

Dissertation

Thermal expansion and stiffness of continuous fiber reinforced Al and Mg Plates

ausgeführt zum Zwecke der Erlangung des akademischen Grades eines
Doktors der technischen Wissenschaften unter der Leitung von

o.Univ.Prof.Dr. H.P. Degischer
Institut für Werkstoffkunde und Materialprüfung

eingereicht an der Technischen Universität Wien,
Fakultät Maschinenbau

von

Dipl.Ing. Mohammed Safwat ALY

Matr.Nr.: 0025958

Wien, im september 2004


.....
Mohammed ALY

Diese Dissertation haben begutachtet:


.....


.....

Acknowledgements

This work was carried out at the Institute of Materials Science and Technology at the Vienna University of Technology. The author is greatly indebted and deeply appreciates his thesis advisor, Prof. H.P. Degischer, for his assistance, numerous stimulating discussions and support in preparing this work. Many thanks are also given to Prof. H.J. Böhm (Institute of Lightweight Design and Structural Biomechanics, Vienna University of Technology) for acting as a reviewer, contributing important suggestions to improve the final manuscript.

The author wishes to acknowledge the financial support by the Egyptian mission department, Ministry of higher education. The author would like also to thank the ARC- Leichtmetallkompetenzzentrum Ranshofen GmbH, and ILK- Institut für Leichtbau und Kunststofftechnik- Technical university- Dresden for providing materials.

Last, but not least, I express my kindest thanks to all my colleagues, who have made working at the Institute of Materials science and testing an interesting experience.

Thermische Ausdehnung und Steifigkeit endlosfaserverstärkter Al- und Mg-Platten

Kurzfassung

Metallmatrix-Verbundwerkstoffe mit Endlosfaserverstärkung (CFRM) zählen zu den Hochleistungsmaterialien, die für den Einsatz in der Raumfahrt und im Kraftfahrzeugrennsport von Interesse sind, wo hohe mechanische Belastbarkeit bei wechselnden Temperaturen von Leichtbaukomponenten zu ertragen sind.

Es werden folgende Materialkombinationen untersucht, die mittels Gasdruckinfiltration als Prüfplatten hergestellt worden sind: Endlosfasern aus hochmoduligen (HM) bzw. hochfesten (HS) PAN-Kohlenstofffasern und Aluminiumoxidfasern (Nextel 610) in Aluminium- oder Magnesiummatrix. Für die Kohlenstofffaserverstärkung werden neben unidirektionaler Faserausrichtung auch Fasergelege und -gewebe untersucht.

Die Eigenschaften und ihre Anisotropie werden in der Plattenebene wie folgt bestimmt:

- Die Steifigkeit bzw. die Elastizitätseigenschaften mittels 4-Punktbiegeversuchen, dynamisch-mechanischer Analyse (DMA), Resonanzmethoden und mit über gepulsten Laser erzeugtem Ultraschall.
- Im 4-Punktbiegeversuch wird die Festigkeit in verschiedenen Richtungen gemessen.
- Die thermische Ausdehnung wird mittels thermisch-mechanischem Analysator (TMA) und dynamischem Dilatometer bei Aufheiz- und Abkühlzyklen zwischen -40°C und 120°C bzw. 200°C (einzelne bis 500°C) bestimmt.

Die thermische Ausdehnung wird mittels physikalischem Temperatúrausdehnungskoeffizienten charakterisiert, der zwischen Aufheiz- und Abkühlfall eine beträchtliche Hysterese aufweist. Es werden elastische, plastische und viskose Verformungsbereiche der Matrix unterschieden, woraus qualitativ auf die Eigenspannungen in den CFRM geschlossen wird. Sich ändernde Eigenspannungen führen zu makroskopischen Längenänderungen. Die größten Spannungsamplituden treten in den Mischkristallen AlMg und MgAl auf, während reine Al-Matrix hauptsächlich plastisch verformt. Aus den anisotropen, thermischen Dehnungen werden die thermischen Volumsänderungen bestimmt, die bei bestimmten CFRM Anomalitäten aufweisen.

Die Anisotropie des thermischen Ausdehnungsverhaltens und der Steifigkeit der CFRM wird mittels Modellen nach Schapery und Berechnungen nach der Laminattheorie nachvollzogen. Es werden die für die Bauteilauslegung wichtigen Kennwerte der CFRM und ihre Veränderlichkeit durch den Eigenspannungszustand dargestellt.

Thermal expansion and stiffness of continuous fiber reinforced Al and Mg plates

Abstract

Metal matrix composites reinforced with continuous fibers (CFRM) are candidate materials for aerospace and automotive racing components, where they can withstand high mechanical loads and temperature cycles at low weight.

Different combinations of continuous fibers and matrices are investigated:

high modulus (HM), as well as high strength (HS) PAN carbon fibers and alumina Nextel 610 fibers with matrices of aluminium and magnesium. C-fiber reinforcements are studied not only in unidirectionally reinforced matrices but as well with stacked preforms or woven fabrics.

Material tests are performed in order to obtain in-plane properties of different CFRM:

- The elastic properties by four point bending test, dynamic mechanical analysis, resonant beam, resonant bar and pulsed laser ultrasonic techniques.
- The strength by four point bending tests.
- The thermal expansion by dilatometry during heating and cooling in temperature cycles between -40 and 120°C and up to 200°C (some heating tests up to 500°C).

An hysteresis in temperature - strain diagrams is observed between heating and cooling, which depends on the constituents of the investigated CFRM and the temperature range. Elastic, plastic and viscous deformation stages are distinguished and the residual stresses are qualitatively deduced. The residual macroscopic strains observed depend on the preceding thermal exposure of the specimen. The highest stress levels are reached by the solid solution matrices of Al-Mg and Mg-Al, whereas pure Al deforms mainly plastically. The thermal changes in volume are calculated from the anisotropic linear expansion, which exhibit anomalies in some cases.

The obtained experimental results are compared with the theoretical estimations using lamination theory for the mechanical properties and Schapery's model for the coefficient of thermal expansion (CTE). The properties relevant for the design of components are presented and their dependence on the residual stress state is described.

Contents

Chapter 1

1. Introduction	1
-----------------	---

Chapter 2

2. State of the art	4
2.1. Metal matrix composites	4
2.1.1. Matrix Material	6
2.1.2. Reinforcement materials	6
2.1.2.1. Carbon fibers	6
2.1.2.2. Alumina fibers	10
2.2. Metal matrix composites processing	10
2.2.1. Infiltration Process	10
2.3. Mechanical properties	14
2.4. Rule of mixture	22
2.5. Elastic properties for unidirectional composites	23
2.5.1. Elastic constants	23
2.5.2. Engineering constants	23
2.6. Thermal expansion	24

Chapter 3

3. Experimental work	31
3.1. Materials	31
3.2. Determination of reinforcement volume fraction	32
3.3. Determination of mechanical properties	33
3.3.1. Four point bending test	34
3.3.2. Dynamic mechanical analysis	35
3.3.3. Resonance bar technique	
3.3.4. Resonant beam technique	37
3.3.5. Laser ultrasonic technique	38

3.4. Thermal expansion measurements	39
3.4.1. Thermomechanical analyzer	39
3.4.2. Dynamic dilatometer	42
3.5. X-ray computer microtomography	43
3.6. Gleeble compression test	44
Chapter 4	
4. Results	46
4.1. Metallography	46
4.2. Four point bending	49
4.2.1. MgAl _{0.6} /C-M40B/65f-UD MMC	49
4.2.2. AlMg _{0.6} /Al ₂ O ₃ -Nextel610/65f	51
4.2.3. Mg/C-Tenax HTA 5331/60f – UD	53
4.2.4. Al/C-M40B/64f, (0, +60°, -60°, -60°, +60°, 0)	54
4.3. Dynamic mechanical analysis	56
4.4. Resonant beam technique	57
4.4.1. MgAl _{0.6} /C-M40B/65f-UD MMC	57
4.4.2. AlMg _{0.6} /Al ₂ O ₃ -Nextel610/65f	57
4.4.3. Al/C-M40B/65f	61
4.5. Resonant bar technique	62
4.5.1. MgAl _{0.6} /C-M40B/65f-UD MMC	62
4.5.2. AlMg ₁ /Al ₂ O ₃ -Nextel610/65f	62
4.6. Pulsed laser ultrasonic technique	63
4.7. Thermal expansion	64
4.7.1. MgAl _{0.6} /C-M40B/65f-UD MMc	64
4.7.2. AlMg _{0.6} /Al ₂ O ₃ -Nextel610/65f	68
4.7.3. Al/C-M40B/65f	72
4.7.4. Mg/C-Tenax HTA 5331/60f-UD	76
4.7.5. Al/C-M40B/64f, (0°, +60°, -60°, -60°, +60°, 0°)	80
4.7.6. Woven MgAl/C-T300J/50f	84

4.8. Damage	90
4.8.1. Damage due to thermal cycling	90
4.8.2. Damage due to production conditions	92
4.8.2.1. Unidirectional MMCs	93
4.8.2.2. Symmetric 6 layer specimens	96
4.9. Matrix yield strength	99
Chapter 5	
5. Discussion of results	102
5.1. Al based UD MMCs	102
5.1.1. Al/C-M40B/65f	102
5.1.2. AlMg1/Al ₂ O ₃ -Nextel610/65f	110
5.2. Mg based UD MMCs	116
5.2.1. MgAl _{0.6} /C-M40B/65f	114
5.2.2. Mg/C-Tenax HTA 5331/55f	121
5.3. 6 Layered UD and woven fiber reinforcement	126
5.4. Volumetric change calculations	129
5.5. Comparison	137
5.6. Anomalous CTE upon cooling	142
Chapter 6	
6. Conclusions	143
Chapter 7	
7. References	145

Introduction

Composites are not really new materials. A composite is a material having two or more distinct constituents or phases and thus we can classify bricks made from mud reinforced with straw, which were used in ancient civilizations, as a composite.

Composite materials are now familiar, specially for engineers, as the composites nowadays utilized in the sporting, aerospace and automotive industries.

While research on metal matrix composites was pioneered in the 1960's, metal matrix composite materials (MMC) have become the object of a significant and sustained research and development effort only since the early 1980's.

The spur to this rapid expansion over the last few decades was the development of boron fibers in the USA in the early 1960's and of carbon fibers in the UK and Japan. These new fibers, which have high elastic constants and strength, gave significant increase in the stiffness-to-weight and strength-to-weight ratios which are the key factors in the selection of materials for designers [1]. The main products are continuous fibers reinforced polymers (CFRP).

When designing a MMC, an objective might be to combine the high ductility and formability of the matrix with the stiffness and load-bearing of the reinforcement, or perhaps to unite the high thermal conductivity with the low thermal expansion of the reinforcement.

The major application of metallic Al-Carbon fiber composite is a high-gain antenna boom (Fig1-1) for the Hubble Space Telescope made with diffusion-bonded sheet of P100 carbon fibers in 6061 Al. This is an actual example of continuous fiber reinforced MMC abbreviated as CFRM (A6061/C-P100/~50f). This boom (3.6 m long) offers the desired stiffness and low CTE to maintain the position of the antenna during space maneuvers. In addition, it provides the wave-guide function, with the MMC's excellent electrical conductivity enabling electrical-signal transmission between the spacecraft and the antenna dish. Also contributing to its success in this function is the MMC's high dimensional stability;

the material maintains dimensional tolerance of ± 0.15 mm along the entire length [2].

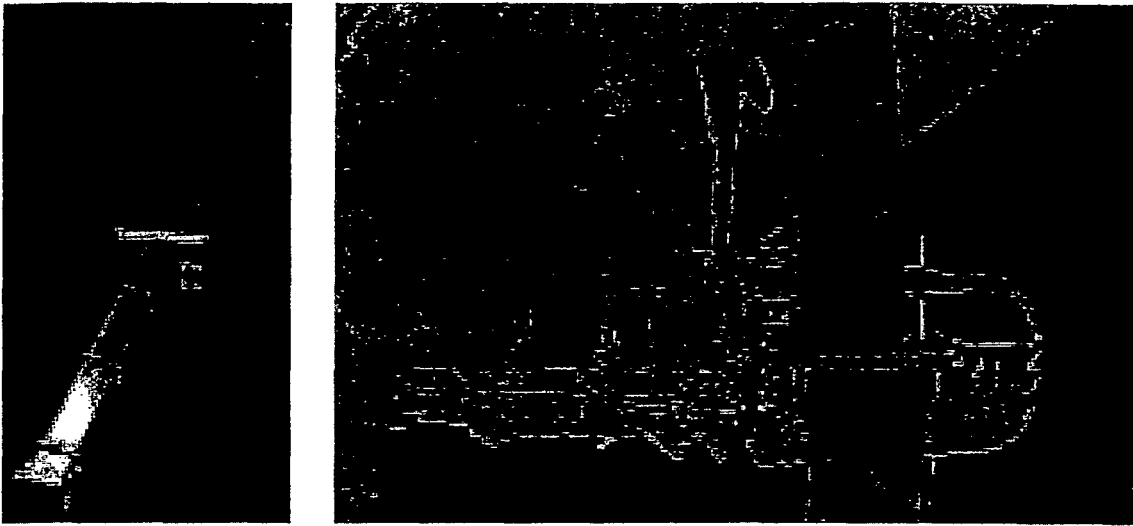


Figure 1-1. The A6061/C-P100 high-gain antenna wave guides/ boom for the Hubble Space Telescope (HST) shown (a-left) before integration in the HST, and (b-right) on the HST as it is deployed in low-earth orbit from the space shuttle orbiter [2].

The prime function of the matrix is to transfer stresses to the fibers because they are stronger and of higher elastic modulus than matrix. The response of a composite to applied stress depends upon the respective properties of the fiber and matrix phase, their relative volume fractions, orientation of fibers relative to the direction of applied stress, and the interface reaction between fibers and matrix.

Although fibers are a striking feature of composites, it is initially helpful to examine the functions of the matrix. Ideally, it should be able to (1) infiltrate fibers and solidify rapidly at a reasonable temperature and pressure, (2) form a coherent bond, usually chemical in nature, at all matrix/fiber interfaces, (3) envelop the fibers, which are usually very notch sensitive, protecting them from mutual damage by abrasion and from the environment (chemical attack, moisture), (4) transfer working stresses to the fibers, (5) separate fibers so that failure of individual fibers remains localized and does not jeopardize the integrity

of the whole component, (6) debond from individual fibers, with absorption of significant amounts of strain energy, whenever a propagating crack in the matrix chances to impinge upon them, and (7) remain physically and chemically stable after manufacture [3].

The behavior of metal matrix composites is often sensitive to changes in temperature. This arises for two reasons; firstly, because the response of a metal to an applied load is itself temperature dependent and secondly, because changes in temperature can cause thermal mismatch to be set up as a result of different thermal contraction between the phases [4].

It is stated that the properties of metal-matrix composites are best modeled by finite element analysis, but it is emphasized that in order to obtain good predictions, the models must be coupled with first-hand characterizations of the constituent phases and their interactions, including the thermal history of the specimens [5].

The general topic of the thesis is the experimental investigation of the thermal expansion behavior of CFRM and related mechanical properties taking into account anisotropy.

2.1. Metal matrix composites

Structural materials can be divided into four basic categories: metals, polymers, ceramics and composites. Composites, which consist of two or more separate materials combined in a macroscopic structural unit, are made from various combinations of the other three materials [6].

The relative importance of the four basic materials in a historical context has been presented schematically in Fig.2-1, in which the steadily increasing importance of polymers, composites, and ceramics and the decreasing role of metals is shown clearly. Composites are generally used because they have desirable properties which could not be achieved by either of the constituent materials acting alone [6].

Metal matrix composites have a series of advantages that are very important in the utilization of structural materials. These advantages relate to the same metallic properties that have led to the general primacy of metal alloys for use in dynamic engineering structures. They include the combination of the following properties: (i) high strength; (ii) high modulus; (iii) high toughness and impact properties; (iv) low sensitivity to changes in temperature or thermal shock; (v) high surface durability and low sensitivity to surface flaws; (vi) high electrical and thermal conductivity; and (vii) excellent reproducibility of properties [7].

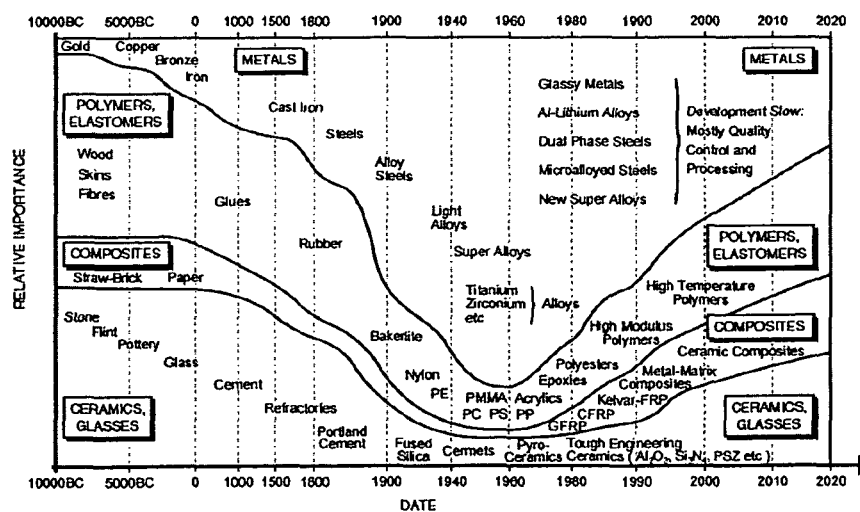


Fig.2-1, Schematic diagram showing the relative importance of the four classes of materials as a function of time [3].

On the Eshelby chart of Fig. 2-2, guide lines are plotted for material selection for the three service situations, and hence performance indicators. Consider the guide line drawn for $E^{1/3}/\rho$; this corresponds to a specific set of service conditions for panels supported at both ends and subject to a central force. Any material alternatives, for instance light metals and MMC, just move the line up or down the chart whilst maintaining the same slope. All materials which lie on the line will perform equally well under the specified conditions for that line. The performance of materials above the line is better. Comparison between the composites and alloys indicate that most composites outperform alloys under conditions corresponding to the $E^{1/2}/\rho$ and $E^{1/3}/\rho$ guide lines but only some composites are better than alloys for E/ρ service limited situations [8].

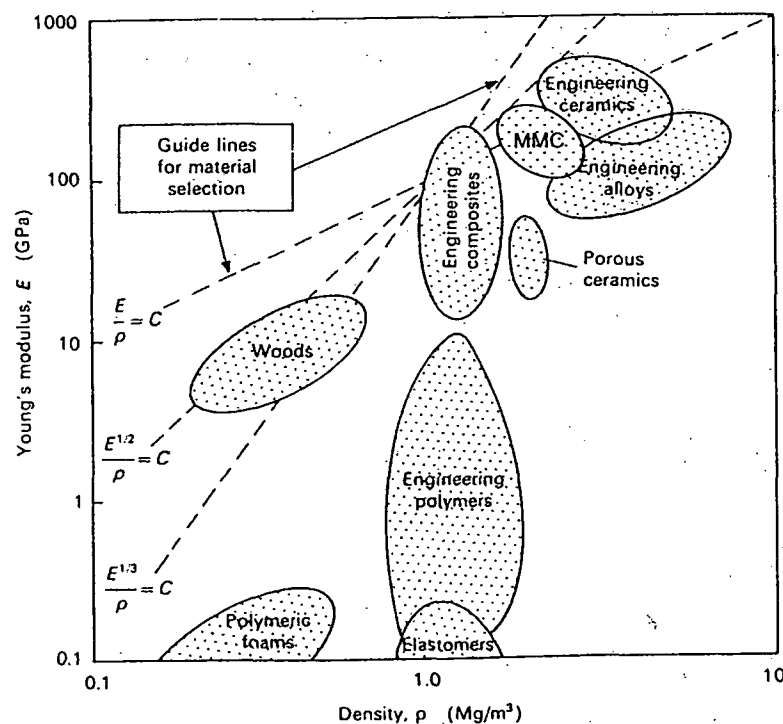


Fig.2-2, Material property chart; Young's modulus versus density, with the performance indicators E/ρ , $E^{1/2}/\rho$ and $E^{1/3}/\rho$ including the range of MMC [8].

2.1.1. Matrix Materials

Polymers, metals, and ceramics are all used as matrix materials in composites, depending on the particular requirements. The purpose of the matrix is to hold the fibers together in a structural unit and to protect them from external damage, transfer and distribute the applied loads to the fibers, and in many cases contribute to properties such as ductility and toughness. Because the reinforcements are typically stronger and stiffer, the matrix is often the weak link in the composite, from a structural perspective. As a continuous phase, the matrix therefore controls the transverse properties, interlaminar strength, and elevated temperature strength of the composite. The matrix holds reinforcing fibers in the proper orientation and position so that they can carry the intended loads and distributes the loads more or less evenly among the reinforcements. By using light weight metals such as aluminium, titanium and magnesium and their alloys operating temperature can be extended in the case of titanium to about 1250°C [4,9].

2.1.2. Reinforcement materials

Metal matrix composites can be reinforced by strong second phase of three dimensional shapes (particulate), two dimensional shapes (laminar), or one dimensional shapes (fibrous). This study considers only continuous fibers, so attention to the fibrous reinforcements will be given.

2.1.2.1. Carbon fibers

Unfortunately, the names “carbon” and “graphite” are often used interchangeably to describe fibers based on the element carbon. These fibers are usually produced by subjecting organic precursor fibers such as polyacrylonitrile (PAN) or rayon to a sequence of heat treatments, so that the precursor is converted to carbon by pyrolysis. The major difference is that the graphite fibers are subjected to higher temperature pyrolysis than carbon fibers. The result is that carbon

fibers typically are less than 95% carbon, whereas graphite fibers are at least 99% carbon [6, 9,10]. Although carbon fibers were once prohibitively expensive, the cost has dropped significantly as production capacity and demand increased (Fig.2-3).

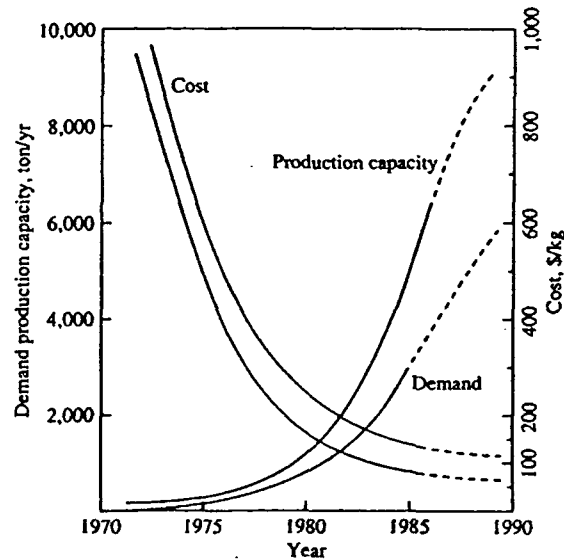


Fig.2-3, Production capacity and cost of PAN-base carbon fibers as a function of time [6].

The graphitic structure consists of hexagonal layers, in which the bonding is covalent and strong (525 kJ/mol); these layers, which are called the basal planes, are stacked in an ABAB sequence with inter-layer bonds being weak (<10 kJ/mol) van der Waals bonds. It should be no surprise that the consequence of the marked difference in the intra-layer and inter-layer bonding is that the properties of graphite are very anisotropic. The theoretical elastic modulus of graphite is approximately 1000GPa in the basal plane and only 35GPa in the c-direction perpendicular to this plane. Alignment of the basal plane parallel to the fiber axis gives stiff fibers which, because of the relatively low density of around 2Mg/m³, have extremely high values for specific stiffness.

Graphite sublimates at 3700°C but starts to oxidize at around 500°C; carbon fibers can, however, be used at temperatures exceeding 2500°C if protected from oxygen. Carbon fibers are produced from a variety of precursors. The

mechanical properties vary greatly with the precursor used and the processing conditions employed as these determine the perfection and alignment of the crystals. There are three main precursors [6,11]:

- 1- Controlled heating of cellulose or rayon fiber converts the fiber to graphite. Loss of weight and shrinkage takes place during pyrolysis at 200 to 400°C as the organic precursor decomposes to carbon with a yield of 15-30%. This is followed by carbonization and finally graphitization at higher temperatures; at this stage the fibers have low strength and stiffness. However hot stretching by up to 50% at temperature in the range 2700 to 3000°C increases the modulus and strength by developing a preferred orientation in the fibers and reducing porosity.
- 2- Fibers produced from polyacrylonitrile, PAN, have a high degree of orientation in filament form. The PAN precursor gives a yield of up to 50% on conversion to carbon. The production is divided into three stages [12]; the first stage involves stretching and oxidation. The fibers are initially stretched 500-1300% to improve molecular alignment and then heated in air, while still under tension, to 200-280°C, this is followed by oxidation. Heating in nitrogen or argon at 900-1200°C produces low modulus, high strength carbon fibers, which have fine well-oriented crystals parallel to the fiber axis. However they have a fair degree of porosity and the density is only 1.74 Mg/m³. Heating in argon up to 2800°C causes graphitization and produces high modulus fibers of increased density up to 2 Mg/m³. The value of modulus increases with increasing temperature of graphitization. PAN carbon fibers can be supplied in three basic forms, high modulus (HM), intermediate modulus (IM), and high strength (HS). Basal planes are somewhat curled but parallel to fiber axis. A three dimensional representation of the basal planes in PAN carbon fibers is given in Fig.2-4.

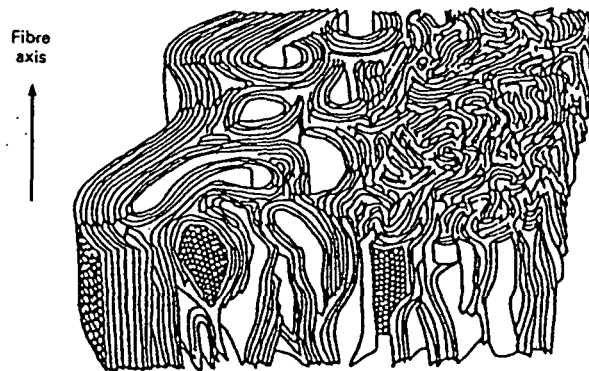


Fig.2-4, Schematic representation of the three dimensional structure of the orientation of the basal plane of the graphite in PAN carbon fibers [8].

- 3- Fibers produced from petroleum and coal-tar pitches which contain a complex mixture of high molecular weight aliphatic and aromatic hydrocarbons. The pitch is heated to above 350°C to polymerize to molecular weight of about 1000. The polymer is melt spun and after oxidation to induce cross-linking, and hence prevent the fibers remelting and sticking together, the fibers are carbonized at temperature up to 2000°C giving low modulus carbon fibers with a yield of about 80%. The degree of graphitization is controlled by heat treatment at temperature up to 2900°C. Basal planes are oriented predominantly radially, therefore, transverse properties are somewhat higher than those of PAN.

An unusual characteristic of carbon fibers is their very low, or even slightly negative, coefficient of longitudinal thermal expansion. As for other properties, the coefficient of thermal expansion depends on the fabrication route and hence degree of graphitization and crystal orientation. Ultra high modulus carbon fibers have negative coefficients of expansion of approximately -1.4 ppm/K [8].

2.1.2.2. Alumina fibers

Alumina (Al_2O_3) can adopt several crystal structures, some of which are metastable; the different alumina phases are designated alpha- (α), delta- (δ), gamma- (γ) and eta- (η) alumina. The familiar bulk alumina ceramic, used for example in spark plugs, is α -alumina which has a hexagonal close packed crystal structure. α -alumina is the predominant phase in some fibers, but the other forms, particularly δ -alumina, are also found as the major phase in certain fibers. Alumina fibers are isotropic and polycrystalline contain nearly 100% Al_2O_3 but also other oxides. The most common oxide addition is SiO_2 .

Alumina has a high melting point in excess of 2000°C and a relatively low viscosity when molten and is therefore not amenable to fiber production by melt spinning techniques. The production methods employed can be classified as slurry forming plus firing, and solution or sol-gel processing plus heat treatment [13].

2.2. Metal matrix composites processing

A wide variety of fabrication methods have been employed for MMCs but most of these can be conveniently classified into one of these following categories [4]:

- | | |
|----------------|-----------------|
| a) solid state | b) liquid state |
| c) deposition | d) in situ |

From the liquid state method of fabrication, the infiltration process which has grown to become one of the most significant methods of production of composite materials [14].

2.2.1. Infiltration Process

With metal matrix composites, infiltration processes are separable into two main classes, according to whether or not the matrix wets the reinforcement and can

infiltrate spontaneously the preform. Although spontaneous infiltration is in some cases feasible, molten metals generally do not wet typical metal matrix composites' reinforcement phases, such as carbon, oxides and carbides. Then, to produce the composite by infiltration, force must be provided by external means to drive the molten metal matrix into the porous reinforcement preform. This is generally obtained by pressurization of the melt to pressures in the order 1 to 100 MPa.

In the gas pressure infiltration process, gas is used to drive the molten metal into the preform under pressure of 1-20 MPa. Fig. 2-5, is a schematic diagram showing the steps of gas pressure infiltration, in the first step the chamber which contains the liquid metal is evacuated and then the second step in which a gas is forced into the chamber under pressure which in turn causes the molten metal to infiltrate the preform, the pressure is maintained for the short period of time required for solidification.

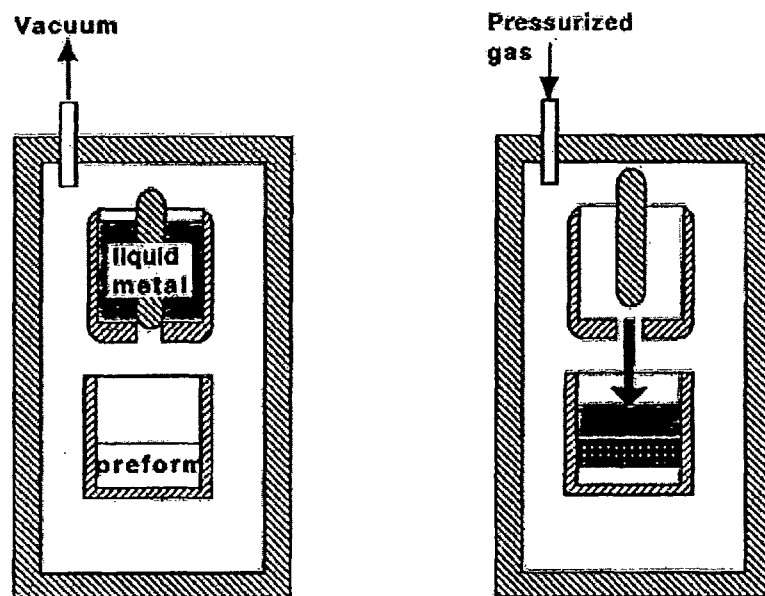


Fig.2-5, Schematic description of gas pressure infiltration process used for metal matrix composites production [14].

Governing process parameter:

Four parameters are governing the infiltration process [14],

- (i) Viscosity, the fluid viscosity governs strongly the infiltration kinetics, fortunately, molten metal have a viscosity of water as shown in Fig. 2-6.
- (ii) Capillary phenomena, wetting of matrix to the fibers is governed by Young's equation $\gamma_{fm} = \gamma_{fa} + \gamma_{ma} \cos\theta$ where γ_{fm} , γ_{fa} , and γ_{ma} are the surface energies of fiber-matrix, fiber-atmosphere, and matrix-atmosphere interfaces respectively, and θ the wetting angle: the lower θ , the better wetting is.
- (iii) Permeability, is a function of the preform volume fraction, fiber arrangement and stress state, as well as of the degree of fluid saturation in the preform.
- (iv) Stress-strain behavior of the fiber preform, the compliance of fibrous preform is generally measured using a compression test on the un-filtered preform.

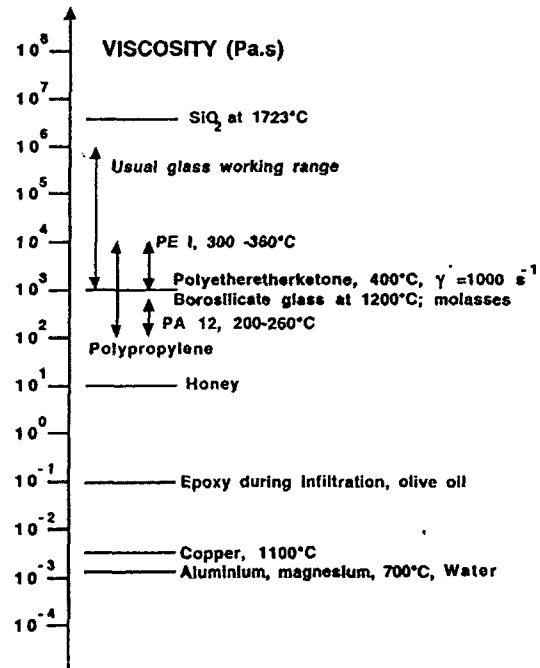


Fig. 2-6, Range of viscosities of matrices and various other fluids [14].

Studies on the reaction products at the interface for different carbon reinforced aluminium metal matrix composites revealed that, the formation of aluminium carbide Al_4C_3 as a product from the reaction $4Al + 3C \rightarrow Al_4C_3$ is always the reason for poor mechanical properties and high tendency of corrosion in aqueous media, especially in case of PAN carbon fibers. The reason is that, in Pan carbon fibers many basal graphite planes are exposed at the surface to provide high energy sites for carbide nucleation [15].

In case of Pitch carbon fibers reinforced aluminium wires, aluminium carbides were observed by TEM as shown in Fig. 2-7. The tensile strength is decreasing with increasing time of infiltration due to increasing in the carbide content (Fig. 2-8) in interfacial region between fibers and matrix [16].

Conversely, although magnesium is a reactive metal with a high affinity for oxygen, it does not form stable carbides. Therefore, it is generally known that no reaction takes place between the fibers and the surrounding matrix in carbon reinforced magnesium composites, when the matrix is un-alloyed [17].

It has been shown [18] that $Mg_{17}Al_{12}$ precipitates form discontinuously at the fiber/matrix interface, even if only a small amount of Al is present in the matrix.

Unlike the previous type of reactions which lead to second phase formation, there are many examples where diffusion of one or both components at the fiber matrix interface may occur but the scale of the reaction is such that no second phases are produced, as in alumina reinforced aluminium matrix composites in which the interface reaction causes a strong bond between fiber and matrix [15].

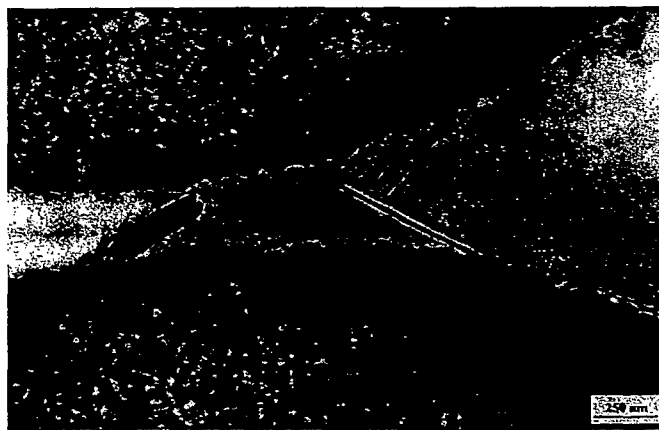


Fig.2-7, Carbide formation after 1.3 sec. of infiltration time [16].

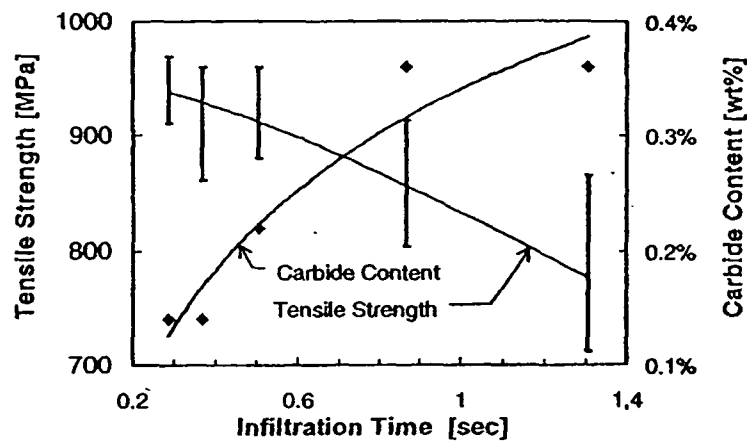


Fig.2-8, Tensile strength and carbide content in relation to the infiltration time of the 55% carbon P25 pitch fibers reinforced high purity aluminium matrix composite [16].

2.3. Mechanical properties

The ideal stress strain curve for unidirectional metal matrix composites in the longitudinal direction is presented in Fig. 2-9. Generally this curve consists of two stages. During the stage I, both fiber and matrix remain elastic, during stage II the matrix deforms plastically and fibers remain elastic. Possibly, there is a stage III where both matrix and fibers deform plastically, but generally the fibers break being unable to deform plastically [20].

The improvement in the mechanical properties is particularly significant specially for such aluminium and magnesium metals that have relatively low stiffness and strength values. For instance, the value of stiffness in fiber direction can be doubled for aluminium composite compared to pure aluminium as illustrated in Fig 2-10.

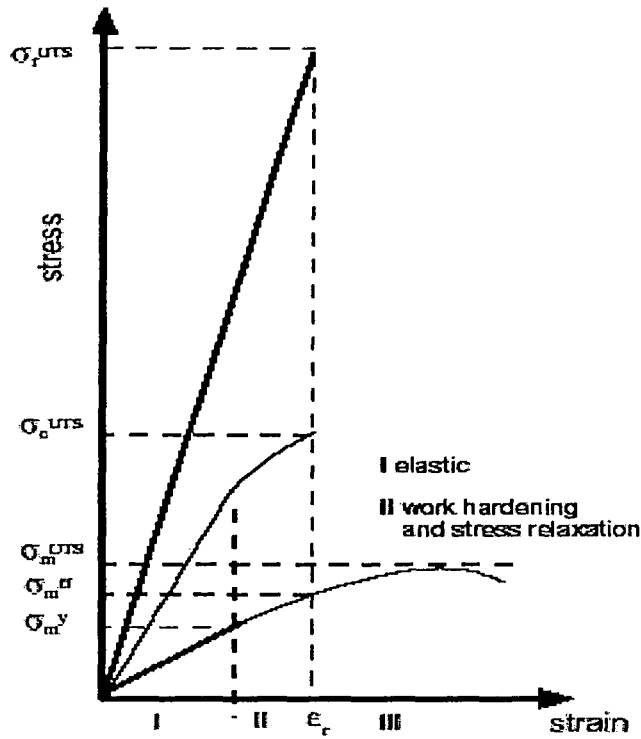


Fig.2-9, Ideal stress-strain curve for metal matrix composites [20].

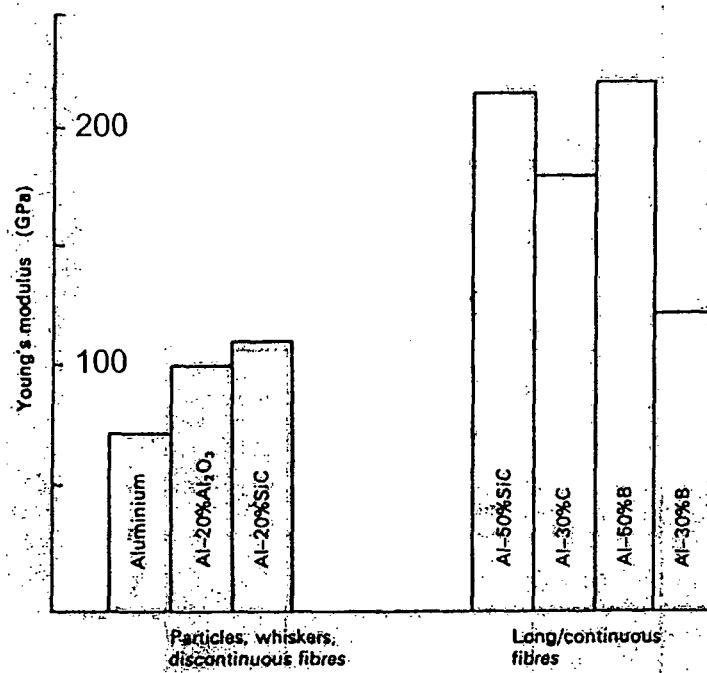


Fig.2-10, Effect of reinforcement on the Young's modulus of aluminium (Scale extrapolated with respect to Al) [8].

Stiffness and strength are generally higher with increased volume fraction of the reinforcement, however, because of processing difficulties, the strength is sometimes found to decrease at high levels of reinforcement as illustrated by the curve of Al/B in Fig. 2-11. It can be seen from the curves that, the longitudinal strength of the continuous fibers composite is better than that obtained with particulate matrix composites for a given volume fraction of reinforcement [8].

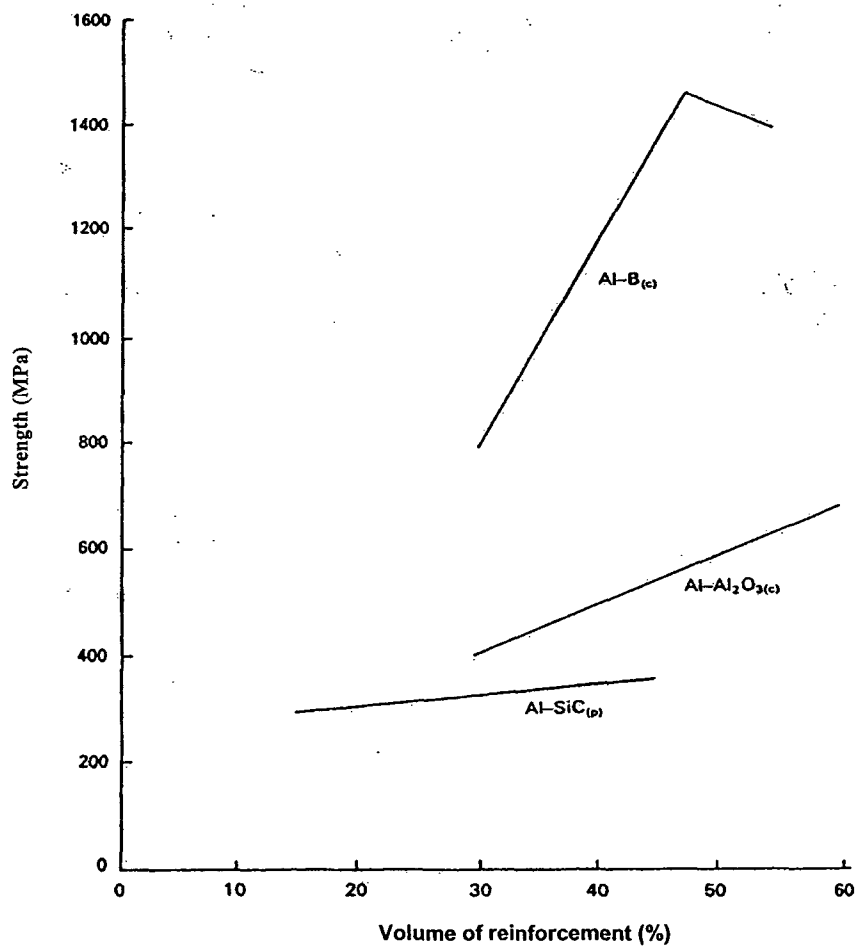


Fig.2-11, Effect of volume reinforcement on the tensile strength of aluminium alloy matrix composites, p and c refer to particulate and continuous fiber respectively, Values for c composites are longitudinal strengths [8].

When unidirectional continuous fiber composites are tested at an angle to the fiber axis, lower values than the longitudinal values for strength and stiffness would be observed as illustrated in Fig.2-12. The lowest value is obtained in the transverse direction in which the properties are largely dependent on the properties of the matrix and fiber matrix bonding rather than the properties of reinforcement.

Mechanical properties in terms of the specific strength and stiffness are illustrated in Fig. 2-13, for aluminium and its composites, benefits can be seen of continuous fiber reinforcement provided that the service stress is parallel to the fiber axis.

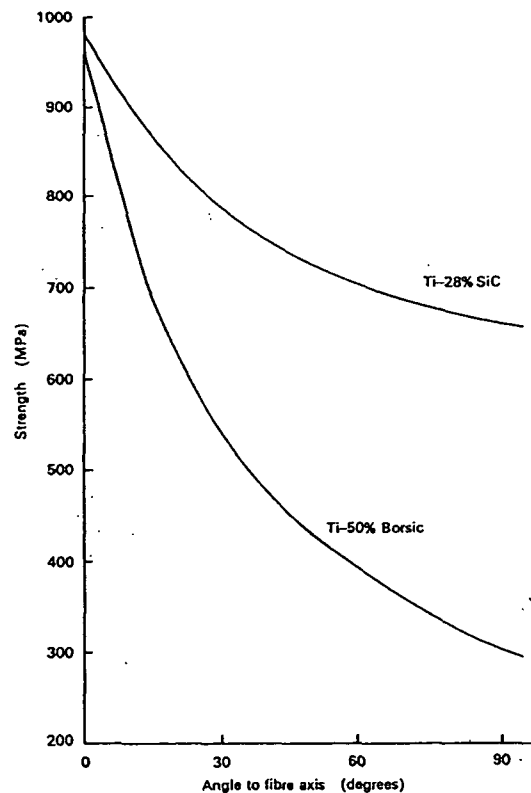


Fig.2-12, Graph showing the marked effect of angle between the tensile axis and the fiber axis on the strength of monofilament fiber reinforced titanium alloy (Ti-6Al-4V) [8].

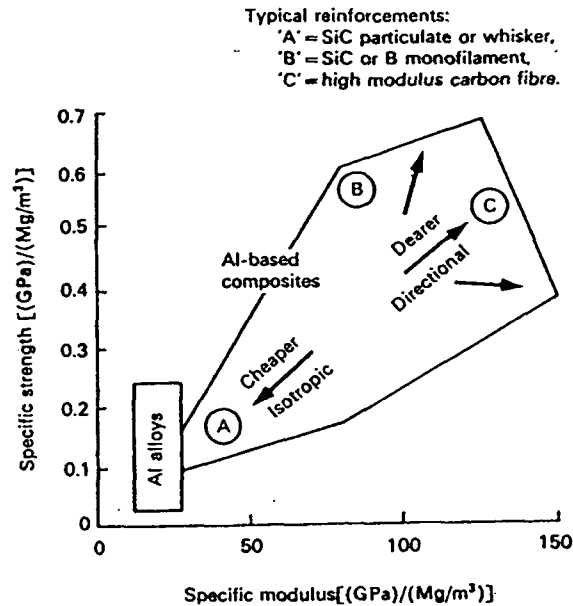


Fig.2-13, Range of specific strength and specific modulus values for aluminium alloy matrix composites compared with that for aluminium alloys [8].

A.Vassel [21] compared between mechanical properties of continuous fiber reinforced aluminium and titanium matrix composites, he stated that both systems have outstanding mechanical properties (modulus and strength) in the longitudinal direction. The longitudinal Young's modulus at room temperature for both systems is compared in fig. 2-14, it can be noted that the stiffness value for Ti/SiC MMC (220 GPa at v_f of 0.35) is two times that of Ti alloy, and Al/Nextel610 (240 GPa at v_f of 0.60) is three times that of Al alloy. Specific longitudinal strength of Al-MMCs are higher than those of Ti-MMCs below 300°C and carbon fiber reinforced Al-MMCs exhibit the best tensile properties in the temperature range 20-300°C, as illustrated in Fig. 2-15. He also analyzed the transverse properties, and he found that the anisotropy of Al MMCs is more pronounced than in Ti MMCs and the solution of this problem is to use cross ply laminates.

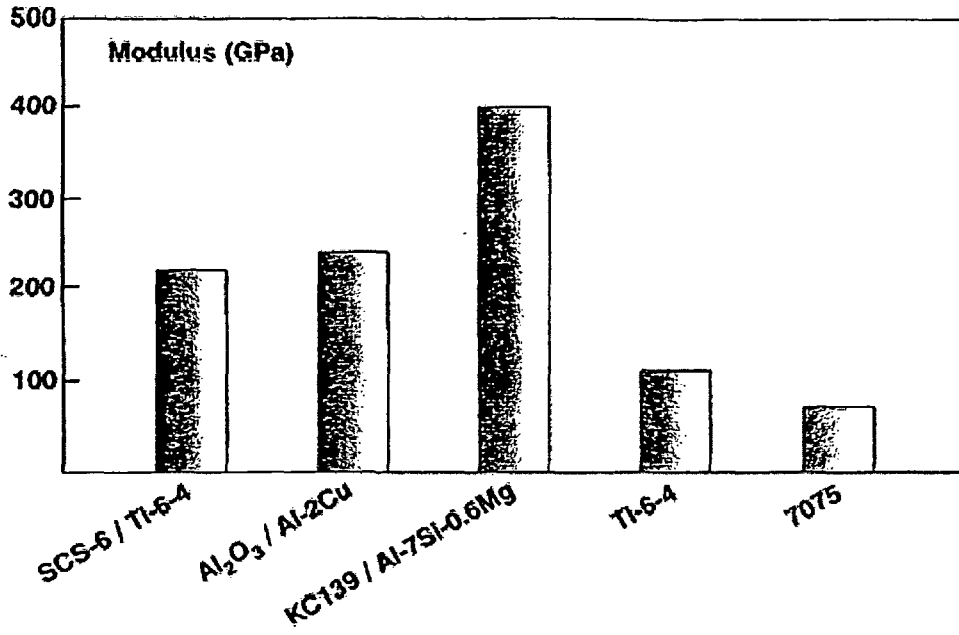


Fig.2-14, Longitudinal Young's modulus: materials comparison at room temperature [21].

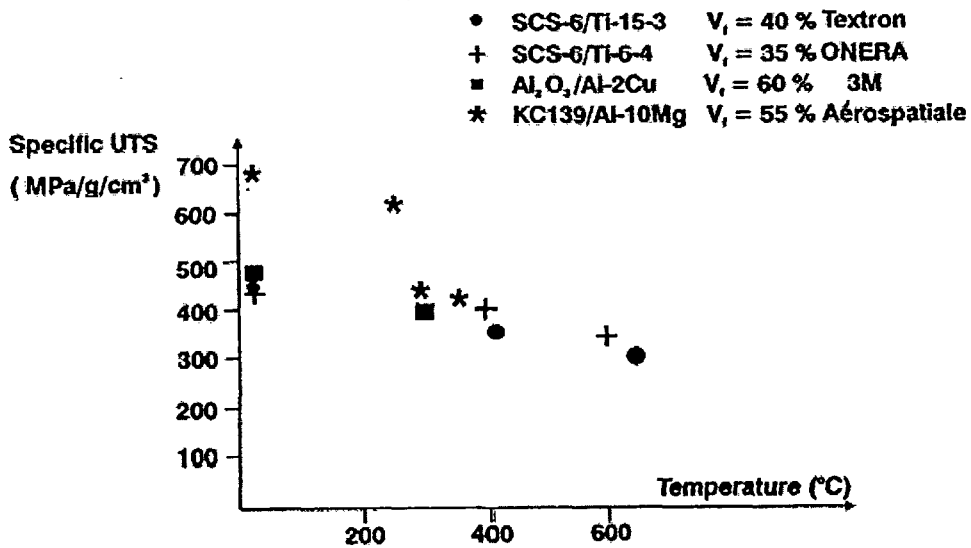


Fig. 2-15, Specific tensile strength of Ti and Al MMCs as a function of temperature [21].

The distribution of the reinforcements, orientation and homogeneity, plays an important role in the values of strength and Young's modulus of the unidirectional matrix composites. Studies on alumina Nextel 610 fiber reinforced Al MMCs have been done by D.Ducret et al [22]. Material elastic constants have been

determined by means of two different methods; ultrasonic bulk waves and tensile test. Materials are produced by medium pressure infiltration with a volume fraction of the fibers is 0.5. The results for this study are listed in table 2-1.

Table 2-1, Engineering constants for Al/ alumina/ 50f CFRM [22].

Property	Symbol	Bulk waves	Mechanical test
		GPa	GPa
Longitudinal modulus	E_1	233.3±2.3	223±10
Transverse modulus	$E_2=E_3$	141.9±1.5	138±5
Shear modulus	G_{23}	51.8±1.7	
	$G_{13}=G_{12}$	54.6±0.7	52±3
Poisson's ratio	$\nu_{21}=\nu_{31}$	0.177±0.001	0.19±0.01
	$\nu_{12}=\nu_{13}$	0.291±0.003	0.31±0.01
	$\nu_{23}=\nu_{32}$	0.368±0.003	

Considering anisotropy measurements a tensile test on woven T300 carbon fiber reinforced magnesium has been investigated by K.Schreiber et al [23]. The results for Young's, shear moduli, and Poisson's ratio for different fiber directions are illustrated in a polar diagram as shown in fig.2-16.

For different continuous fiber reinforced aluminium MMCs produced by gas pressure infiltration process, a three point bending test has been done to determine the strength and stiffness in fiber direction by H.P.Degischer et al [24]. The results are listed in table 2-2.

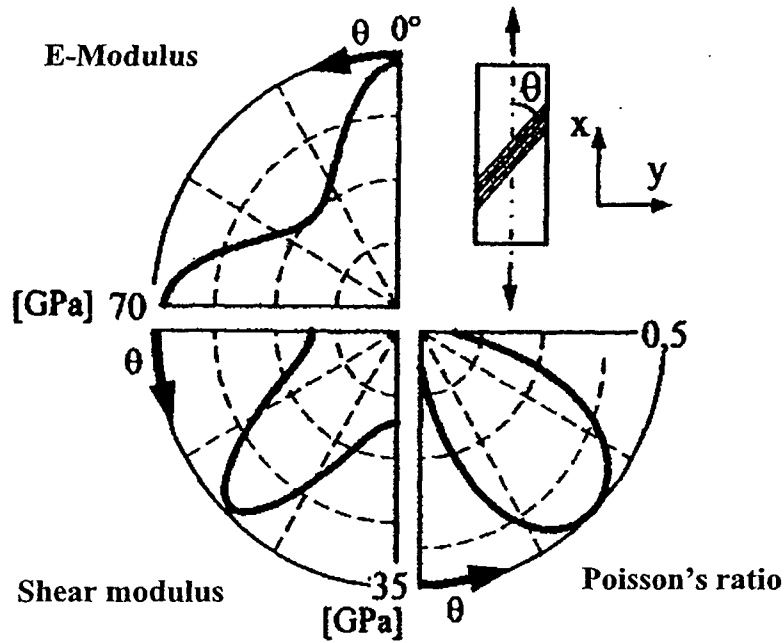


Fig. 2-16, Polar digram showing directional dependence of different properties in carbon fibers T300 woven 0/90 reinforced magnesium [23].

Table 2-2, Strength and stiffness values as a result from three point bending test for different fiber reinforced Al MMCs [24].

Fiber	Strength MPa	Stiffness GPa
C: EXAS 6K 2N	480	150
C: T300B 6K 50E	520	150
C: RK30 12K	1070	170
C: EIMS 12K 1.0N	920	170
C: EHMS 10K 0.7E	1380	200
C: M40B 6K 50B	1550	220
C: TONEN FT700 3K	800	370
SiC: NL-207	1130	120
Al ₂ O ₃ : Altex SN-11-1K	1190	120
Al ₂ O ₃ : Almax Al-1001-50M	900	190

2.4. Rule of mixture

The longitudinal modulus of elasticity and strength of unidirectional fiber composites can be calculated, with a good approximation, using the linear “rule of mixture”. Assuming an isostrain condition and a simple parallel arrangement for fibers and matrix as illustrated in Fig. 2-17a, a constant strain is imposed on the model in the fiber direction (Voigt model), and the total force and the average stress are computed, resulting the ROM expression in the direction of fibers as follows,

$$E_l = v_f E_f + v_m E_m$$

Where, E and v stand for young's modulus and volume fraction respectively, subscripts l,f and m for longitudinal, fibers and matrix, respectively.

A similar expression can be obtained for the composite longitudinal strength, as long as the fibers do not fail premature due to localization of internal stresses, using for the matrix the strength at rupture of fibers,

$$\sigma_l = v_f \sigma_f + v_m \sigma_m$$

Where, σ is the strength

On the other hand, for the transverse direction, assuming isostress or series arrangement of fibers and matrix (Reuss model) as illustrated in Fig.2-16b gives,

$$1/E_t = v_f/E_f + v_m/E_m$$

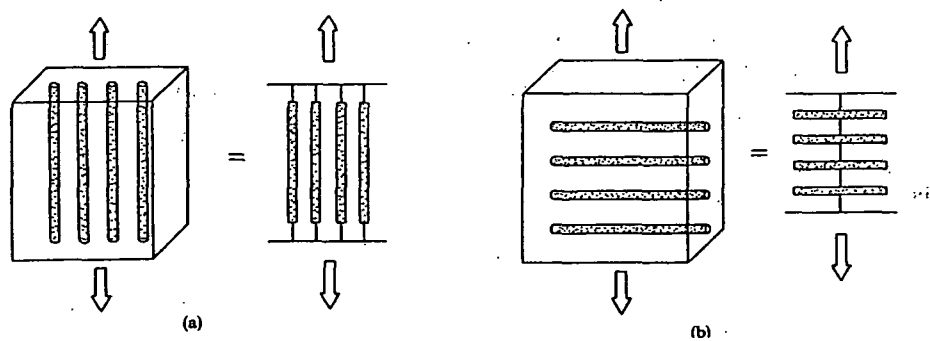


Fig.2-17, Unidirectional composite: (a) isostrain or action in parallel, (b) isostress or action in series [19].

The in plane shear modulus can be estimated from a formula similar to Reuss model, while density, Poisson's ratio, and conductivities can be estimated similar to Voigt model.

2.5. Elastic properties for unidirectional composites

2.5.1. Elastic constants

The elastic properties of an anisotropic material can be described by the three dimensional generalized Hooke's law:

$$\sigma_{ij} = C_{ijkl} \epsilon_{kl} \quad \text{or} \quad \epsilon_{ij} = S_{ijkl} \sigma_{kl}$$

where σ_{ij} and ϵ_{kl} are the mean stresses and strains at the macroscopic scale.

The effective elastic constant C_{ijkl} and S_{ijkl} are the fourth rank effective stiffness and compliance tensors that have 81 (9x9) components. Due to stress and strain symmetry, ($\sigma_{ij} = \sigma_{ji}$ and $\epsilon_{ij} = \epsilon_{ji}$), it is convenient to use the 6x6 matrix components provided from contracted notation. Orthotropic symmetry which is sufficiently general to describe most of fibrous composites, have only 9 independent elastic constants. Then, the stiffness matrix in the principal direction becomes,

$$[C_{ij}] = \begin{bmatrix} C_{11} & C_{12} & C_{13} & 0 & 0 & 0 \\ & C_{22} & C_{23} & 0 & 0 & 0 \\ & & C_{33} & 0 & 0 & 0 \\ & \text{Sym.} & & C_{44} & 0 & 0 \\ & & & & C_{55} & 0 \\ & & & & & C_{66} \end{bmatrix} \quad (2.5.1)$$

Indices 1,2 and 3 of C_{11} , C_{22} , and C_{33} refer to normal stress and extensional strain along directions 1, 2, and 3 respectively. Indices 4,5, and 6 of C_{44} , C_{55} , and C_{66} refer to the shear in 23, 13, and 12 planes, respectively. C_{12} , C_{13} , and C_{23} are coupling elastic constants. In case of axial symmetry around axis 1, then plane 23 is an isotropic plane and we have only 5 independent elastic constants that characterize the elastic behavior: C_{11} , $C_{22} = C_{33}$, $C_{13} = C_{12}$, C_{23} , C_{44} , $C_{55} = C_{66}$, with the transverse isotropic relation: $C_{44} = (C_{22} - C_{23})/2$ [25-27].

2.5.2. Engineering constants

The results of mechanical experiments are generally not expressed as elastic constants C_{ij} but as engineering constants. These are Young's moduli E_i , shear

moduli G_{ij} and Poisson's ratios ν_{ij} . The compliance terms of the compliance matrix S_{ij} can be expressed as functions of these engineering constants. Let us consider a material with orthotropic symmetry. Hence, the compliance terms along the diagonal of the compliance matrix are the inverse of the three Young's moduli and three shear moduli. If the symmetry axis is axis 1, we have five independent engineering elastic constants that characterize the elastic behavior:

$$E_1, E_2 = E_3, G_{23}, G_{13} = G_{12}, \nu_{12} = \nu_{13}, \nu_{23}$$

with
$$G_{23} = E_2/2(1 - 2\nu_{23}) \quad (2.5.2)$$

which is the transverse isotropic relation [28].

2.6. Thermal expansion

Thermal expansion characteristics are extremely important in applications where the component is exposed to changing thermal environments. The geometric changes with temperature must be understood in order to select the appropriate material for specific end uses.

The influence of thermal stresses in metal matrix composites compared to polymer matrix composites is much larger because of the high temperature of production and use of metal matrix composites, and the relaxation of deviatoric thermal stresses by plastic yielding is more difficult because of the much higher yield strength of the metallic matrices. These lead to nonreversible phenomena upon thermal cycling causing degradation of composite properties as a result of damage accumulation.

For prediction of longitudinal and transverse coefficients of thermal expansion (CTE), the model derived by Schapery based on energy consideration is frequently used [29-31].

Schapery [32] derived bounds for the three principal linear expansion coefficients α_i of anisotropic composites. The upper and lower bounds on α_i correspond to, the lower and upper bounds on the composite bulk modulus K_c and Young's moduli E_i .

Schapery showed that, if the Poissons ratio ν_f and ν_m of the fiber and matrix are equal, the longitudinal thermal expansion coefficient α_l with unidirectional continuous fibers can be expressed as

$$\alpha_l = \frac{\alpha_m \nu_m E_m + \alpha_f \nu_f E_f}{\nu_m E_m + \nu_f E_f} \quad (2.5.3)$$

Schapery also proposed an approximate expression for the transverse CTE α_t of the composite with unidirectional continuous fibers as

$$\alpha_t = \nu_m(1+\nu_m)\alpha_m + \nu_f(1+\nu_f)\alpha_f - \nu_E \alpha_l \quad (2.5.4)$$

and

$$\nu_E = \nu_f \nu_f + \nu_m \nu_m$$

Where α , ν , ν , and E stand for coefficient of thermal expansion, volume fraction, Poissons ratio, and Young's modulus, fiber data are marked by a subscript f and matrix data by subscript m . Subscripts l and t stand for longitudinal and transverse properties, ν_E is the effective longitudinal Poissons ratio calculated from the rule of mixtures.

Prediction of CTE by Schapery is in some cases in accordance with the experimental data, and in other cases is little higher than predictions [33].

A modification on Schapery has been done by Boehm [34], he suggests that after a critical temperature, the matrix is fully yielded, and the equation of schapery can be modified by replacing the Young's modulus of the matrix by the hardening modulus $E_m^{(h)}$, and by treating the matrix as incompressible, i.e. $\nu_m=0.5$, the longitudinal and transverse CTE become,

$$\alpha_l^p = \frac{\alpha_m \nu_m E_m^h + \alpha_f \nu_f E_f}{\nu_m E_m^h + \nu_f E_f} \quad (2.5.5)$$

$$\alpha_t^p = \frac{3}{2} \nu_m \alpha_m + \nu_f(1+\nu_f)\alpha_f - \alpha_l^p \left(\frac{1}{2} \nu_m + \nu_f \nu_f \right) \quad (2.5.6)$$

In addition to Schapery's model other models have also been proposed [30]. Chaims has given an expression for the CTE in the longitudinal direction identical to that of Schapery. The coefficient of thermal expansion in the transverse direction due to Chaims is

$$\alpha_t = \alpha_f v_f^{0.5} + [1 - v_f^{0.5}] [1 + v_f v_m E_f / E_c] \alpha_m \quad (2.5.7)$$

where E_c is the Young's modulus of the composite calculated by the rule of mixture.

Rosen and Hashin derived expressions for the CTE of unidirectional fiber reinforced composites in the longitudinal and for the transverse directions where the bulk modulus would be required [23].

The coefficient of thermal expansion for different metal matrix composites systems has been measured. For unidirectional MMCs, numerous studies on determination of CTE especially in the fiber direction for light metals as matrices reinforced with carbon, silicon carbide or alumina have been executed.

S.Rawal [35] produced an overview about the space application of MMCs. He compared different longitudinal CTE values for Al6061/P100, AZ91/P100, and Al/B UD MMCs in the range of -100 to 100°C, the values were -0.49, 0.54, and 5.8 ppm/K respectively.

R.U.Vaidya et al [30] determined the CTE for fibers and particulate reinforced MMCs in the range of 20-500°C. The materials were SiC fibers reinforced Al6061 matrix produced by diffusion bonding and alumina fibers reinforced Al-Li 8090 and MgZE41A matrix produced by conventional casting with 0.35-0.48 fiber volume fraction. He found that the values of CTE in ppm/K for SiC/Al 6061 is 5.6 in longitudinal and 14.5 in transverse directions, for Al₂O₃/Al-Li 8090, the CTE is 9.5 in longitudinal and 16.3 in transverse, and for Al₂O₃/MgZE 41A 9.5 in longitudinal and 19.8 in transverse directions respectively. He also observed a hysteresis loop in length change during heating and cooling between 20°C and 500°C for all systems.

W.Lacom et al [31] found a wide scatter in the CTE measurements in carbon fibers reinforced aluminium in both high modulus (HM) and high strength (HS) UD fibers. In the range of 100 to 500°C, the CTE decreased with increasing temperature beginning from a value of 2-5 and 0-1.8 ppm/K for HS and HM carbon fiber reinforced aluminium, respectively.

The cycling conditions are among the most severe environmental conditions for composites. The difference between the coefficient of thermal expansion of the constituents causes large thermal mismatch to be induced in the composite during cycling, often resulting in dimensional changes and pronounced strain hysteresis during cycling [36-40]. Thermal cycling induced damage in MMCs can take the form of plastic deformation of the matrix, damage at fiber matrix interface, such as microvoid formation or debonding at the interface, interfacial sliding or in some cases even fiber fracture.

Damage has been evaluated by Chawla et al [41] by measuring Young's modulus and density after thermal cycling. He expressed the damage in the elastic modulus as

$$D_E = 1 - (E_n/E_0) \quad (2.5.8)$$

where E_n is the elastic modulus after n cycles and E_0 is the elastic modulus before cycling. In the same manner he expressed damage in terms of density as $D_\rho = 1 - \rho_n/\rho_0$ where ρ_n is the density after n cycles and ρ_0 is the initial density before cycling.

Fig.2-18 a,b, shows the residual stresses of the composite as a function of the radial distance arising from cooling from 288°C to room temperature of SiC fibers reinforced Al matrix composites with considering matrix fully elastic (Fig.2-18a) and matrix fully plastic (Fig.2-18b), as computed by Chun et al [42] based on coaxial cylinder model. Analyzing these two figures reveals that, all components of residual stresses in the fiber are compressive and constant. The radial and hoop stresses in the fibers are equal. The matrix is fully yielded at room temperature. The residual radial stress is compressive and the hoop and axial

stresses are tensile in the matrix. Large deviatoric stresses are created around the fiber. One can observe that plastic flow in the matrix has allowed a reduction of the thermal stresses with considering matrix plasticity by one order magnitude in comparison to the elastic case.

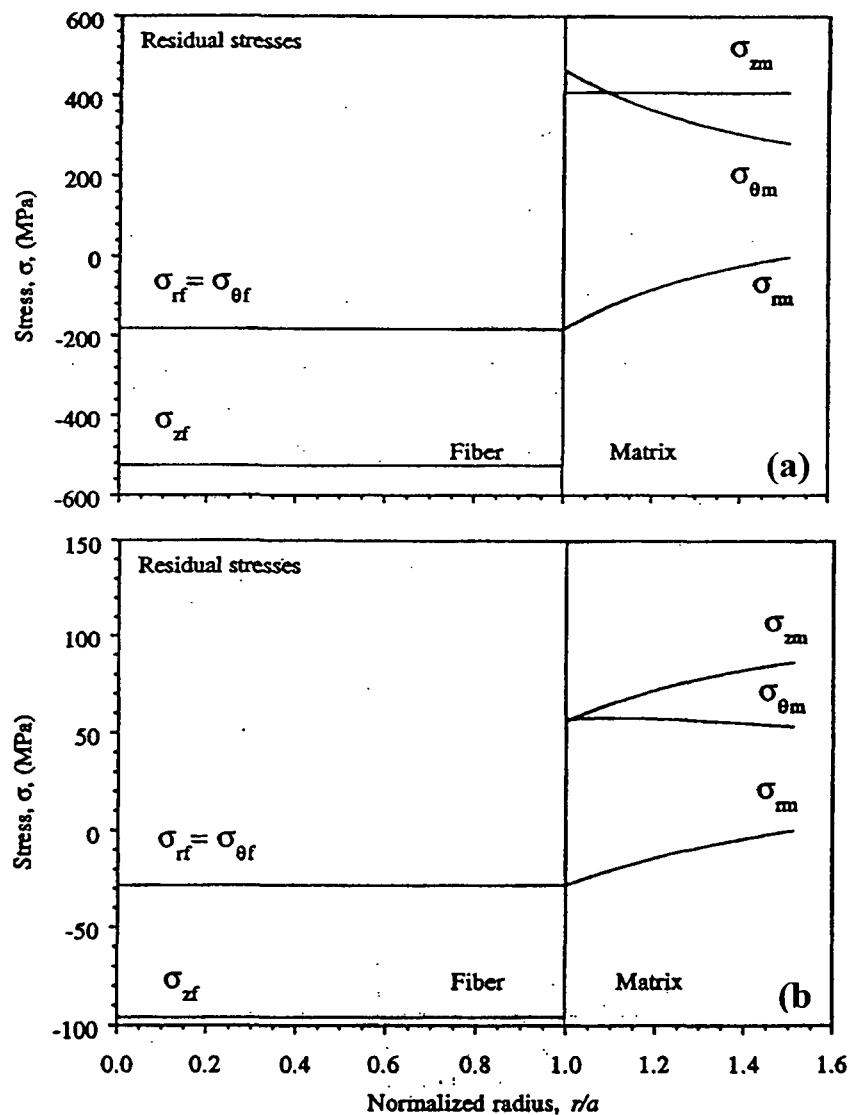


Fig.2-18, Thermal residual stress distributions in the fiber and matrix at room temperature after cooling from 288°C as a function of normalized radial distance, a) without considering plastic flow of the matrix, b) considering plastic flow of the matrix, subscripts z, θ , r for axial, hoop and radial stresses, respectively, and m and f for matrix and fibers, respectively[42].

F. Chmelik et al., used a formula to predict the thermal stresses σ_{TS} , produced by a temperature change ΔT at the interfaces as

$$\sigma_{TS} = \frac{E_f E_M}{(E_f v_f + E_M (1 - v_f))} v_f \Delta \alpha \Delta T \quad (2.5.9)$$

where E_f and E_M are the values of Young's modulus for the reinforcement and the matrix, respectively, V_f is the volume fraction of fibers and $\Delta \alpha$ is the thermal expansion mismatch between the matrix and the reinforcement associated with the coefficient of thermal expansion. He applied this formula for the saffil short fibers reinforced AZ91 magnesium alloy.

Thermal stresses in the matrix of SiC particulate reinforced Al have been studied using X-ray diffraction during thermal cycling by H.Li et al [43]. As shown in Fig. 2-19, upon heating from room temperature, the tensile stress at first relaxes elastically, and then the compressive stress develops because of the larger thermal expansion of Al matrix. Eventually, the yielding of the matrix in compression is observed as a deviation from the elastic line (point B). With further heating after yielding, the compressive stress develops and passes through a maximum followed by a gradual decrease of compressive stress up to point C, which implies that more plastic deformation takes place in the local region of the matrix due to the localized stress concentration. During cooling from the maximum temperature, the compressive stress at first relaxes to zero because the matrix contracts faster than does the reinforcement. On further cooling, a tensile stress develops in the matrix, and this cause plastic deformation in tension to occur. After yielding the tensile stress remains almost constant with continuing in cooling. They also observed that the tensile stress on the matrix after cycling is much lower than the start point and they attributed that to difference in cooling rate between production and testing.

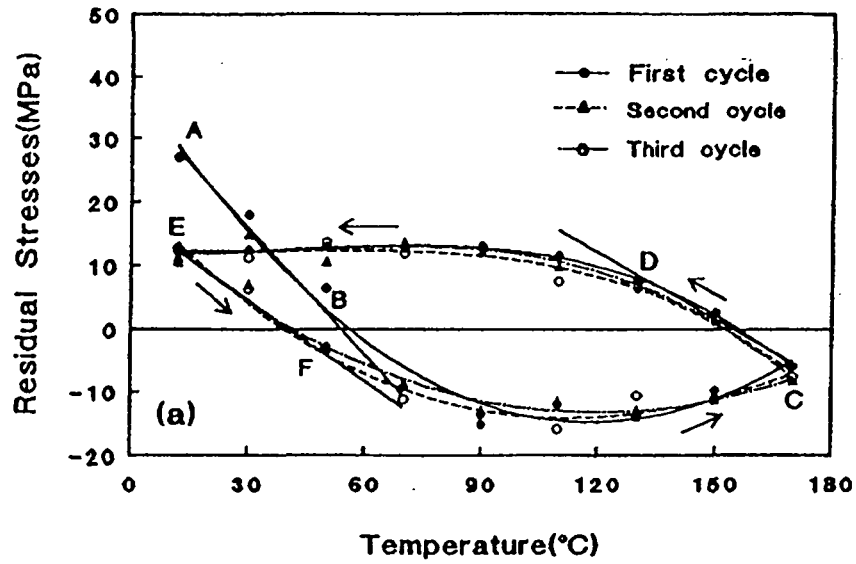


Fig.2-19, Stress temperature plot for the matrix in composite during thermal cycling, starting at A [43].

3.1. Materials

From the point of view that the properties of the continuous fiber reinforced metal matrix composites (CFRM) depend not only on the properties of the constituents: fiber types and matrices, but also on the fiber direction and arrangements, mechanical and thermal properties for metal matrix composites have been determined for different variables between fibers and matrices in different fiber orientations.

Matrices were mainly commercially pure aluminium, commercially pure magnesium, with some addition of magnesium and aluminium, respectively. Fibers are PAN carbon fibers of high modulus or high tensile strength, and alumina Nextel610 fibers. Arrangements of the fibers are unidirectional, woven, and stacked symmetric arrangements.

The different information on the matrices, fibers and arrangements are listed in table 3-1, and an overview of the properties of fibers is in table 3-2.

Table 3-1, Matrices, fiber types and arrangements of investigated CFRM.

Production no.	Matrix material	Fibers	Received as, mm ³	Vo%	Fiber arrangement	Produced in	Abbreviation
Y424	MgAl0.6	C-M40B	Plate 150x65x2	65	UD	LKR-Ranshofen	Mg/C-UD
V415, V416	AlMg0.1	Al ₂ O ₃ -Nextel		65	UD		Al/Nex.-UD
V409, V410	Al99.85	C-M40B		65	UD		Al/C-UD
	Mg99.8	C-Tenax-HTA5331	Plate 77x65x2	55	UD		Mg/Tenax-UD
Y224	Al99.85	C-M40B	Plate 150x65x2	64	Stacked 6 layers 0,+ 60,-60, -60,+60,0		6 Layers symmetric
ILK-MMC43	MgAl0.2	C-T300J	Samples 10x5x2	50	0/90 woven, 50/50	ILK-Dresden	Mg/C-woven 50/50
ILK-MMC59,60	MgAl0.2	C-T300J		50	0/90 woven, 80/20		Mg/C-woven 80/20

Table 3-2, Fiber properties [6,44-46]

	C-M40B		C-T300J		Al ₂ O ₃ Nextel610	C-Tenax HTA5331- Long
	Long.	Trans	Long	Trans		
Tensile strength, MPa	2740	-	4210	-	3000	3977
E-modulus, GPa	392	6.2	230	14	373	237.7
Density, gm/cm ³	1.81		1.78		3.88	1.75
Fiber diameter, μm	7		7		11.3	7
α, ppm/K ^o	-0.6	~10	-0.43	~10	7.9	-0.1
Main constituent	>99%C		94%C		>99% α- Al ₂ O ₃	
Ultimate tensile strain, %	0.7	-	1.8	-		1.59

* Temperature range not specified

3.2. Determination of reinforcement volume fraction

Determination of fiber volume fraction was done by using diluted hydrochloric acid (50% acid, and 50% water) to dissolve the matrix following these steps respectively:

- a- Determining the density of the composite specimen using the following equation:

$$\rho_c = \{ [W_a \cdot (\rho_{fl} - 0.0012)] / 0.99983G \} + \rho_a$$

Where:

ρ_c = density of composite specimen, g/cm³

W_a = weight of specimen in air, g

ρ_{fl} = density of the liquid, g/cm³

G = buoyancy of the immersed solid, g

G = $W_a - W_{fl}$

W_{fl} = weight of specimen in water, g

ρ_a = density of air under standard conditions, g/cm³

b- Dissolving the aluminium matrix by diluted HCl using temperature of approximately 100°C.

c- Determining the fiber weight, then substituting in this equation:

$$\xi_f = (W_f / \rho_f) / (W_a / \rho_c)$$

Where:

ξ_f = volume fraction of fibers, W_f = Fibers weight, g

ρ_f = Fibers density, g/cm³.

3.3. Determination of mechanical properties

Because of the importance of the mechanical properties, a great number of experimental techniques have been developed. Those techniques can be classified into two main groups

- Static techniques
- Dynamic techniques

Static methods are based on direct measurements of stresses and strains during mechanical tests, for instance, tensile, compressive, and flexural. Dynamic techniques to determine the stiffness provide an advantage over static techniques because of great precision, and measurement even at high temperatures. Dynamic techniques can be classified into two groups, resonance and pulse methods. In principle resonance methods based on setting the sample into mechanical (sonic and/or ultrasonic) vibration in one or more frequency at which the vibrational displacements are at a maximum (resonance). Samples can be excited to vibrate by drivers having continuously variable frequencies output. Vibrations of the samples are monitored by detecting transducers and analyzed in order to determine its characteristic frequencies. Knowing the vibrational mode, frequency dimension and density of the samples, it is possible to calculate the elastic constants of the material. Pulse techniques are based on measuring the transit time, which is the time spent for the ultrasonic pulse to travel through the specimen from the transmitting to the receiving transducer. By knowing the

dimensions and density of the samples and the transit time, it is possible to calculate Young's and shear moduli of the material.

3.3.1. Four point bending test

Four point Bending test was made at room temperature by Zwick universal test machine linked with testxpert software which was used to calculate and record the experimental data. Fig.3-1 shows schematically the configuration of the test. The distance between the lower cylinders (L_V) is 45mm and the distance between the upper and lower (L_A) is 12.5mm. The data were obtained in the form of stress vs. strain if no loops of loading and unloading of force were used in testing. If looping was used then the data obtained in the form of deflection versus force and the E- modulus, stress and strain were calculated [47] by using the following equations, which hold as long as the beam deforms elastically and is strictly valid only for isotropic materials

E-Modulus E in kN/mm²:

$$E = [L_A * (3 * L_V^2 - 4 * L_A^2) * (X_H - X_L)] / (4 * \Delta L * b_0 * a_0^3) \quad (3.3.1)$$

L_A : Mid span in mm L_V : Support separation in mm

X_H : End of E-Modulus determination in kN

X_L : Beginning of E-Modulus determination in kN

ΔL : Flexure in mm between X_H and X_L

b_0 : Specimen width in mm

a_0 : Specimen thickness in mm.

Flexural stress in N/mm²:

$$\sigma = [(3 * L_A) / (b_0 * a_0^2)] * F = F_{Factor} * F \quad (3.3.2)$$

F: Force in N

F_{Factor} : Conversion factor for force to stress in 1/mm²

Strain in %:

$$\epsilon = [(1200 * a_0) / (3 * L_V^2 - 4 * L_A^2)] * f = S_{\text{Factor}} * f \quad (3.3.3)$$

f: Flexure at the specimen centre in mm S_{Factor} : Conversion factor for travel to strain in %/mm.

The Specimens were machined from plates by slicing the plates into strips with different orientations to the main axis with angles 0, 30,45,60 and 90 degrees using diamond cutting wheel in accutom-5 machine with dimensions of 65 x 5 x2 mm.

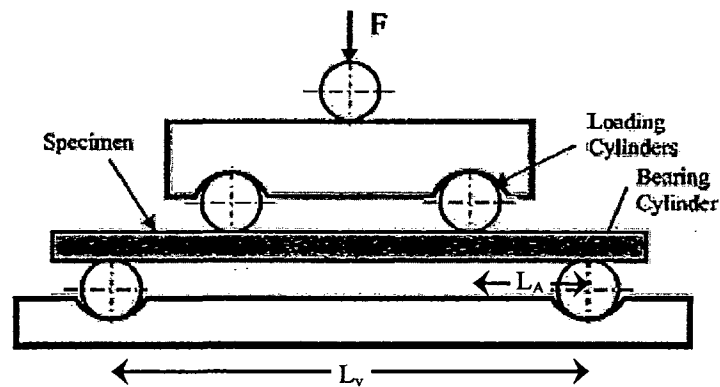


Fig.3-1, Schematic representation of four point bending test.

3.3.2. Dynamic mechanical analysis

3 point bending test was done on samples of dimensions $55 \times 2 \times 2 \text{ mm}^3$ with dynamic mechanical analyzer (DMA) 2980 linked with a TA instruments controller and associated software to make up a dynamic mechanical analysis system (Fig. 3-2). Young's modulus determined in the temperature range of 25 to +450 °C with a heating rate of 1K/min and different frequencies of 1, 5, 10, 50, and 100 Hz. Results were obtained from the average of the five different frequencies for every direction.

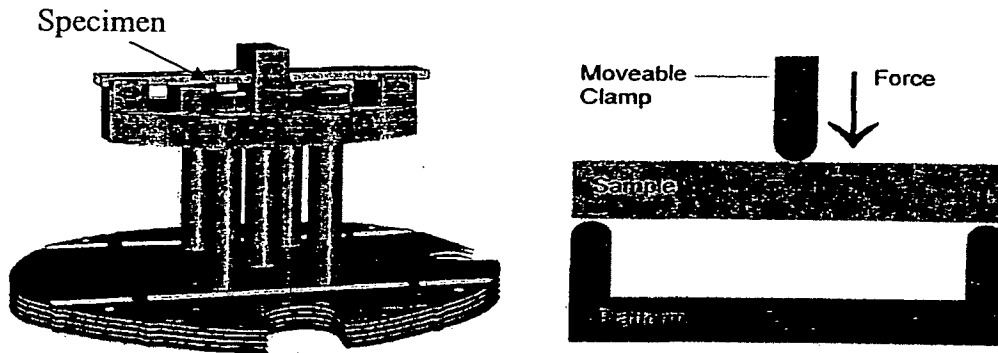


Fig.3-2, Schematic of the three point bending clamp used in the TA Instrument DMA 2980 [48].

3.3.3. Resonance bar technique

The device consists of rectangular wooden plate and four poles fixed one at each corner of the rectangle with the dimension shown in Fig.3-3. A rubber band stretched around the poles was used to support the tested plate in its nodal lines of its first free flexural vibration [49,50]. The vibration initiated by a coil screwed in the center of the wooden plate and a small magnet glued in the center of the examined plate. The coil was linked with a frequency generator (Processor multifunction generator ELV FG9000). A sound level measuring device was supported at one end of the examined plate to measure the eigen-frequency for the examined plate. A theoretical eigen-frequency of isotropic rectangular bending plate is given by the following equation

$$f_1 = \sqrt{\frac{1}{1-\nu^2}} \cdot \sqrt{\frac{E}{\rho}} \cdot \frac{h}{L^2}$$

where,

f_1 = eigen frequency, ν =Poisson's ratio, E =modulus of elasticity

ρ = density, h =thickness of the plate, and L =length of the plate.

This method was used to determine modulus of elasticity for as received plates for carbon fibers reinforced magnesium matrix and Nextel alumina fibers reinforced aluminium.

3.3.4. Resonant beam technique

Young's modulus and shear modulus were determined using Elastotron2000 instrument (Fig.3-4) for unidirectional fiber reinforced materials. This instrument designed to measure elastic moduli at high temperature up to 2000°C.

Prepared specimens, of which the surface skin was ground off, were suspended by two loops of carbon fiber bundles under vacuum and excited to bending vibrations via the loops. The carbon fiber loops are directly connected to the piezoelectric transmitter and receiver units as shown in Fig.3-4b. Data acquisition and evaluation for Young's and shear moduli are delivered on line by a single software package including an effective user interface design and run on a standard personal computer [51-53]. The dimension of the specimens were $80 \times 10 \times 2 \text{ mm}^3$ for the longitudinal specimens and $65 \times 10 \times 2 \text{ mm}^3$ for the transverse specimens.

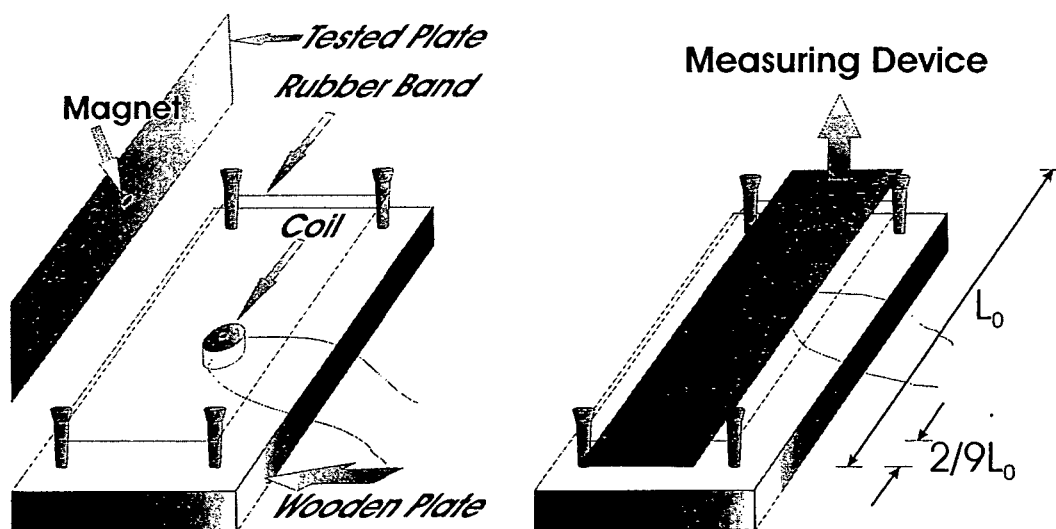


Fig3-3, Schematic representation of the resonant bar technique, showing the construction before measurements (left) and during measurements (right).

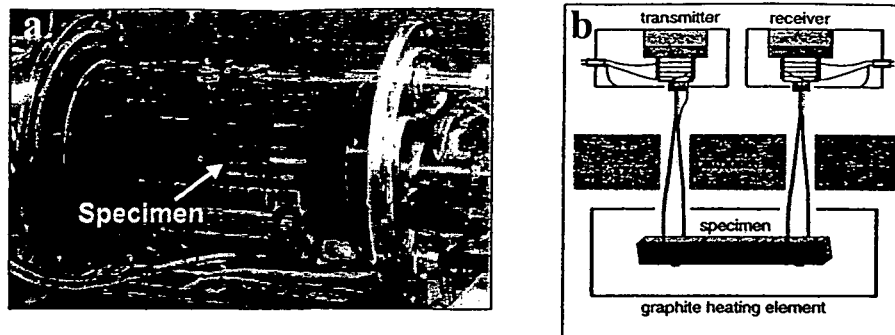


Fig. 3-4 (a) ELASTOTRON 2000 with open vacuum chamber and specimen, (b) scheme of the apparatus, the prismatic specimen is excited to bending vibrations by carbon fibre-bundle loops attached to transducers in water-cooled housing [53].

3.3.5. Laser ultrasonic technique

The use of pulsed laser to generate broad band acoustic signals is now established [54-57]. A localized temperature rise due to absorption of the low power pulse produces transient thermoelastic stress. Stress components normal to the surface are relaxed at the surface and the stresses are approximately biaxial in the plane of the surface. At high power level the laser source operates in the ablation regime by vaporizing a small amount of surface material. Laser ultrasonic uses short pulse laser for generation of thermoelastic waves and a long pulse laser coupled with optical interferometer for detection of ultrasound.

Fig.3-5, shows schematic diagram for point source-point receiver techniques used in the measurements. Sections from the received plates were examined by the PS-PR technique, taking into account the inclined wave propagation through the sample. The minimum region tested shall be wider than 2,5 times the specimen's thickness in all directions, where the receiver is placed. A detection distance of zero means that the source point and the receiving point are opposite with a distance equal to the sample thickness. For a varying detection distance, as shown in Fig.3-5, we get longitudinal and slower transverse waves and also multiple reflections for waves running 3 or 5 times through the sample thickness.

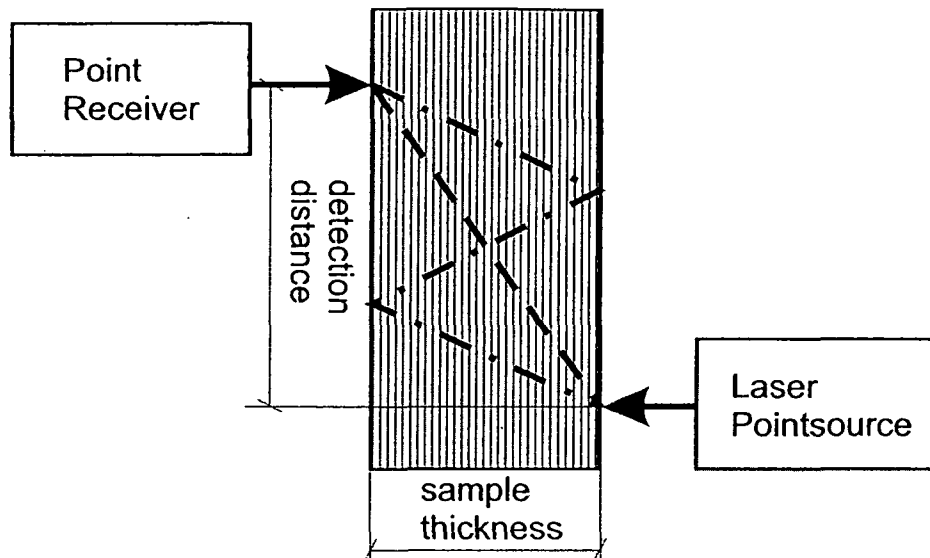


Fig.3-5. Schematic diagram of the ultrasonic laser point-source-point-receiver method [57].

3.4. Thermal expansion measurements

Thermal expansion has been measured by two different devices depending on the output wanted. The use of the material is intended to be in the range of -20 to 180°C , and the instrument suitable to use at subzero temperature measurements is the thermomechanical analyzer with cooling head. A dynamic dilatometer was used for detecting the damage produced as a result of thermal cycling, high heating and cooling rates.

3.4.1. Thermomechanical analyzer

TMA 2940 Thermomechanical Analyzer (TA Instruments) measures dimensional changes in a material as a function of temperature or time under a controlled atmosphere. Its main uses include accurate determination of changes in length, width, thickness, and coefficient of linear thermal expansion of materials.

A schematic diagram of the instrument is shown in Fig. 3-6. The heart of the device is a movable core linear variable differential transformer (LVDT), the

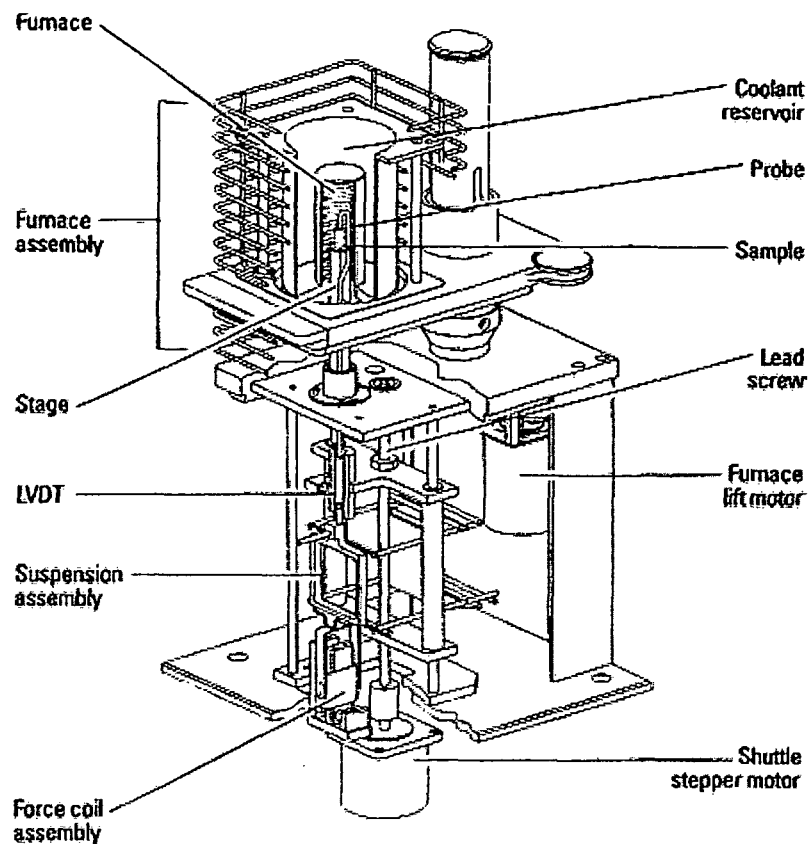


Fig.3-6, TMA 2940 schematic [58].

output of which is proportional to the linear displacement of the core caused by changes in sample dimensions. The core itself is a part of quartz probe that contacts the sample. Temperature control of the sample is achieved by programming a low mass furnace that is automatically lowered to surround the sample and probe. A thermocouple adjacent to the sample ensures accurate measurements of temperature [58]. A temperature calibration using the melting point of three standard materials Indium (156.6°C), Lead (327.5°C), and Zinc (419.6°C) were used to achieve accuracy of ± 1 K for temperature measurement [59,60].

A reservoir around the furnace core accommodates addition of coolant for programmed cooling and operations under room temperature. For temperature

homogenization inside the furnace atmosphere, nitrogen filled the furnace during experiments (100ml/min).

The force applied to the sample is generated by an electromechanical coil and calibrated first by weights, eliminating the need for mechanical weights during experiments. The attached resistance furnace has a temperature range of -70 to 1000°C, but the limitation of using subzero temperature range is restricted by the cooling head temperature range (-70 to 400°C). These features make the instrument suitable for evaluating the effects of dimensional change at temperatures from -70 to 400°C or without cooling head up to 1000°C under forces from 0.1 to 1.0 N acting via a stamp of 6 mm².

Aluminium standard specimens were used for calibration. This operation is done by a thermal cycle 20°C below and above the temperature range used in the experiments. The cell constant is obtained by dividing the CTE value as a standard value by that obtained from the measurements. The calculated cell constant is then introduced into the software for calibration of the instrument.

Samples from different materials and with different directions to main fiber axis were cut in the dimensions of 15x5x2 mm³ using the acotom-5 machine, followed by leveling and polishing for the basal planes to achieve flat and parallel ends.

Almost all of the thermal expansion measurements were done in the first two cycles in the interval of -40 to +120 °C, and in the next two cycles in the interval -40 to +200 °C as shown in Fig.3-7. The heating and cooling rate used is ±3 K/min, with a load of 0.5 N. Results were obtained from the average of three samples for each direction. Cooling from room temperature is faster than 3 K/min. and a holding period of 5 min. is introduced before heating starts.

The data were obtained in the form of dimension change versus temperature and derivation of dimension change versus temperature. The strain temperature curves were smoothed ±30K around each point to obtain the corresponding deviation. The coefficient of thermal expansion (CTE) was then calculated for an interval of temperature, (T-T₀).

For calculating the technical CTE, this equation was used [61]

$$\alpha_{\Delta T} = (L - L_0) / (T - T_0) L_0 \quad (3.4.1)$$

where:

L = length at T °C, T_0 = reference temperature (-40°C), and
 L_0 = original length (at -40°C).

And for instantaneous CTE,

$$\alpha_i = (dL/dT)(1/L)$$

where, L is the actual length of the specimen and T is the absolute temperature.

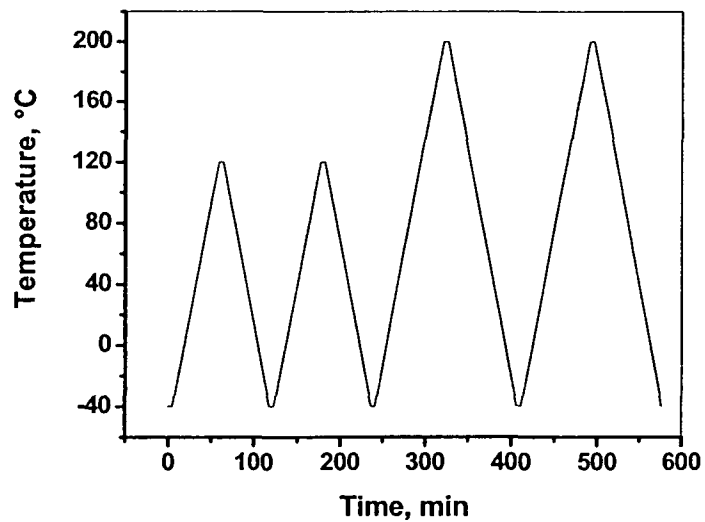


Fig.3-7, Thermal cycles used in TMA measurements for different MMCs.

3.4.2. Dynamic dilatometer

For complicated thermal cycles, i.e. different cooling and heating rates, a dynamic dilatometer (Bähr DIL 805) was used (Fig.3-8). With this type of dilatometer a heating rate of 1000K/s can be used due to the induction furnace surrounding the specimen, and a high cooling rate could be achieved depending

on the specimen geometry, thermal conductivity and the cooling gas with a maximum of 1600K/s [62].

Specimens with the same dimensions and conditions as TMA were used for unidirectional carbon fiber reinforced aluminium and magnesium matrices.

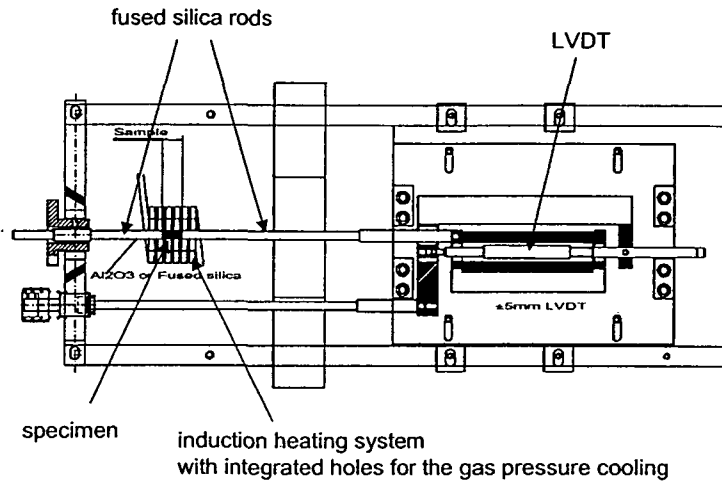


Fig.3-8, Schematic drawing of the dynamic dilatometer DIL 805 [62].

3.5. X-ray computer microtomography

Computed X-ray tomography (XCT) reveals the 3-dimensional structure of composite materials by mapping the local X-ray absorption of a sample [63]. Small specimens ($5.2 \times 2 \times 15 \text{ mm}^3$, the same as used for dilatometry) were introduced into a Skyscan 1072 Desktop Micro-Tomograph [64] with an 80 kV microfocus X-ray tube, an area detector and a CCD-camera for recording (Fig.3-9). The reconstruction of the X-ray absorption yields relative gray values, which can be calibrated by measuring simultaneously reference samples of similar size: massive Al and a piece of porous graphite ($\rho = 1.42 \text{ g/cm}^3$), which requires a correction for the density of the C-fibers that is about 25% higher. The achieved spatial resolution is about $10 \mu\text{m}$ based on a voxel size of a cube of $6.3 \mu\text{m}$ edge

length. Individual fibers cannot be resolved, but the local fiber volume fraction yields the corresponding absorption represented by 256 gray levels.

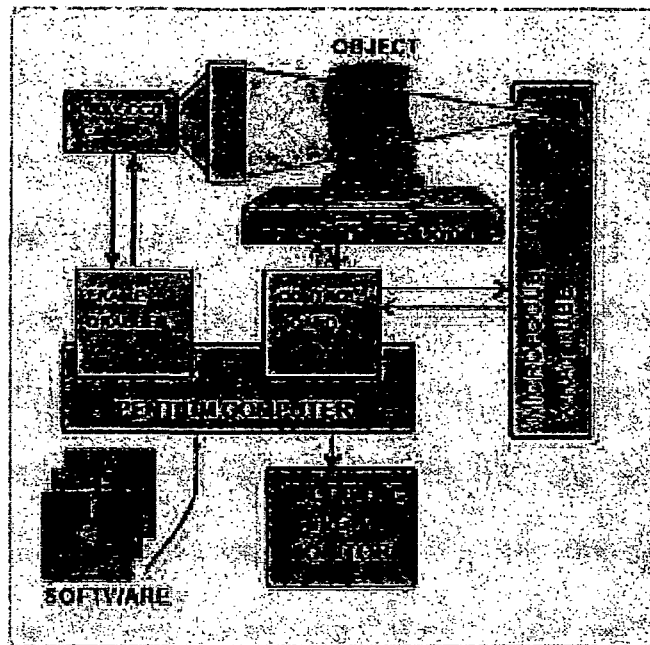


Fig3-9, Skyscan 1072 Desktop Micro-Tomograph [64].

3.6. Gleeble compression test

Compression test for the matrix materials has been done using Gleeble 1500 machine. The Gleeble 1500 Thermo-Mechanical Simulator is capable of heating specimens by direct resistance heating. This employs a low voltage 50Hz AC current which is passed directly through a cylindrical specimen with a diameter of 10 mm and length of 15 mm, so that the resistance of the specimen itself generates the heat by the Joule (I^2R) effect. Temperature measurement is by means of thin wire thermocouples percussion welded to the surface of the specimen. A closed loop feedback signal then enables precise control of the heat

input based on the temperature at any instant. Specimens were tested at 50, 100, 150, and 200°C to determine the constitutive behavior of the material and determining the hardening modulus. On the other hand, heating up for constrained specimens of pure aluminium and magnesium has been done for determining stress and temperature under which yielding of the matrix occurs.

4. Results

4.1. Metallography

Optical microscopy has been done to confirm the infiltration quality, fiber distribution, and to execute sometimes volume fraction measurements by image analysis. Cross sections for different unidirectional metal matrix composites are shown in Fig.4.1(a-f). The soundness of the samples is a clear indication for good infiltration of the liquid matrix into the fiber preform. Two different magnifications for each MMC material are shown, low magnification for overall view and higher magnification for fiber distribution and closer investigation. Fig 4.1a,b, show carbon fibers reinforced aluminium (Al/C-M40B), in Fig 4.1a channels of matrix between fiber bundles and asymmetric matrix skin from both specimen surfaces were observed, these features cannot be observed in the higher magnification Fig4.1b. Carbon fibers reinforced magnesium (Mg/C-M40B) is shown in Fig 4.1c,d. The nonuniform bean shaped cross section is characteristic for the M40 carbon fibers with a diameter of about 7 microns, conversely the uniform circular cross section of the alumina fibers is clearly observed in Fig.4.1e,f, for alumina Nextel fiber reinforced aluminium (AlMg0.6/Al₂O₃ Nextel610).

Fig.4-2 (a-d), shows T300J carbon fibers plain woven fabric reinforced MgAl0.2 MMCs (MgAl0.2/C-T300J/0,90°). The lengthwise set is called warp and the crosswise set is called fill. Fig 4-2 (a,b) shows inplane and cross sectional view for 50% of fibers in the warp direction and 50% of fibers in the fill direction, while Fig 4-2 (c,d) shows the same sections for 80% of fibers in the warp direction and 20% in the fill direction.

Fig.4-3(a,b) shows symmetrically stacked carbon M40B fibers reinforced aluminium (Al/C-M40B) in the direction of 0,+60,-60,-60,+60,0 stacking sequence. The observed fiber depleted areas, specially in the later two systems and even in the unidirectional MMC materials, as veins of matrices are due to the

inhomogeneity of compression of the fibers by the non-wetting liquid matrix before infiltration.

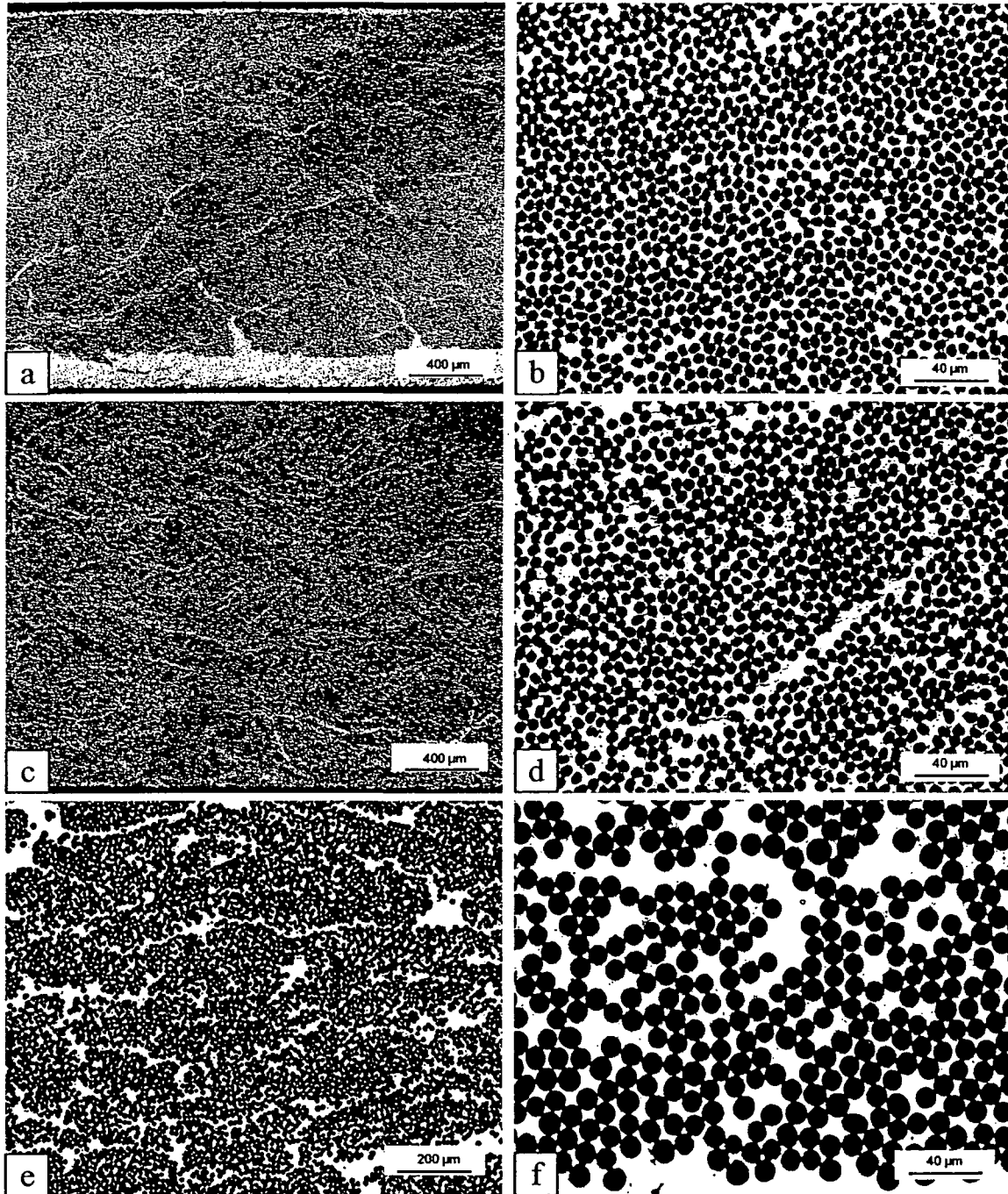


Fig. 4-1: Optical micrographs showing cross sections of the unidirectional composites: (a),(b) Al/C-M40B/65f-UD; (c),(d) MgAl_{0.6}/C-M40B/65f-UD; (e),(f) AlMg_{0.6}/Al₂O₃-Nextel610/65f-UD.

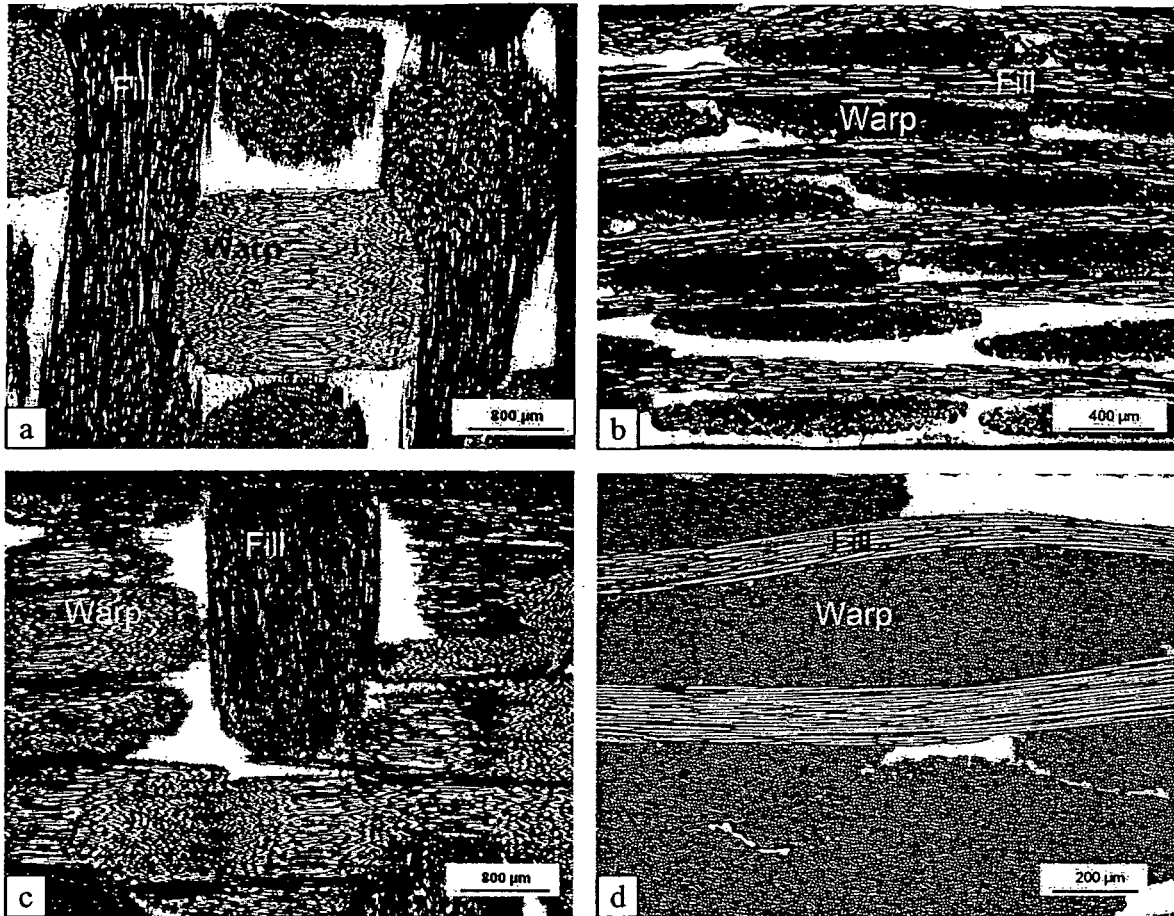


Fig. 4-2: Optical micrographs of the Mg composites with woven C-fiber fabrics:
 (a) inplane, (b) cross-sections of MgAl_{0.2}/C-T300J/55f (0/90°, 50/50%)
 (c) inplane, (d) cross-section of MgAl_{0.2}/C-T300J/55f (0/90°, 80/20%).

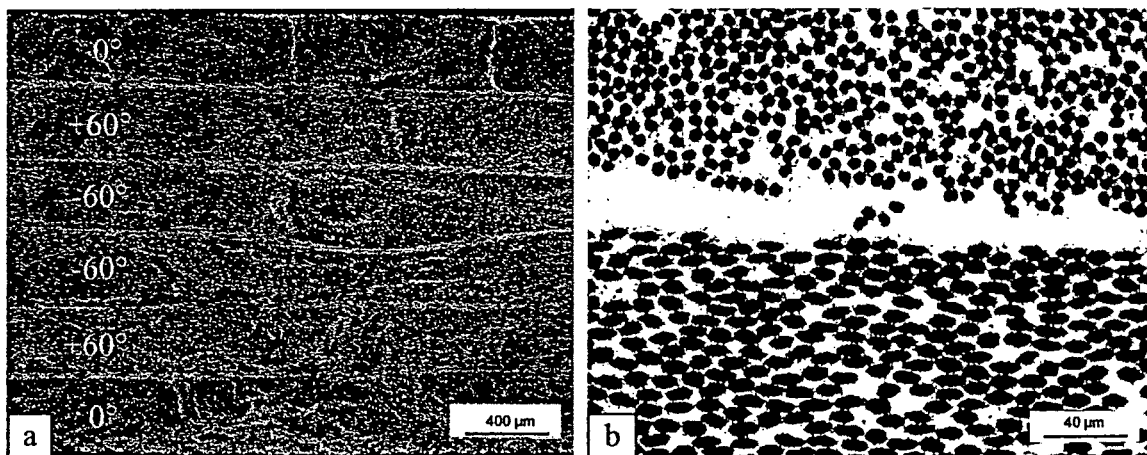


Fig. 4-3: Optical micrographs of the symmetric 6 layers of Al/C-M40B showing in a) the stacking sequence 0°, +60°, -60°, -60°, +60°, 0°; and in b) matrix veins between the layers and the bundles.

4.2. Four point bending

Mechanical properties of fibrous composites are known to be strongly dependent on the fiber orientation. Orientation of the fibers with respect to the loading axis is an important parameter, which affects the distribution of load between the fibers and the matrix. The contribution of the fibers to the composite's properties maximize when they are parallel to the loading direction, and the extent to which they are reduced depends on the angle of fibers to the loading axis.

4.2.1. MgAl_{0.6}/C-M40B/65f-UD MMC

Determination of stiffness for the longitudinal samples is easy as the elastic portion is broad enough for the stiffness determination. Conversely, for the off axis specimens where there is a deviation from the fiber direction, the elastic portion is narrow and leads to uncertain values and composite materials start to behave like ductile materials. For this reason loading-unloading cycling gives more accurate results for stiffness determination.

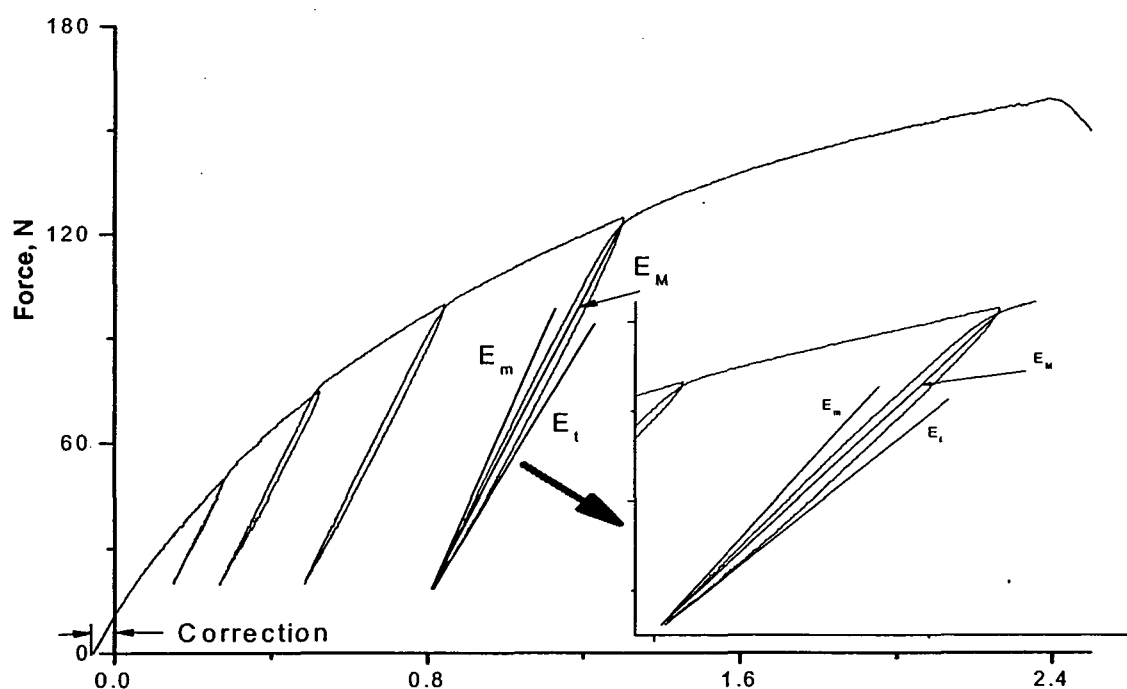


Fig.4-4: Determination of stiffness values by loading-unloading cycling.

Fig.4.4 shows schematic diagram for the three stiffness moduli maximum (E_m), tangential (E_t), and mean (E_M). Correction for the strain values has been done by extrapolation to a true zero value in the stress strain curve. Fig 4.5. shows a set of specimens in different directions 0, 30, 45, 60 and 90° to the fiber direction, the max. stiffness value in the longitudinal direction sample is about 230 GPa, yield strength of 800MPa, and a breaking strength of 1240 MPa at 0.55% Strain, while table 4.1 shows the average of stiffness and strength values for different fiber directions. The anisotropy of stiffness values is clearly observed, the value at 30° is 30% of the longitudinal value and the lowest is for the transverse direction with 8% of the longitudinal value. The same trend observed for the strength with a value for 30° of 13% of the longitudinal value and for transverse samples of 2% of the longitudinal samples.

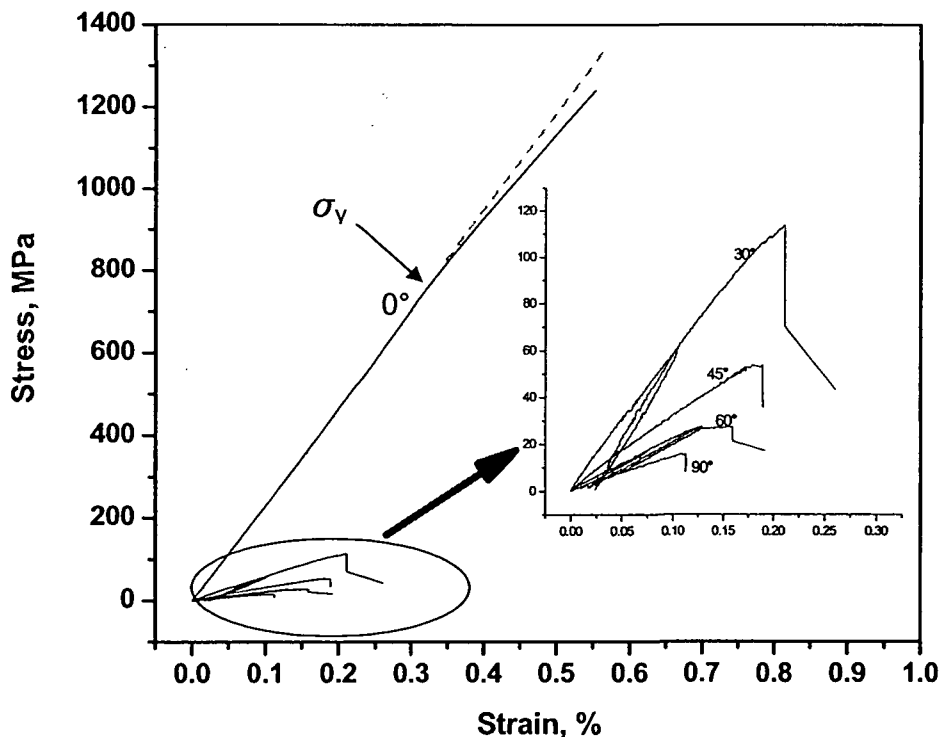


Fig.4-5: Stress-strain curves for MgAl_{0.6}/C-M40B/65f MMC for a set of specimens with different fiber directions.

E_t was determined when the unloading-loading hysteresis indicated a difference close to the point of the lower stress reversal. The stress, where E_m transforms into E_t , means that the matrix starts to yield reversibly. The area of the hysteresis loop represents the damping of CFRM. A yield stress is indicated in Fig. 4-5, where the slope of the stress-strain curve changes, which is caused by successive fiber fracture along the tension side of the longitudinal bending samples. The yield strength values in table 4.1 for inclined specimens were determined at 0.1 % strain. The remaining permanent strain at fracture is calculated from the total strain by subtracting the elastic strain calculated using the determined Young's modulus.

Table 4.1: Average stiffness and strength values for MgAl0.6/C-M40B/65f.

Angle	Maximum stiffness	Mean stiffness	Tangential stiffness	Yield strength	Breaking strength	Strain to failure %		
	GPa E_m	GPa E_v	GPa E_t	MPa $\sigma_y (E)$	MPa R_m	Elastic	Plastic	RAM
0	245	245	245	800	1140±100	0.33	0.22	0.55
30	72	74	64	60	153±4	0.08	0.20	0.28
45	46	37	30	20	73±1	0.05	0.20	0.25
60	22	21	19	18	31±2	0.09	0.08	0.17
90	21	20	17	8	25±7	0.04	0.16	0.20

4.2.2. AlMg0.6/Al₂O₃-Nextel610/65f

The same procedure as in sec.4.2.1 had been used for AlMg0.6/ Al₂O₃-Nextel610/70f. Fig. 4.6 shows a set of samples for different fiber directions 0, 30, 45, 60, and 90° to the main fiber direction. The stiffness value in the 30° direction has 79% of the longitudinal direction, while the transverse has 69% of the longitudinal specimens. The specimens in 30 and 45° did not break but twisted as seen in Fig 4.7. As can be seen from table 4.2, there is little difference in the stiffness values between the 45, 60 and 90° directions, while the transverse stiffness value is a little higher than that of the 60° direction specimens. For the

breaking strength values the transverse specimen has 25% of the longitudinal direction.

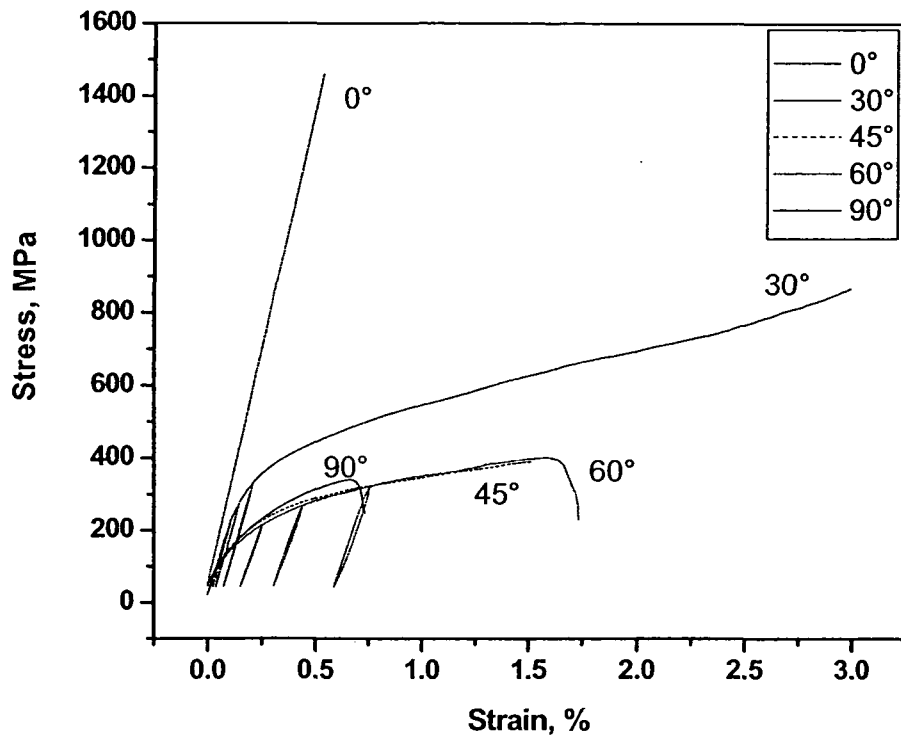


Fig.4-6: Stress-strain curves for AlMg0.6/ Al₂O₃-Nextel610/70f MMCs for a set of specimens with different fiber directions.

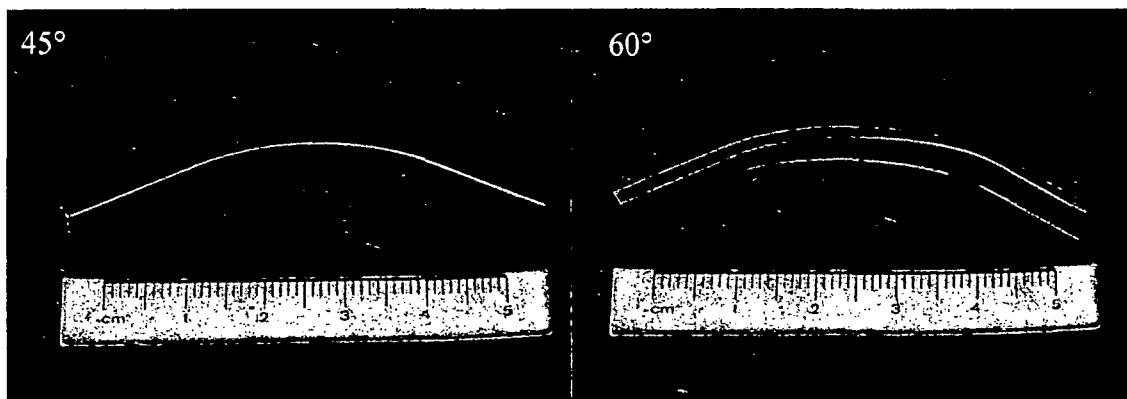


Fig.4-7: Twisted bending samples both 45 and 60° fiber directions for AlMg0.6/ Al₂O₃-Nextel610/70f MMC.

Table 4.2: Average stiffness and strength values for AlMg0.6/ Al₂O₃-Nextel610/65f MMC.

Angle	Max stiffness	Mean stiffness	Tangential stiffness	Yield strength	Strength at 0.2% strain	Breaking strength	Strain		
	GPa E_m	GPa E_s	GPa E_t	MPa $\sigma_y (E)$	MPa $R_{0.2}$	MPa R_m	Elastic	Plastic	Max.
0	262	262±9	262	1460	---	1460	0.6	<10 ⁻⁴	0.6
30	219	207±2	193	230	409	> 850	0.1	>2.9	>3
45	195	191±5	165	85	252	> 390	1.14	>7.45	>7.5
60	177	167±4	133	83	238	401	0.04	1.56	1.6
90	185	180±5	161	53-62	280	369	0.03	0.67	0.7

4.2.3. Mg/C-Tenax HTA 5331/55f – UD

Four point bending test had been done for low modulus tenax carbon fibers reinforced magnesium with 55% fiber volume fraction. An average of three specimens in the longitudinal and transverse directions was tested, but only one specimen in other directions was examined because of lack of material availability. Fig. 4-8 shows stress strain diagram for different orientations. The longitudinal direction results are separated from the other directions because of relatively high strength. Values of mean stiffness, strength and maximum strain are summarized in table 4.3.

Table 4.3: Average stiffness and strength values for Mg/C-Tenax HTA 5331/55f MMC.

Angle	Mean stiffness	Breaking strength	Elastic strain	Plastic strain	Maximum strain
	GPa E_m	MPa R_m	%	%	% ϵ_m
0	118±20	1282±280	1.08	<10 ⁻⁴	1.08±0.06
30	43	44	0.10	1.63	1.73
45	26	24	0.09	1.18	1.27
60	21	17	0.08	0.82	0.9
90	20±1	15±4	0.08	0.83	0.9±0.2

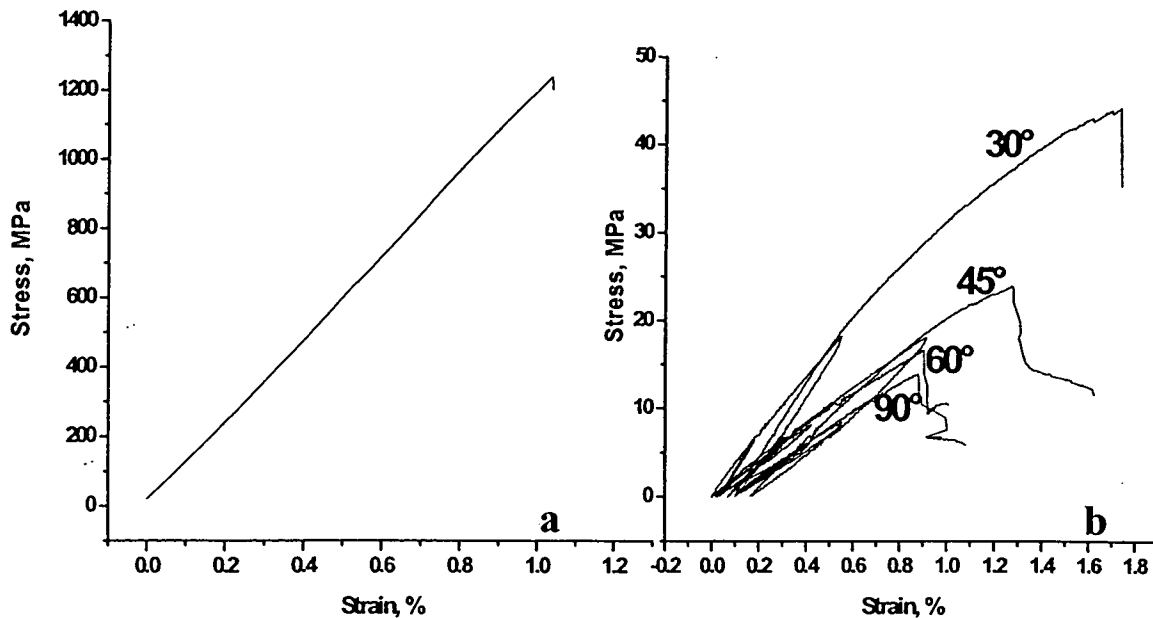


Fig.4-8: Stress-strain curves for Mg/C-Tenax HTA 5331/55f MMCs for a set of specimens with different fiber directions, a) Longitudinal direction, b) 30,45,60, and 90° directions.

4.2.4. Al/C-M40B/64f, (0, +60°, -60°, -60°, +60°, 0)

Bending test for various specimen directions 0, 15, 30, 45, and 90 degrees was carried out for determining strength and modulus of elasticity, and dependence of anisotropy on orientation. Three specimens were tested for every direction. The results were averaged for the stiffness and strength values.

As shown in Fig.4.9, although the arrangement of fibers is symmetric 6 layers, and the anisotropy should be minimized, the material showed anisotropic behavior, maximum strength and stiffness obtained when the outer fibers have 0 degree, i.e, axial direction, and minimum strength and stiffness when the outer fibers have 90 degrees, i.e, transverse direction. Table 4.4 shows values of stiffness and strength for individual specimens as well as the average values for different fiber arrangements.

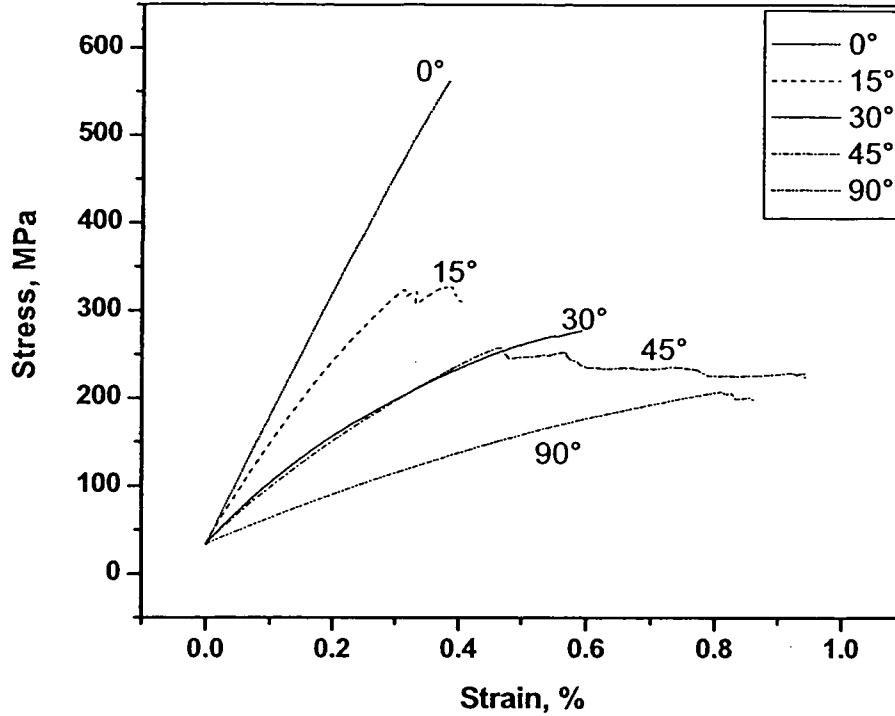


Fig.4-9: Stress-strain curves for 6 layers symmetric MMCs for a set of specimens with different fiber directions.

Table 4.4: Stiffness and strength values for Al/ C-M40B/64f -(0, ±60°, 60°, 0) MMC.

Specimen	Angle	E modulus GPa	Average E modulus GPa	Breaking strength MPa	Average breaking strength MPa	Breaking strain %	Av. Br. strain	Strain %	
								Elastic	Plastic
1	0	142	147 ±8	535	606 ±62	0.41	0.45 ±0.04	0.41	0.04
2		143		634		0.48			
3		156		650		0.46			
4	15	120	116 ±8	333	339 ±7	0.35	0.39 ±0.04	0.29	0.10
5		122		337		0.42			
6		108		346		0.41			
7	30	67	69 ±3	255	301 ±39	0.59	0.78 ±0.16	0.44	0.34
8		69		326		0.88			
9		71		322		0.86			
10	45	64	63 ±1	255	268 ±19	0.52	0.55 ±0.05	0.43	0.12
11		64		259		0.52			
12		63		290		0.62			
13	90	26	28 ±2	225	217 ±7	1.20	1.02 ±0.16	0.78	0.24
14		28		212		0.94			
15		29		214		0.92			

4.3. Dynamic mechanical analysis

Fig.4.10 shows the average storage modulus values for different orientations versus temperature from room temperature up to 450°C. For the longitudinal sample the storage modulus value was 302 GPa at room temperature and at 450°C. This value is increasing with increasing temperature up to about 305 GPa at 250°C and then drops down again at higher temperature. With increasing the orientation angle the modulus degrades drastically, at 30° the modulus value at room temperature is 79 GPa. No great difference exists between modulus values for 45° and 60°, which are 47 and 45 GPa, respectively. The lowest modulus values observed for the transverse direction is about 29 GPa. The values of storage modulus at different orientations on the fiber direction at different temperatures are listed in table 4.5.

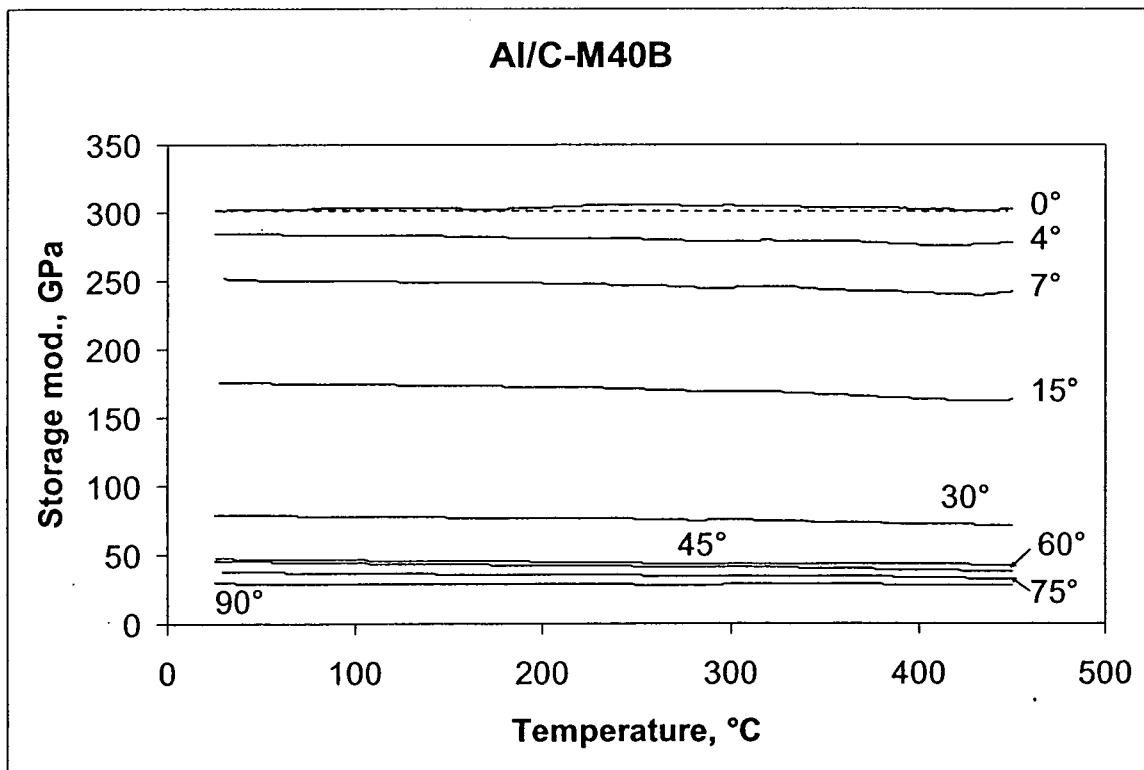


Fig.4-10: Storage modulus vs. temperature for Al/C- M40B/65f along different orientations.

Table 4.5, Storage modulus of Al/C-M40B in different fiber orientations at room temperature, 250°C and 450°C.

Angle	RT	%	250°C	%	450°C	%
0	302±2	100	305±3	100	302±2	100
4	284±2	94	281±3	92	278±3	92
7	252±2	83	247±2	81	242±3	80
15	176±1	58	171±2	56	163±3	54
30	79±1	26	76±2	25	71.3±2	24
45	47±1	16	44±1	14	42.4±2	14
60	45±1	15	41.6±2	14	37.3±2	12
90	29±1	10	28.3±1	9	27.3±2	9

4.4. Resonant beam technique

4.4.1. MgAl_{0.6}/C-M40B/65f-UD MMC

Fig.4-11(a,b) shows longitudinal stiffness and shear modulus during thermal cycling between room temperature and 200°C for carbon fiber reinforced magnesium using resonant beam technique. The stiffness value at room temperature is 226 GPa, which increases with temperature slightly by only one GPa difference and then decreases again to a value that equals the room temperature value. Shear modulus at room temperature is 13.3 GPa and decreased to 13 GPa at 200°C. No difference had been detected between heating and cooling cycles for both stiffness and shear modulus.

4.4.2. AlMg_{0.6}/Al₂O₃-Nextel610/65f

Fig. 4-12 and 13, show the stiffness and shear modulus values in both longitudinal and transverse directions, respectively. In the longitudinal direction the stiffness value at room temperature is 254 GPa and this value decreased to 250 GPa at 200°C, while the shear modulus in the same direction is 66 GPa at room temperature and decreased to 62.5 at 200°C. For the transverse direction the stiffness value of 177 GPa decreased to 164 GPa in the same temperature range, and the shear modulus is 71 GPa at room temperature decreased to 70 GPa at 200°C.

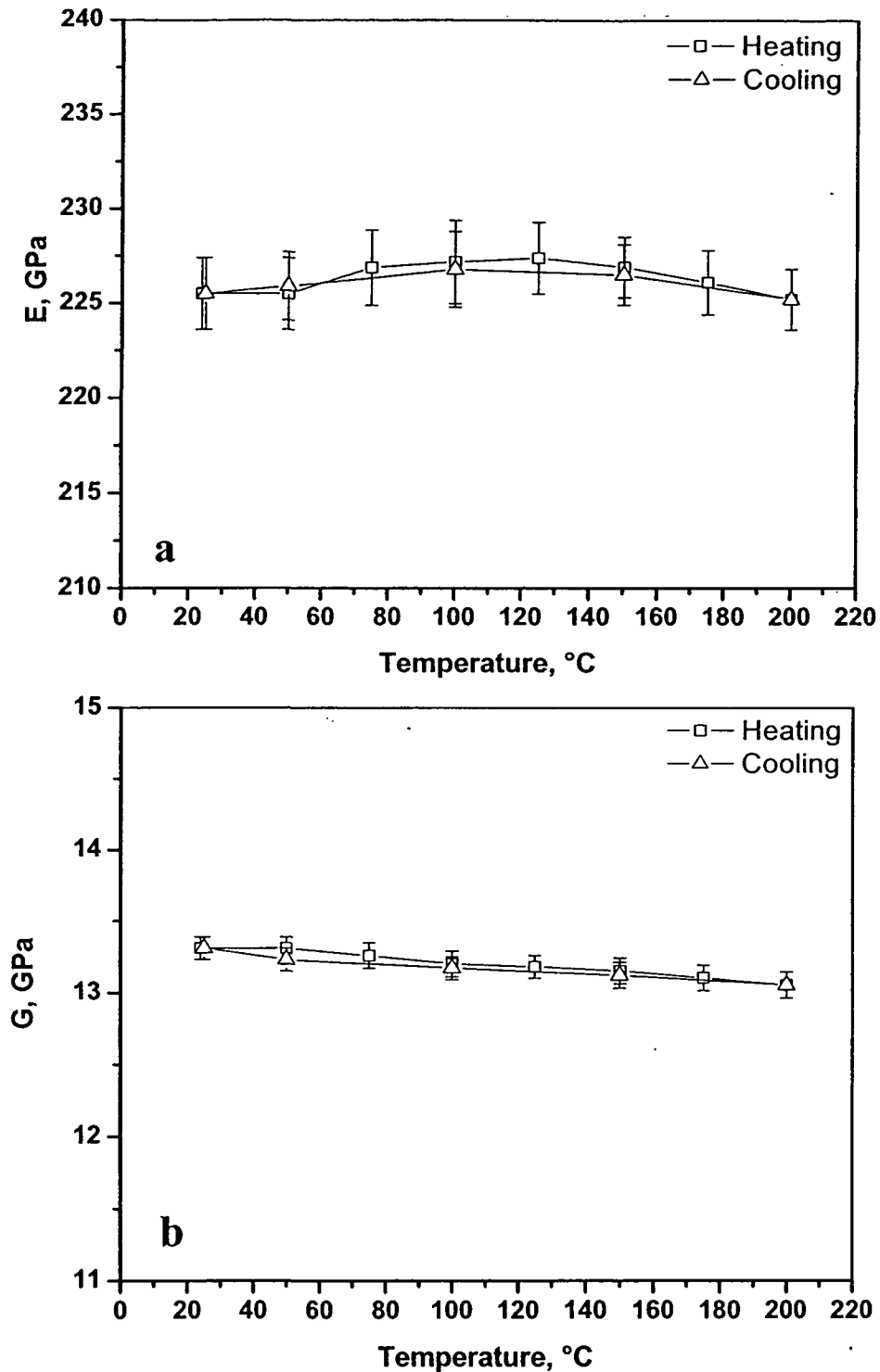


Fig.4.11, Results from the resonant beam technique for MgAl_{0.6}/C-M40B/65f-UD MMC in the longitudinal direction, a) Young's modulus vs. temperature, b) shear modulus vs. temperature.

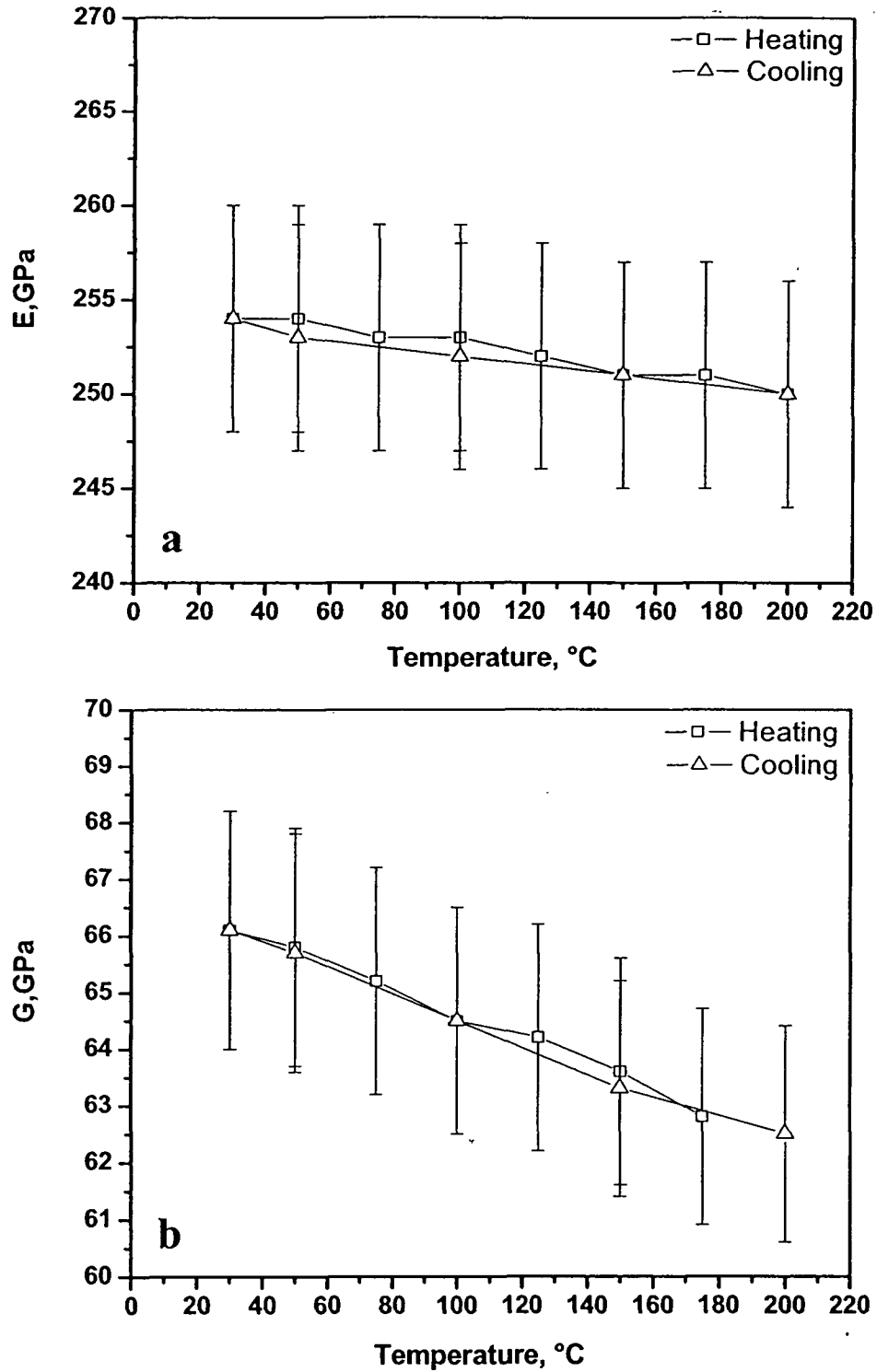


Fig.4.12, Results from the resonant beam technique for AlMg_{0.6}/Al₂O₃-Nextel610/65f in longitudinal direction. a) Young's modulus vs. temperature, b) shear modulus vs. temperature.

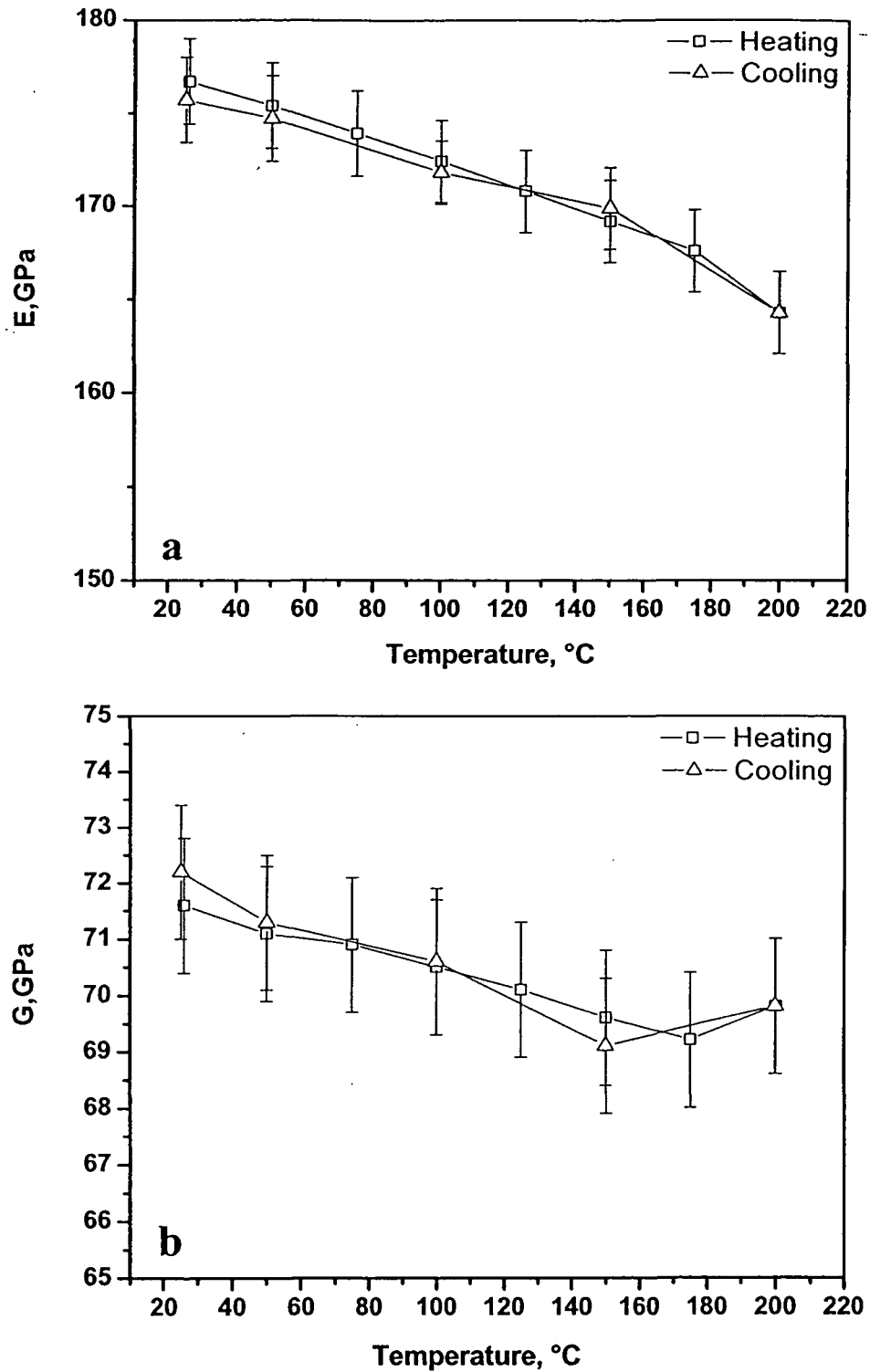


Fig.4.13, Results from the resonant beam technique for AlMg_{0.6}/Al₂O₃-Nextel610/65f in transverse direction. a) Young's modulus vs. temperature, b) shear modulus vs. temperature.

4.4.3. Al/C-M40B/65f

After removing the aluminium skin from the longitudinal specimen from both sides, the modulus of elasticity and shear modulus have been determined. The results for the longitudinal specimen were 257 GPa at room temperature for the modulus of elasticity decreased to 254 GPa at 200°C and 16 GPa for shear modulus at room temperature, decreased to 15 GPa at 200°C as shown in Fig. 4-14a,b.

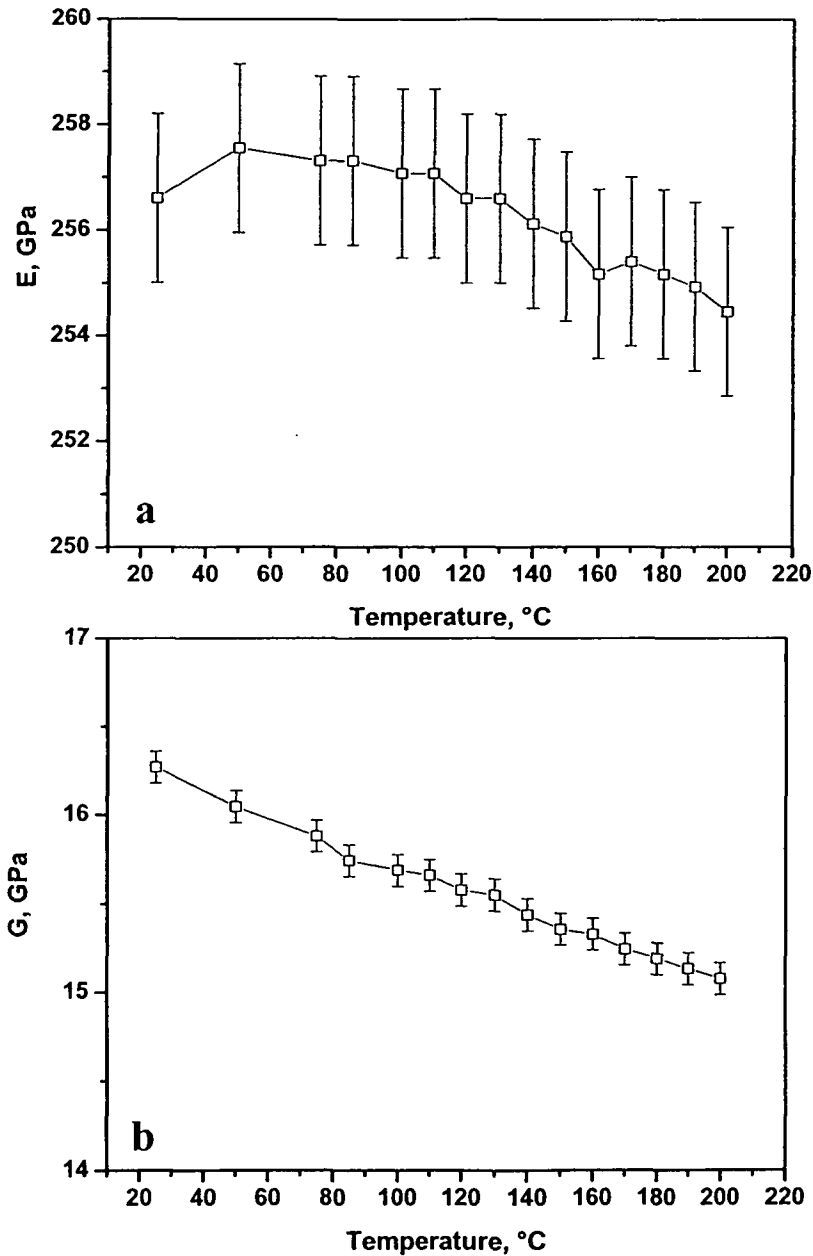


Fig.4.14, Results from the resonant beam technique for Al/C-M40B/65f in longitudinal direction. a) Young's modulus vs. temperature, b) shear modulus vs. temperature.

4.5. Resonant bar technique

4.5.1. MgAl_{0.6}/C-M40B/65f-UD MMC

The modulus of elasticity of the as received plates for Mg/C-M40/65f material is shown in table 4.6.

Table 4.6, Modulus of elasticity of as received plates for carbon fibers reinforced magnesium matrix MgAl_{0.6}/C-M40B by resonant bar technique.

Plate	Matrix	Reinforcement	E, GPa	
			Longitudinal	Transverse
V421	Mg+ 0.6 Al	Carbon M40 PAN (HM)	214	21.5
V422			212	22
V424			218	21
Average			215±3	21.5±0.5

4.5.2. AlMg1/Al₂O₃-Nextel610/65f

The modulus of elasticity of the as received plates for AlMg1/Al₂O₃ Nextel-610/65f is shown in table 4.7.

Table 4.7, Modulus of elasticity of as received plates for Nextel610 fibers reinforced aluminium matrix AlMg1/Al₂O₃-Nextel610 by resonant bar technique.

Plate	Matrix	Reinforcement	E, GPa	
			Longitudinal	Transverse
V414	Al+ 1 Mg	Al ₂ O ₃ Nextel 610	259	176
V415			255	180
V416			242	168
Average			252±8	175±6

4.6. Pulsed laser ultrasonic technique

Using pulsed laser ultrasonic technique (PLUS), overall elastic constants have been determined for MgAl_{0.6}/C-M40B and AlMg₁/Al₂O₃ Nextel610 MMCs. The results are listed in table.4.8.

Table 4.8, Engineering constants measured by PLUS technique.

	MgAl _{0.6} /C-M40B	AlMg ₁ /Al ₂ O ₃ Nextel610
E _l	216	216
E _t	18	142
ν ₁₂	0.3	0.3
ν ₂₁	0.03	0.18
G ₁₂	14.4	72

The elasticity tensor c is invariant for all rotations about the fiber-axis. The planes perpendicular to this axis are elastically isotropic. For plane waves propagating in the direction \mathbf{n} the phase velocities and polarizations are given by the eigenvalues (ρV^2) and eigenvectors of the Christoffel tensor $\Gamma_{ij} = c_{ijkl}n_j n_k$ [57]. If the fibers are in the z-direction we get e.g. with \mathbf{n} in the [100] direction:

$$\Gamma = \begin{pmatrix} c_{11} & 0 & 0 \\ 0 & c_{66} & 0 \\ 0 & 0 & c_{44} \end{pmatrix}$$

which gives one longitudinal and two transverse waves with the velocities:

$$V_L = \sqrt{\frac{c_{11}}{\rho}}, V_{T1} = \sqrt{\frac{c_{66}}{\rho}}, V_{T2} = \sqrt{\frac{c_{44}}{\rho}}$$

Therefore we can determine these three elastic constants from a measurement perpendicular to the fiber direction. To get the other elastic constants we have to vary the detection distance parallel to the fibers.

4.7. Thermal expansion

4.7.1. MgAl_{0.6}/C-M40B/65f-UD MMC

Fig.4-15(a-e) shows strain temperature curves for MgAl_{0.6}/C-M40B/65f unidirectional (UD) material with different orientations of carbon fibers within two temperature ranges, the first two cycles from -40 to 120°C followed by two cycles in the temperature range of -40 to 200°C. The given curves are averages for three specimens at each direction. The scatter between samples in the same direction differs with orientation, for the carbon fiber reinforced MMC samples, the scatter for samples in directions 0, 30, 45, 60, and 90° is from 0 to 0.005, 0.02, 0.01, 0.04, and 0.04% respectively. All samples exhibit thermal strain hysteresis between heating and cooling. Beginning from zero strain, the residual strain after first cycle up to 120°C is -0.005%, the second cycle produced very small strain of about -0.0008%. The high temperature cycle up to 200°C produced higher residual strain of about -0.007% in the first and -0.002% in the second cycle. Width of hysteresis as an indication of the degree of deformation is increasing with increasing temperature, in the first cycle the width is 0.007% while this value decreases in the second cycle at the same temperature range. For the first higher temperature cycle up to 200°C a value of 0.012 % was observed and 0.007% for the second cycle at the same temperature range. Deviation from the direction of fibers, i.e, 30, 45, 60, and 90°C leads to increased thermal expansion of UD composites with increasing the angle of inclination on the fiber direction. The residual strain decreases and hysteresis tend to have a smaller width until approximately a linear heating and cooling cycles. The temperature dependence of the instantaneous coefficient of thermal expansion of Mg/C-M40/70f material, along different orientations during heating and cooling at low temperature range (-40 to 120°C) and high temperature range (-40 to 200°C) are shown in Figs. 4-16(a-e) and 4-17(a-e) respectively. Instantaneous CTE curves were calculated from the experimental strain temperature curves according to eqn. (3.4.2).

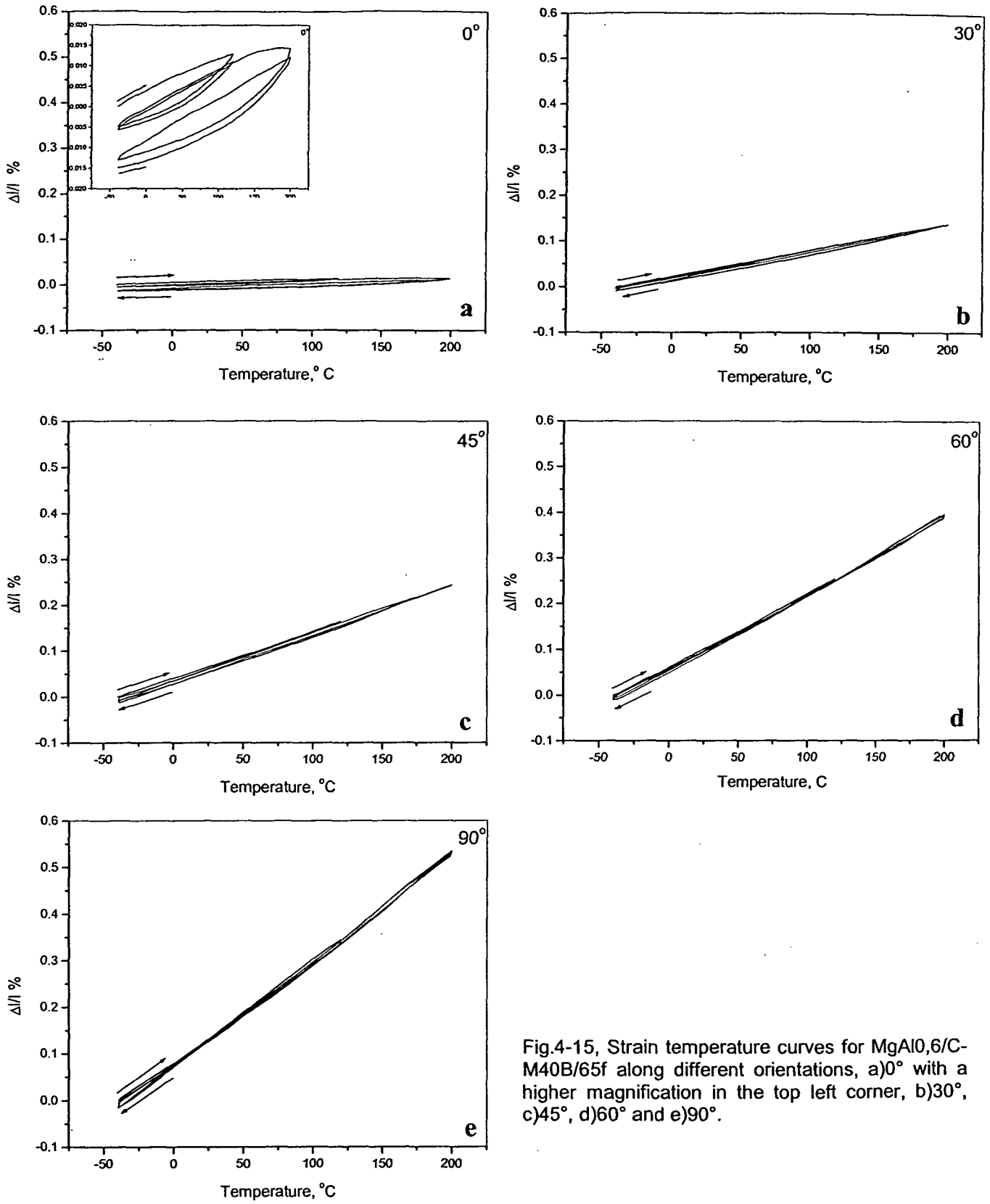


Fig.4-15, Strain temperature curves for MgAl_{0.6}/C-M40B/65f along different orientations, a)0° with a higher magnification in the top left corner, b)30°, c)45°, d)60° and e)90°.

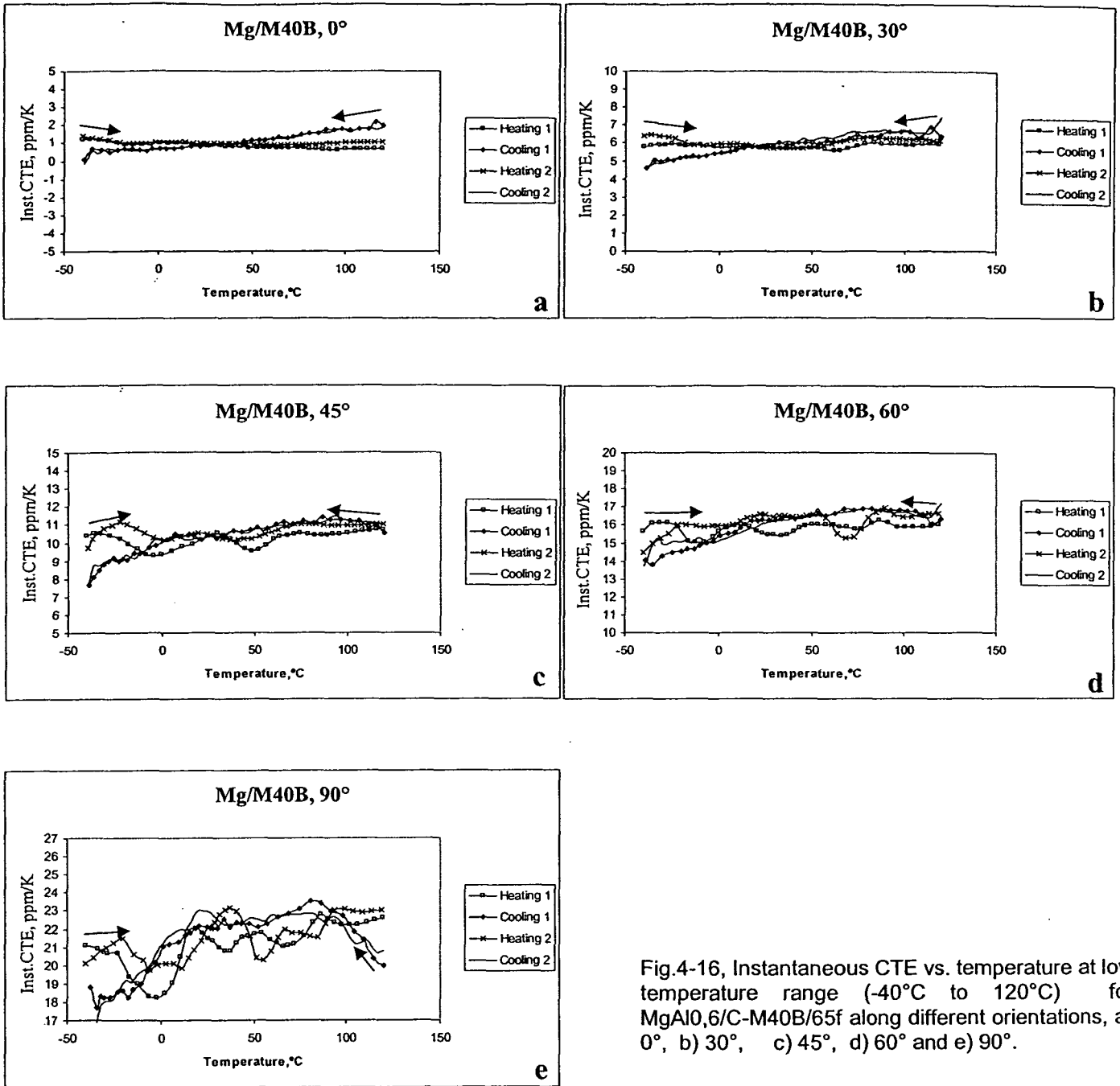


Fig.4-16, Instantaneous CTE vs. temperature at low temperature range (-40°C to 120°C) for MgAl_{0.6}C-M40B/65f along different orientations, a) 0°, b) 30°, c) 45°, d) 60° and e) 90°.

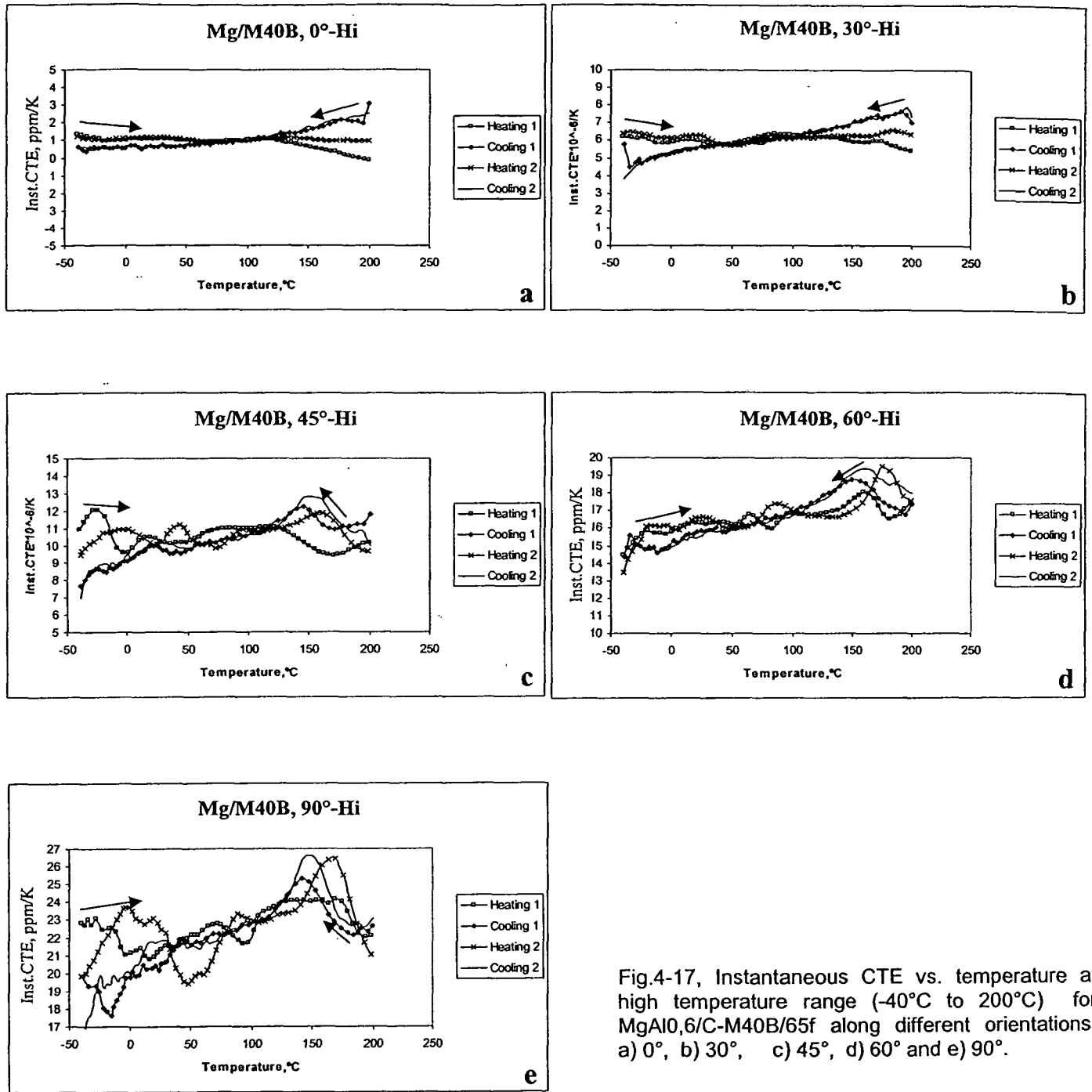


Fig.4-17, Instantaneous CTE vs. temperature at high temperature range (-40°C to 200°C) for MgAl_{0.6}C-M40B/65f along different orientations, a) 0°, b) 30°, c) 45°, d) 60° and e) 90°.

4.7.2. AlMg0.6/Al₂O₃-Nextel610/65f

With the same four temperature cycles, two low temperature cycles (-40 to 120°C) followed by two high temperature cycles (-40 to 200°C) have been done as shown in Fig.4.18. For the Nextel fiber reinforced MMC samples, the scatter for samples in directions 0°, 30°, 45°, 60°, and 90° is from 0 to 0.01, 0.01, 0.03, 0.02, and 0.02% respectively. For the longitudinal specimens, after the first cycle the width of hysteresis was 0.002% and after the first high temperature cycle the width of hysteresis was 0.015%. The residual strain after first cycle up to 120°C is -0.0042%, the second cycle produced strain of about -0.0014%. The high temperature cycle up to 200°C produced residual strain of about -0.007% recycling at the same temperature produced residual strain of -0.0008%. The total strain in the inspected temperature range was the highest among the three different UD systems because of the high CTE value of the Nextel alumina fibers ($8 \times 10^{-6} / K$) compared to zero CTE value for C-fibers. Negligible contraction in the specimens with directions 30 and 45° on the direction of fibers has been observed, while the strain vs. temperature is approximately linear, on the other hand an expansion in final length in the orientations of 60° and transverse directions was observed.

Calculated Instantaneous CTE curves are shown in Figs.19 and 20(a-e) for both temperature ranges (-40 to 120°C and -40 to 200°C) respectively, an increase in CTE values with increasing temperature during heating was observed almost in all orientations accompanied by a decrease in CTE during cooling.

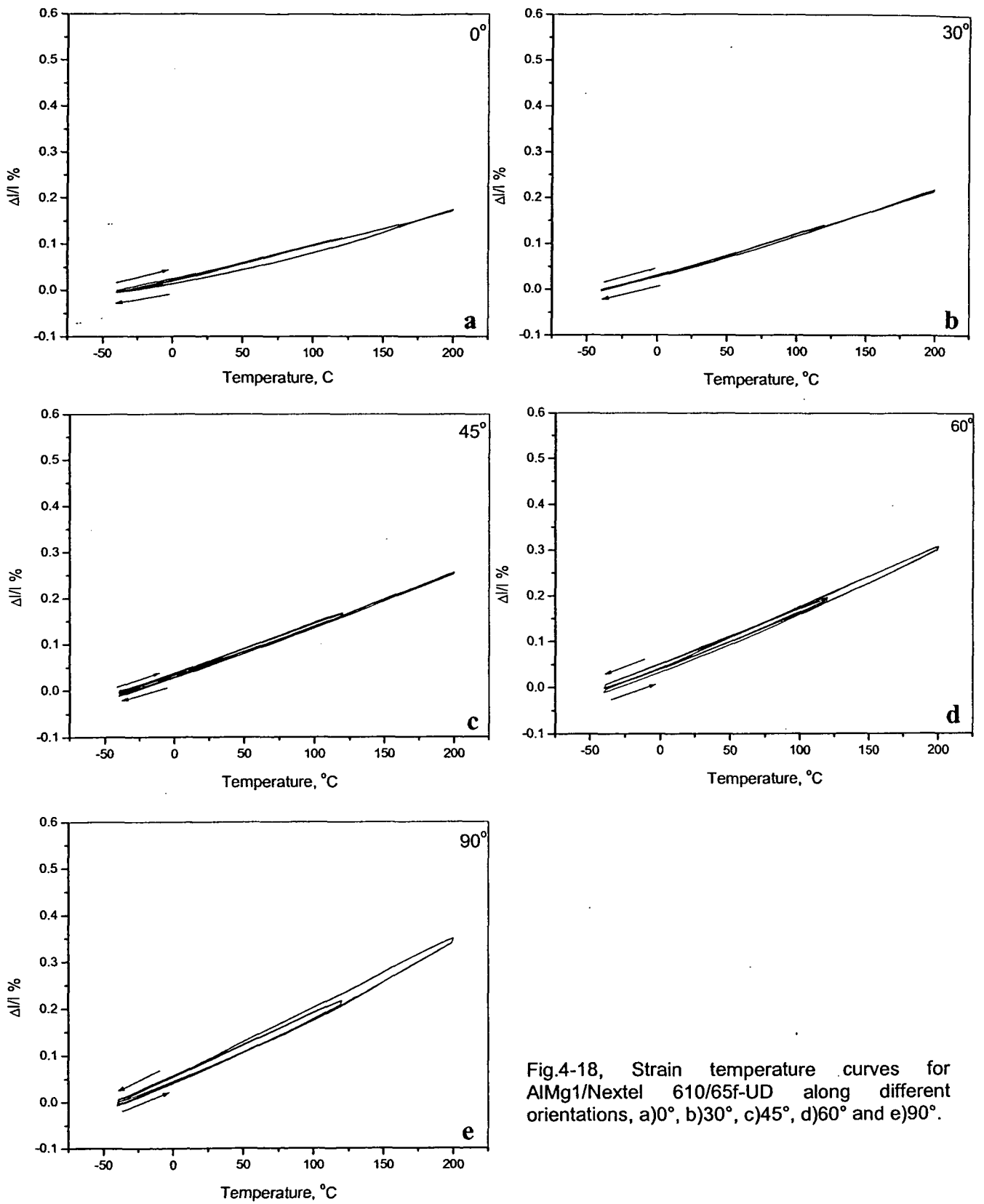


Fig.4-18, Strain temperature curves for AlMg1/Nextel 610/65f-UD along different orientations, a) 0° , b) 30° , c) 45° , d) 60° and e) 90° .

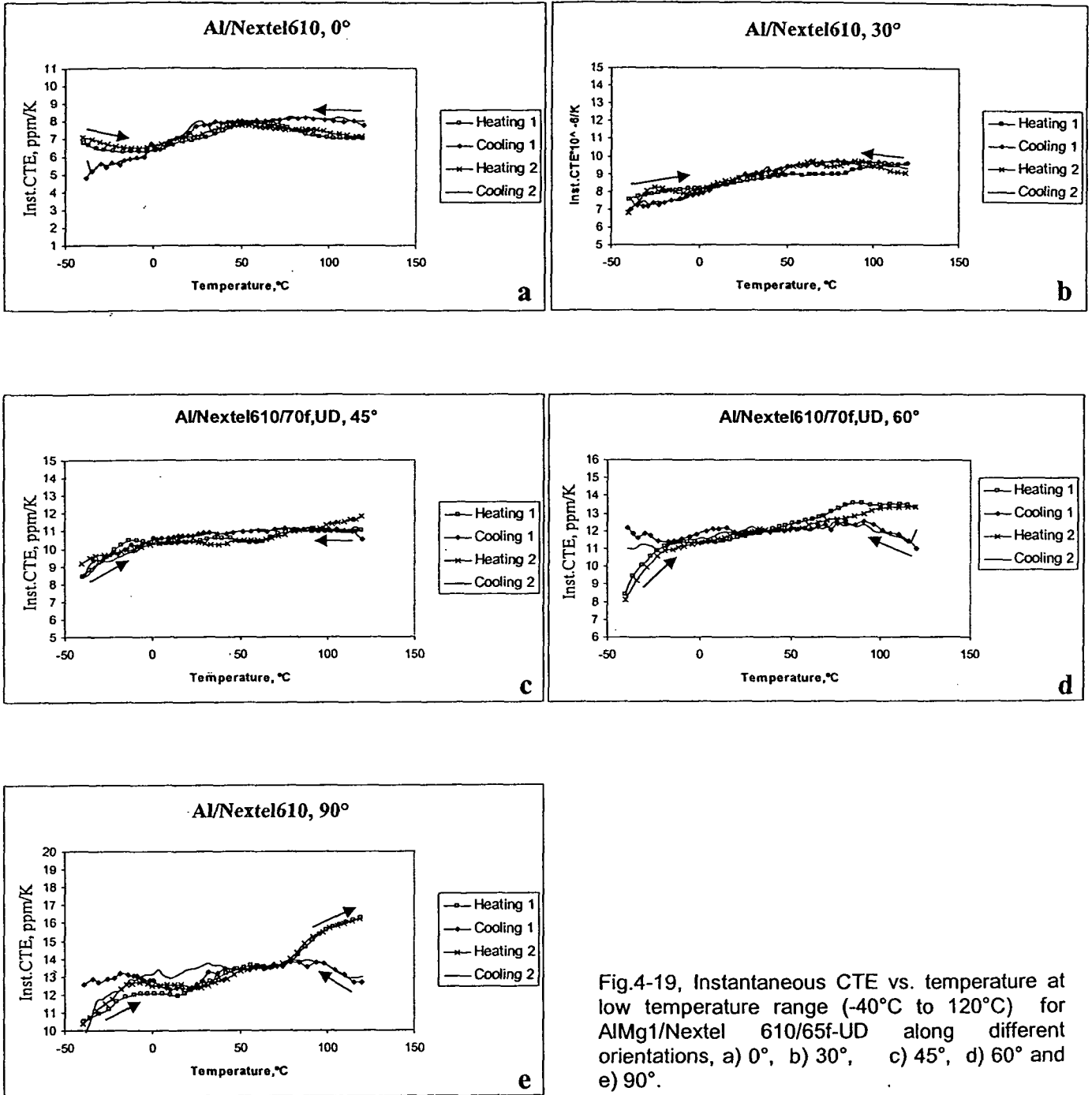


Fig.4-19, Instantaneous CTE vs. temperature at low temperature range (-40°C to 120°C) for AlMg1/Nextel 610/65f-UD along different orientations, a) 0°, b) 30°, c) 45°, d) 60° and e) 90°.

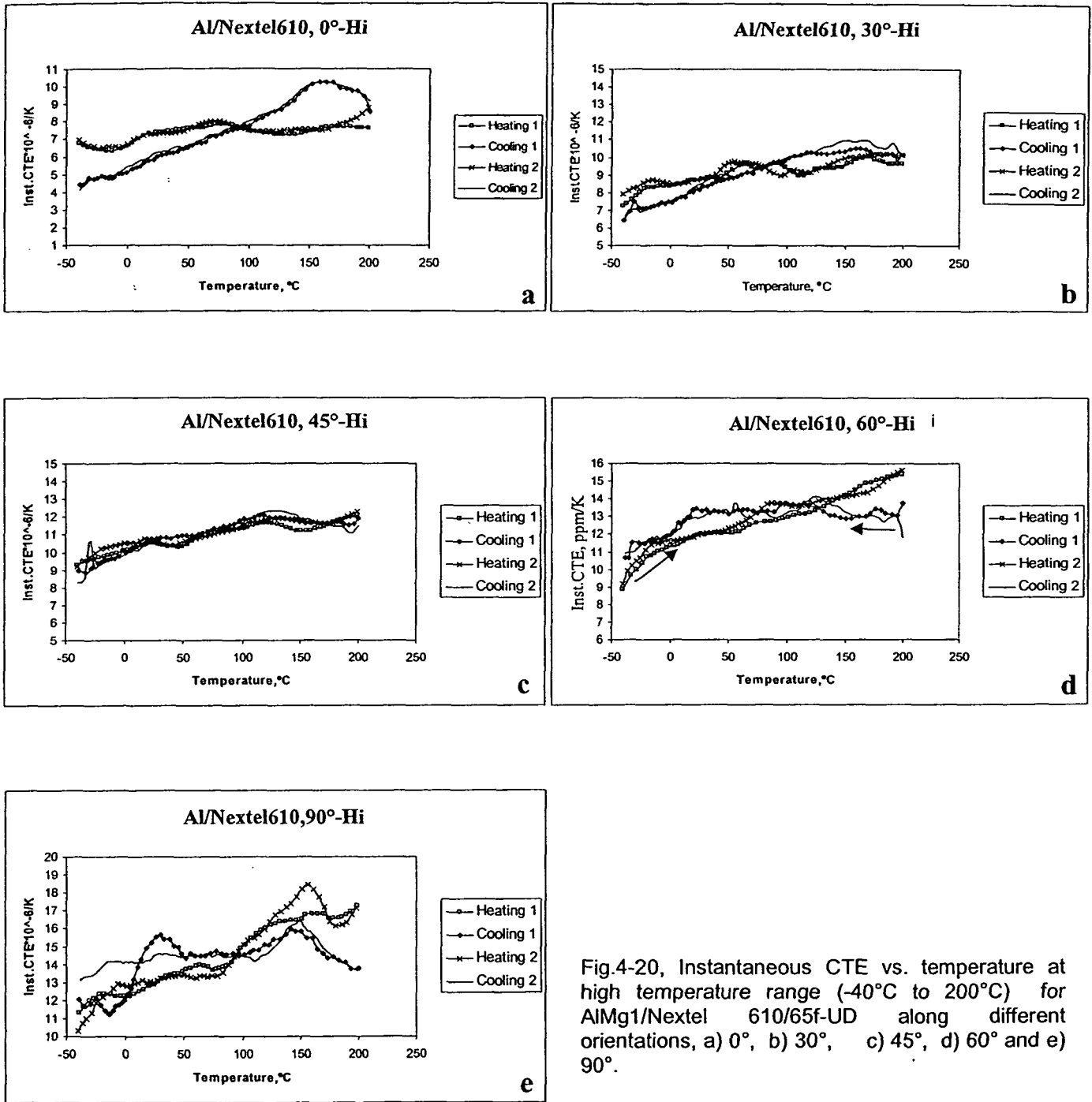


Fig.4-20, Instantaneous CTE vs. temperature at high temperature range (-40°C to 200°C) for AlMg1/Nextel 610/65f-UD along different orientations, a) 0°, b) 30°, c) 45°, d) 60° and e) 90°.

4.7.3. Al/C-M40B/65f

The same experimental procedures for the previous systems were applied to the Al/C-M40/74f material. A hysteresis is also observed for all the strain temperature curves and for orientations on the main fiber axis as shown in Fig.4-21 (a-e). The residual strain for Mg is higher than that for Al matrix composites in the direction of fibers.

Fig.4-21(a-e) shows strain temperature curves for Al/C-M40B/74f unidirectional (UD) material with different orientations of carbon fibers within two temperature ranges, the first two cycles from -40 to 120°C followed by two cycles in the temperature range of -40 to 200°C. The given curves are average for three specimens at each direction. All samples exhibit thermal strain hysteresis between heating and cooling. Careful examination of the longitudinal direction, Fig.4-20a, reveals that the specimens suffer a very slight shrinkage after the first cycle up to 120°C with a strain of -0.002% and again after the first cycle to 200°C with the same strain value of -0.002%, that is because of the residual thermal stresses generated during thermal cycling. Negligible strain values for the repeated cycles at the same temperature range are produced. The hysteresis of the heating and cooling stage opens up slightly when the temperature is increased to 200°C indicating additional plastification of the matrix. The width of the hysteresis indicating deformation is relatively high, 0.014 and 0.013% in the first and second cycles, respectively, in the low temperature range up to 120°C and 0.02 and 0.019% in the third and fourth high temperature cycles, respectively up to 200°C. The total strain is increasing with increasing orientation angle on the main fiber axis.

The temperature dependence of the instantaneous coefficient of thermal expansion of Al/C-M40B/74f material, along different orientations during heating and cooling at low temperature range (-40 to 120°C) and high temperature range (-40 to 200°C) are shown in Figs. 4-22(a-e) and 4-23(a-e) respectively. Instantaneous CTE curves were calculated from the experimental strain temperature curves according to eqn. (3.4.2).

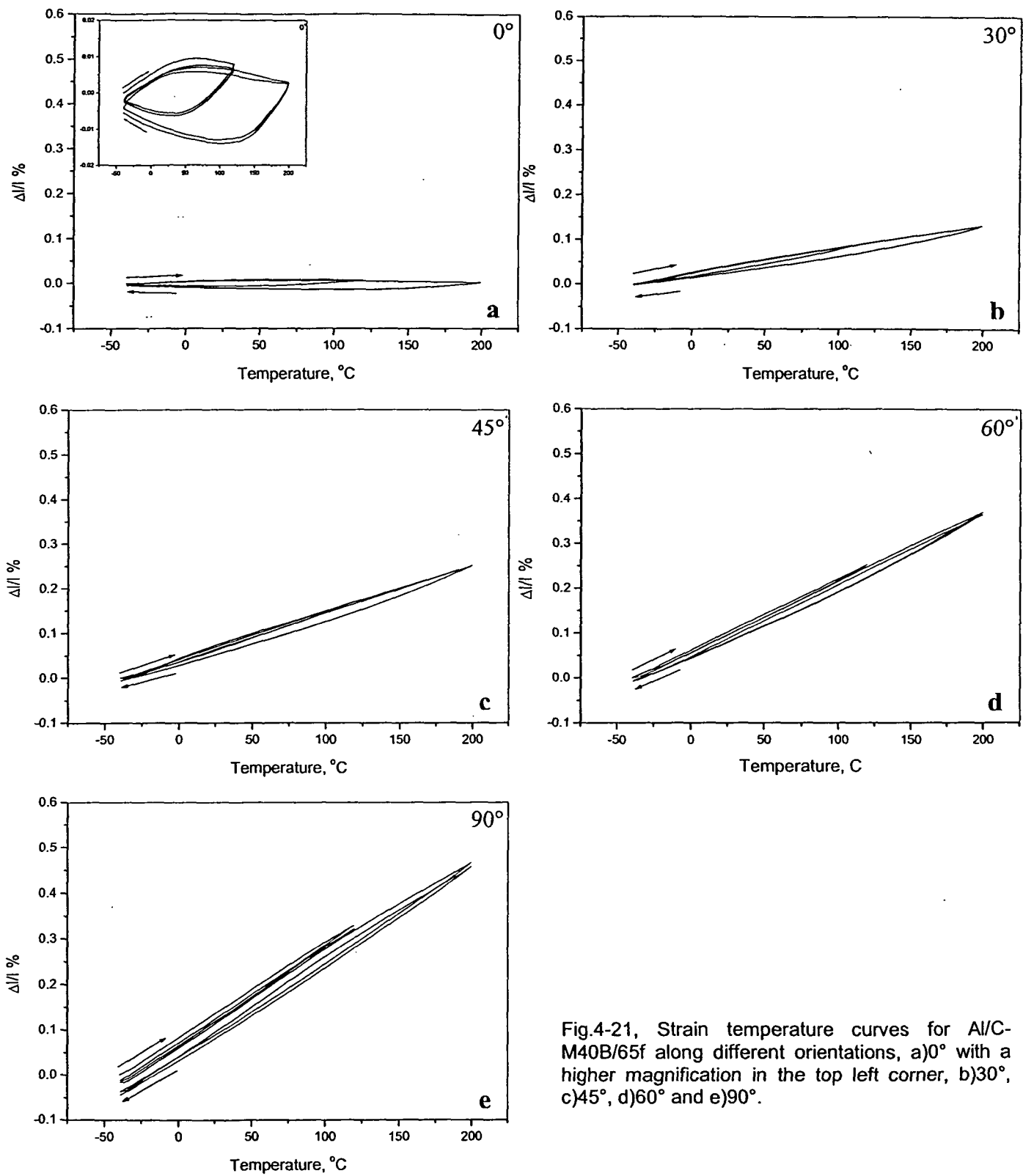


Fig.4-21, Strain temperature curves for Al/C-M40B/65f along different orientations, a)0° with a higher magnification in the top left corner, b)30°, c)45°, d)60° and e)90°.

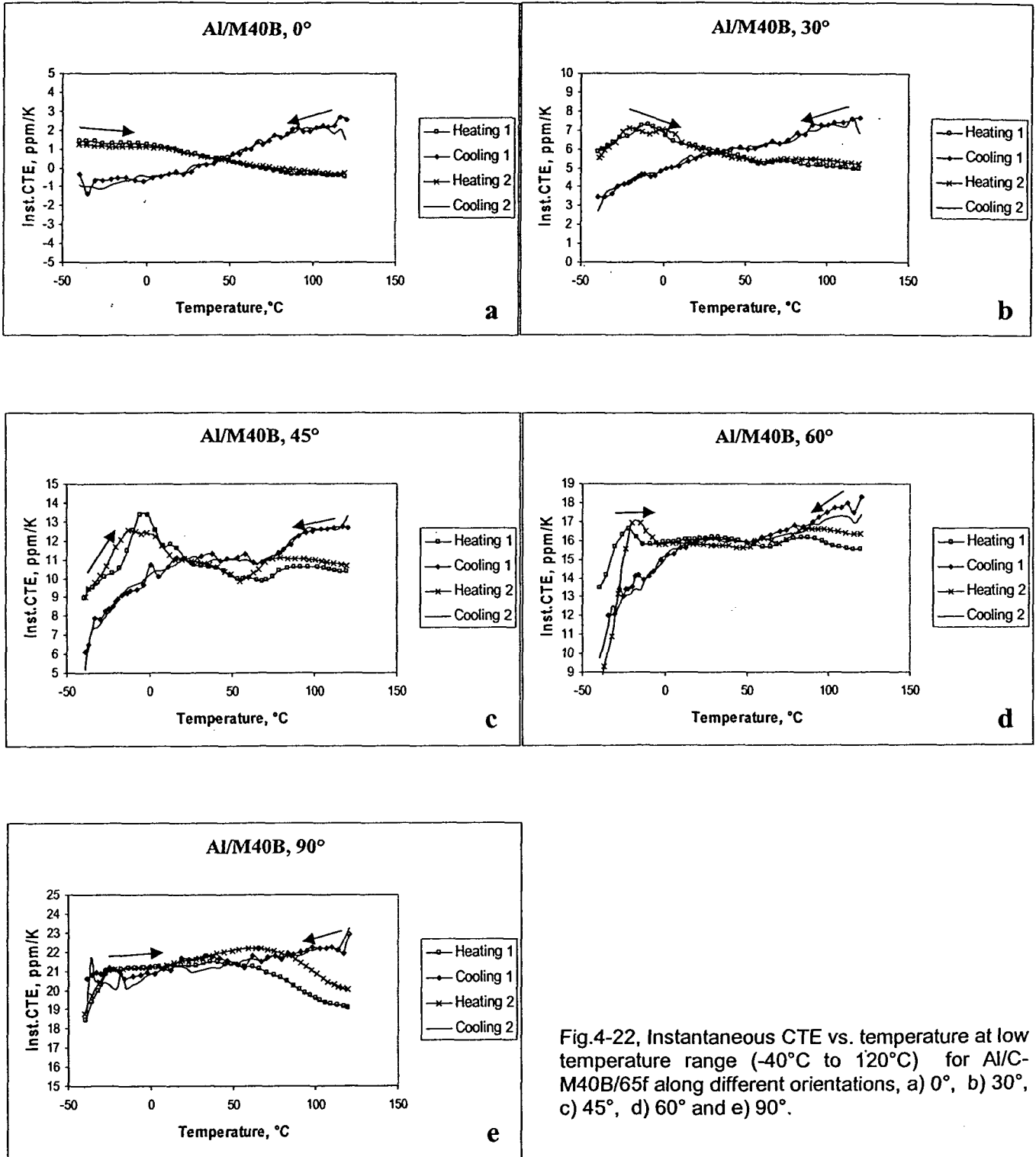


Fig.4-22, Instantaneous CTE vs. temperature at low temperature range (-40°C to 120°C) for Al/C-M40B/65f along different orientations, a) 0°, b) 30°, c) 45°, d) 60° and e) 90°.

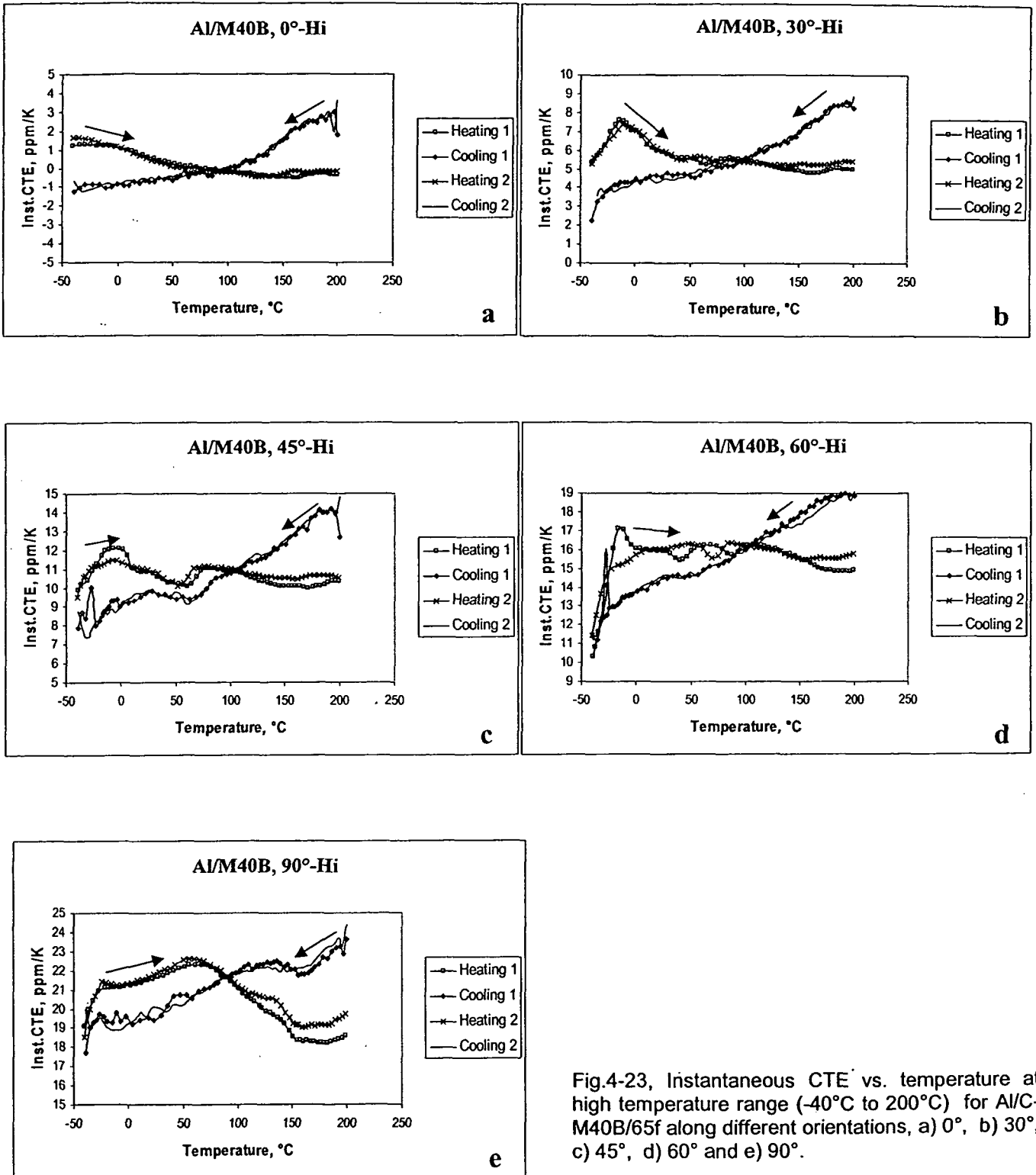


Fig.4-23, Instantaneous CTE vs. temperature at high temperature range (-40°C to 200°C) for Al/C-M40B/65f along different orientations, a) 0°, b) 30°, c) 45°, d) 60° and e) 90°.

4.7.4. Mg/C-Tenax HTA 5331/55f-UD

The same procedure was used for the low modulus tenax carbon fibers reinforced magnesium with 60% fibers volume fraction as shown in Fig.4.24. For the longitudinal direction samples, the behavior of strain against temperature was linear up to temperature of 8°C with a strain of 0.017%, the slope of the line then decreases reaching the maximum strain of 0.04% at the end of the first cycle at 120°C. The maximum width of the hysteresis is 0.09%. For the second low temperature range cycle, no change was observed except width decrease in the hysteresis to 0.07%. In the higher temperature range, three different slopes were observed. Sharp decrease of the slope at the third stage at temperature of 140°C with strain of 0.045% was observed. No residual strain was observed in the low temperature cycle, while a relatively large residual strain of -0.015% linked with a large width of the hysteresis of 0.023%. The width of hysteresis then reduced to 0.013% in the second High temperature cycle with a negligible residual strain at the end of the temperature cycling at -40°C. For the 30° orientation specimen almost linear behavior was observed for the low temperature cycle while a slight change in slope can be recognized at 177°C, with a total strain of 0.16% at the end of the cycle. With increasing angle of inclination, the hysteresis becomes narrower and goes counter clockwise for 60° and 90° specimens. The temperature dependence of the instantaneous coefficient of thermal expansion along different orientations during heating and cooling at low temperature range (-40 to 120°C) and high temperature range (-40 to 200, 300 and 400°C) are shown in Figs. 4-25(a-e) and 4-26(a-g), respectively. For the longitudinal direction samples, the CTE remains constant up to 8°C then decreased with increasing temperature up to 60°C and then levels off until the end of the first cycle. In the high temperature cycle, the same behavior like previous attached with drop in CTE begins at 120°C up to the end of the cycle. With increasing angle of inclination of the specimen on the fiber axis, The CTE values increased up to the maximum value at the transverse direction which is close to the matrix CTE value.

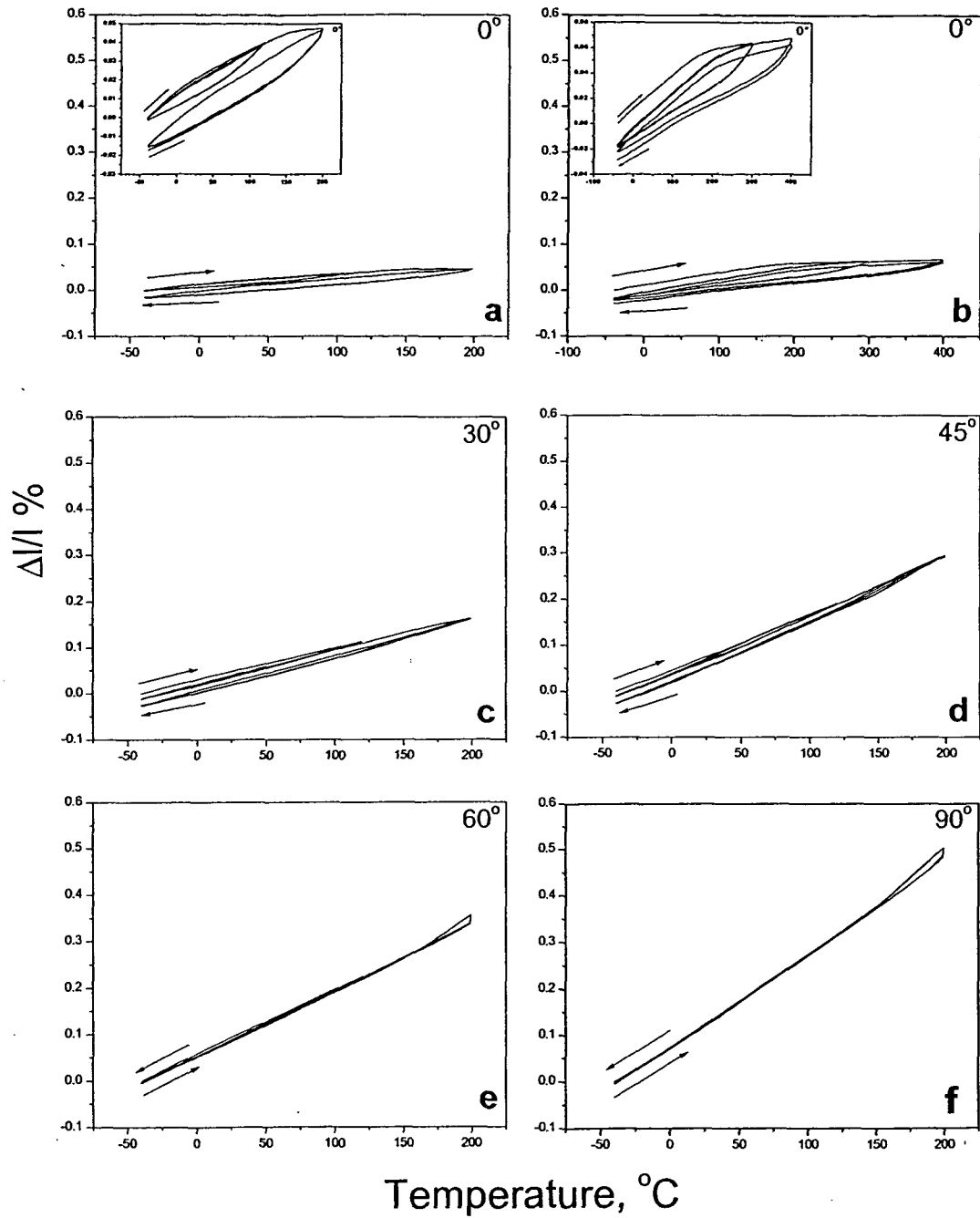


Fig.4-24, Strain temperature curves for Mg/C-Tenax HTA 5331/55f along different orientations, a)0° at temperature ranges from -40 to 120°C and 200°C, b) 0° at temperature ranges from -40 to 300°C and 400°C, c) 30°, d)45°, e)60° and f)90°.

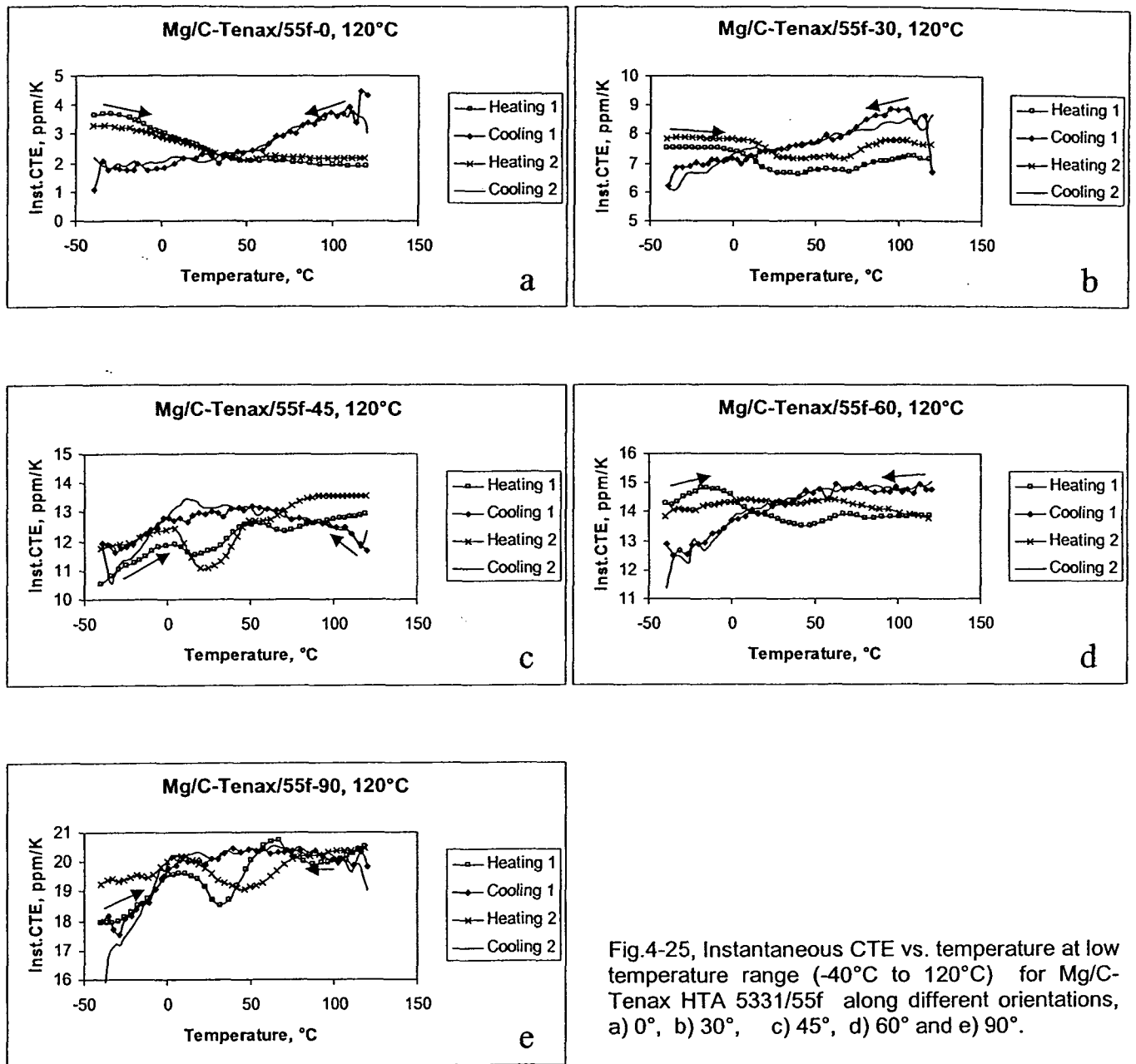


Fig.4-25, Instantaneous CTE vs. temperature at low temperature range (-40°C to 120°C) for Mg/C-Tenax HTA 5331/55f along different orientations, a) 0°, b) 30°, c) 45°, d) 60° and e) 90°.

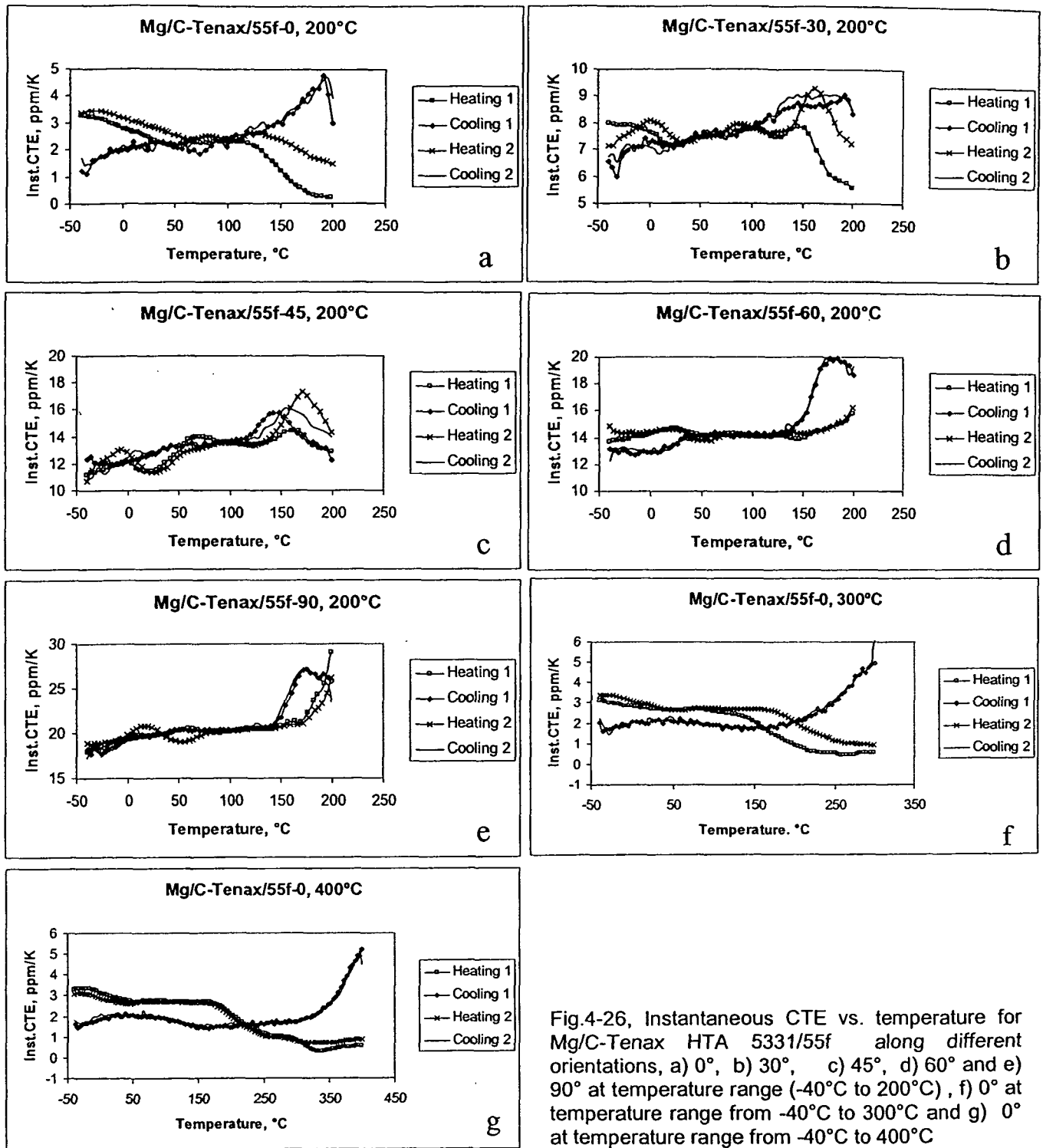


Fig.4-26, Instantaneous CTE vs. temperature for Mg/C-Tenax HTA 5331/55f along different orientations, a) 0°, b) 30°, c) 45°, d) 60° and e) 90° at temperature range (-40°C to 200°C) , f) 0° at temperature range from -40°C to 300°C and g) 0° at temperature range from -40°C to 400°C

4.7.5. Al/C-M40B/64f, (0°, +60°, -60°, -60°, +60°, 0°)

Dilatation curves for different fiber orientations are shown in Fig. 4-27(a-e) in the same temperature cycles as previous systems. The general nature of the dimension change versus temperature is similar for all the fiber composite systems, marked hysteresis, which run in the clockwise direction, are evident for all orientations. In the direction of fibers, upon heating beginning from zero strain value and -40°C, a linear increase in strain up to 0°C with a strain of 0.01%, followed by decreasing rate of strain up to 75°C with a strain value of 0.018%. The strain levels off giving a plateau until the end of the first cycle at 120°C with a total strain of 0.019%. Upon cooling, a linear strain decrease until temperature of 90°C with strain of -0.006% followed by decreasing strain rate to a temperature of 63°C and strain of -0.001%, then a constant strain to a temperature of -5°C followed by increasing strain to a value of -0.001% up to the end of the temperature cycle at -40°C. A total shrinkage in the specimens between heating and cooling cycles was observed in all inclinations to fiber directions. Approximately, no difference in the second cycle in the same temperature range was observed. At higher temperature range up to 200°C, the same behavior except a little higher total strain of 0.021% in the end of the heating cycle at 200°C. As these specimens have two layers in the axial direction of measurements, the total strain is minimum compared with the specimens in different directions. At the selected angles of inclination to the axial plate direction, i.e.; 15, 30, 45, and 90°, the same behavior in general was observed. With respect to 0°C samples a higher total strain value, the disappearance of the plateau, and a continuous decrease in strain rate until the end of the cooling cycles can be observed resulting in a specimen contraction.

The instantaneous coefficient of thermal expansion for both low temperature cycles and high temperature cycles at different specimen directions were computed from the experimental strain versus temperature curves and illustrated in Figs.28(a-e),29(a-e). Upon heating the CTE value decreased with increasing temperature as observed for all fibres reinforced MMCs, this decrease followed by a plateau in case of high temperature range up to 200°C, with temperature

conversion from heating to cooling the CTE jumps up and decreased with cooling, reaching minimum at temperature of -40°C .

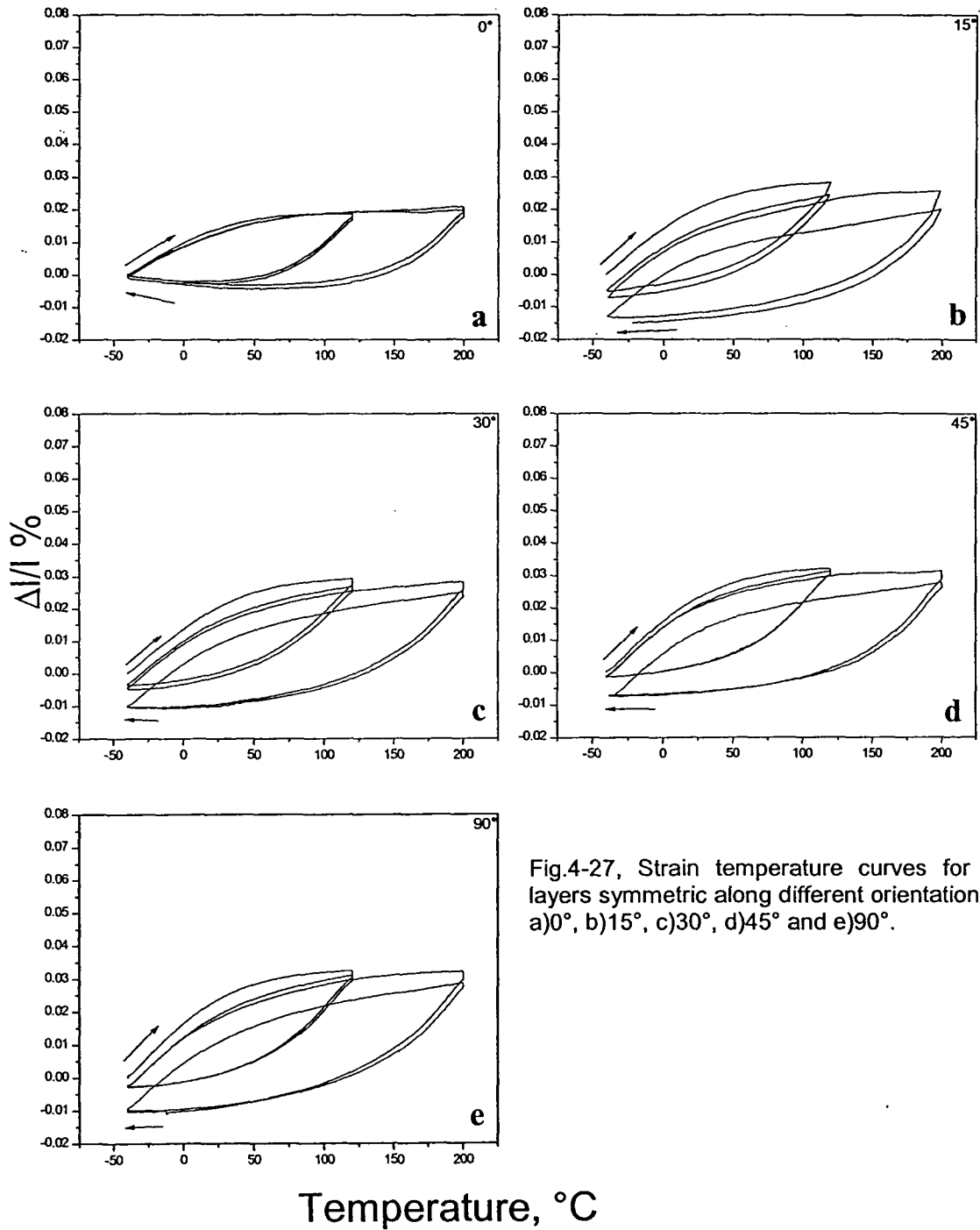


Fig.4-27, Strain temperature curves for 6 layers symmetric along different orientations, a) 0° , b) 15° , c) 30° , d) 45° and e) 90° .

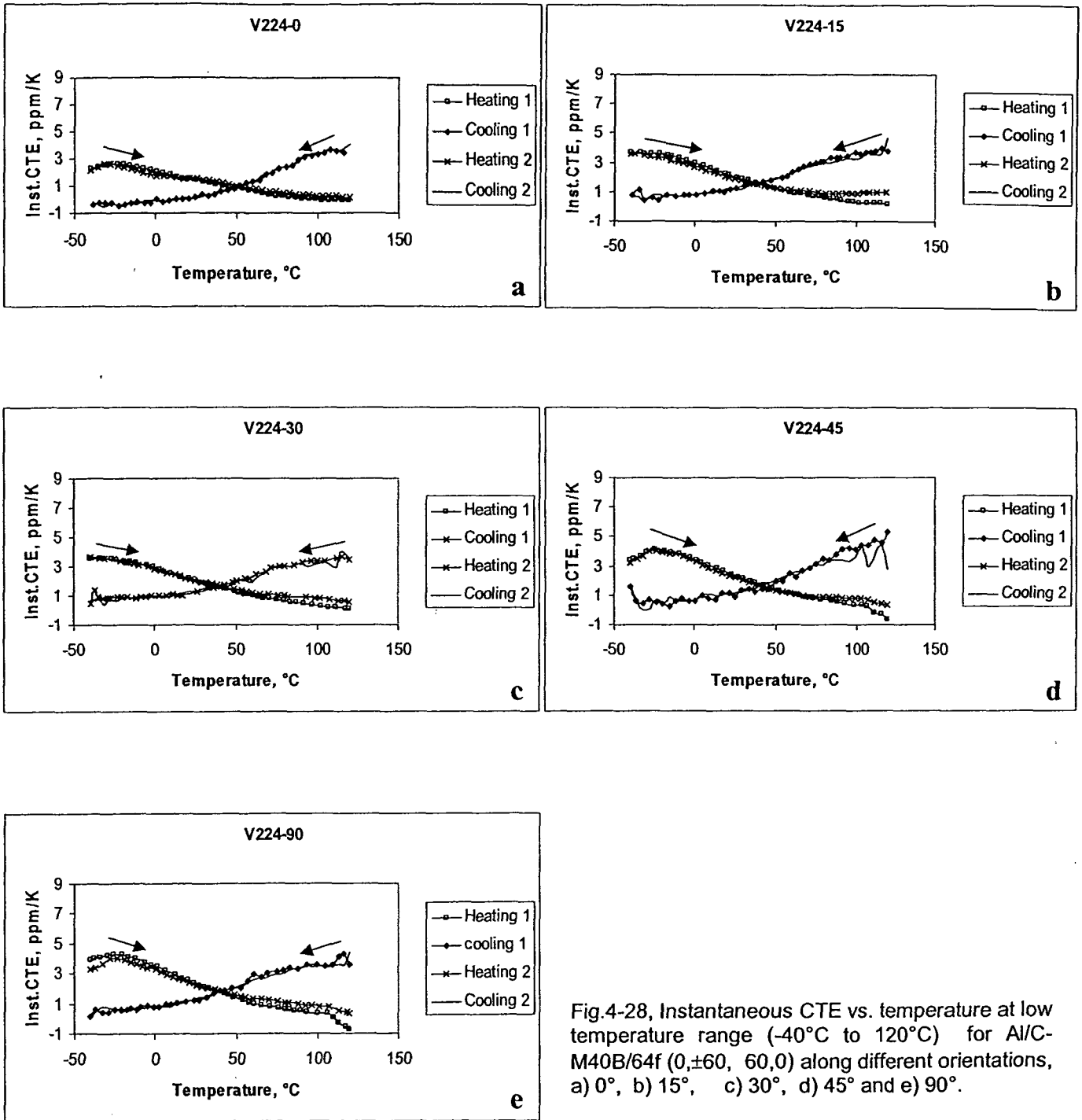


Fig.4-28, Instantaneous CTE vs. temperature at low temperature range (-40°C to 120°C) for Al/C-M40B/64f (0,±60, 60,0) along different orientations, a) 0°, b) 15°, c) 30°, d) 45° and e) 90°.

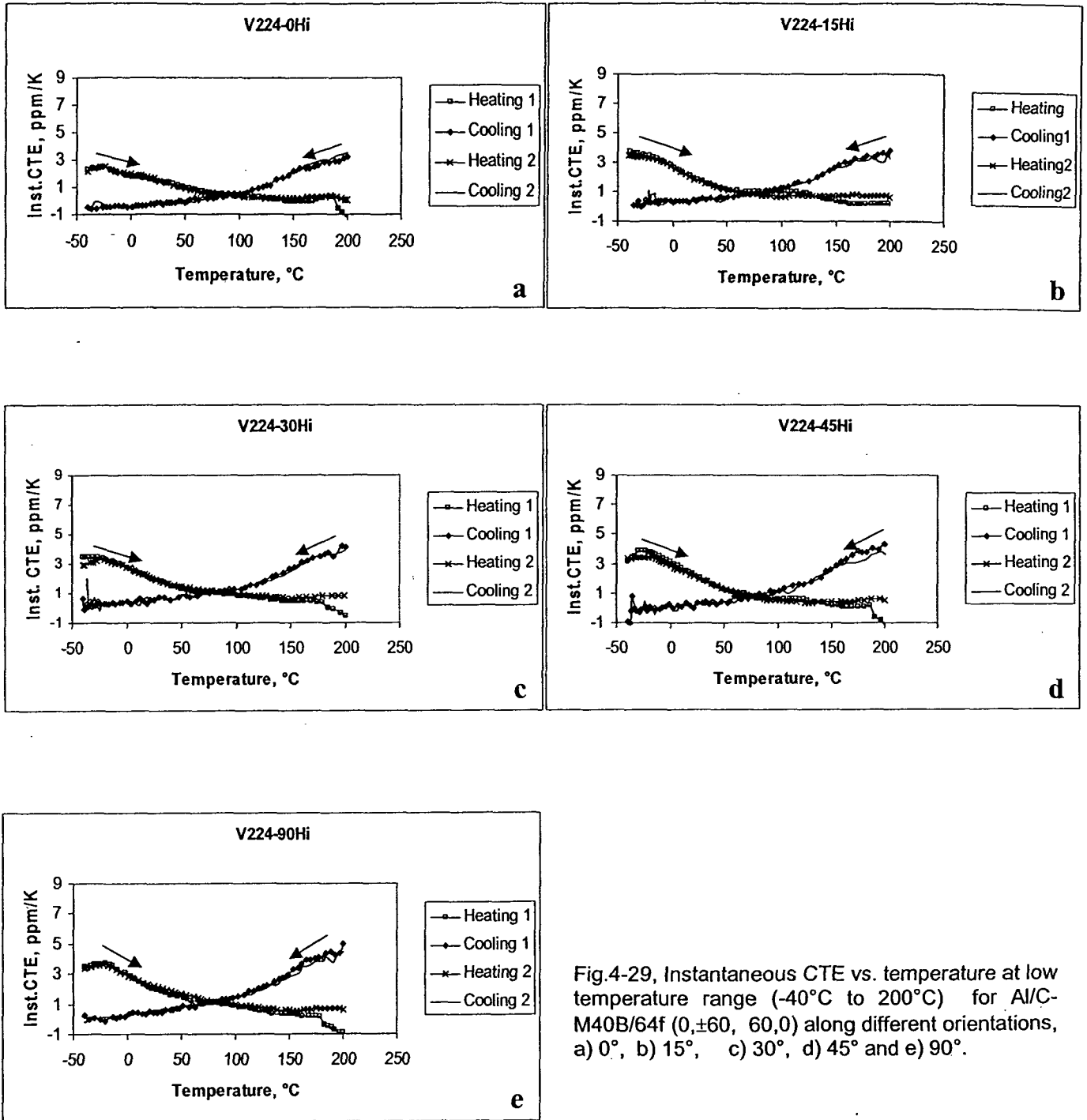


Fig.4-29, Instantaneous CTE vs. temperature at low temperature range (-40°C to 200°C) for Al/C-M40B/64f (0,±60, 60,0) along different orientations, a) 0°, b) 15°, c) 30°, d) 45° and e) 90°.

4.7.6. Woven MgAl/C-T300J/50f

Fig. 4-30(a-e) shows the dilatation curves for woven carbon fibers reinforced magnesium with 50% of fibers in the warp and 50% in the fill directions in different directions during thermal cycling. The hysteresis of the heating and cooling stage opens up when the temperature is increased to 200°C indicating plastification of the matrix. For the 0° orientation specimens, a linear change was observed from the beginning of the measurements; zero strain at -40°C, up to 0.05% strain at 37°C, followed by a curved behavior with decreasing rate until a total strain of 0.1% in the end of first cycle. In the higher temperature cycle up to 200°C, the same behavior was observed with a higher total strain of 0.12%. The specimens from the plane of fiber orientation suffer a slight shrinkage after the first cycle up to 120°C and again after the first cycle to 200°C. This is due to changes in the internal stresses by the heat treatment during the dilatometer test. Highest total strain values were observed in the 45° specimens, 30° and 60° are equivalent with respect to the 0/90° fiber orientation. Specimens out of plane had slight expansion upon cycling.

The change in the instantaneous thermal expansion coefficient during heating and cooling is shown in Fig.4-31(a-e) and Fig.4-32(a-e) for the 120°C and 200°C upper temperature cycles respectively. Slight increase in the CTE values in the second heating cycle in the low temperature range measurements as well as drop in the CTE above 120°C in the high temperature range measurements. The temperature dependence in the fiber plane is reasonable isotropic have been observed.

With increasing carbon fiber percent in the warp to 80% of the fibers, specimens in the 0° direction exhibit a smaller thermal strain about 0.055% (about 25% less than the 50:50 sample), and 90° direction largest strain about 0.15% (more than half of the 50:50 sample), as shown in Fig. 4-33(a-e). The instantaneous CTE vs. temperature for both temperature ranges are shown in Fig. 4-34(a-e) and 4-35 (a-e).

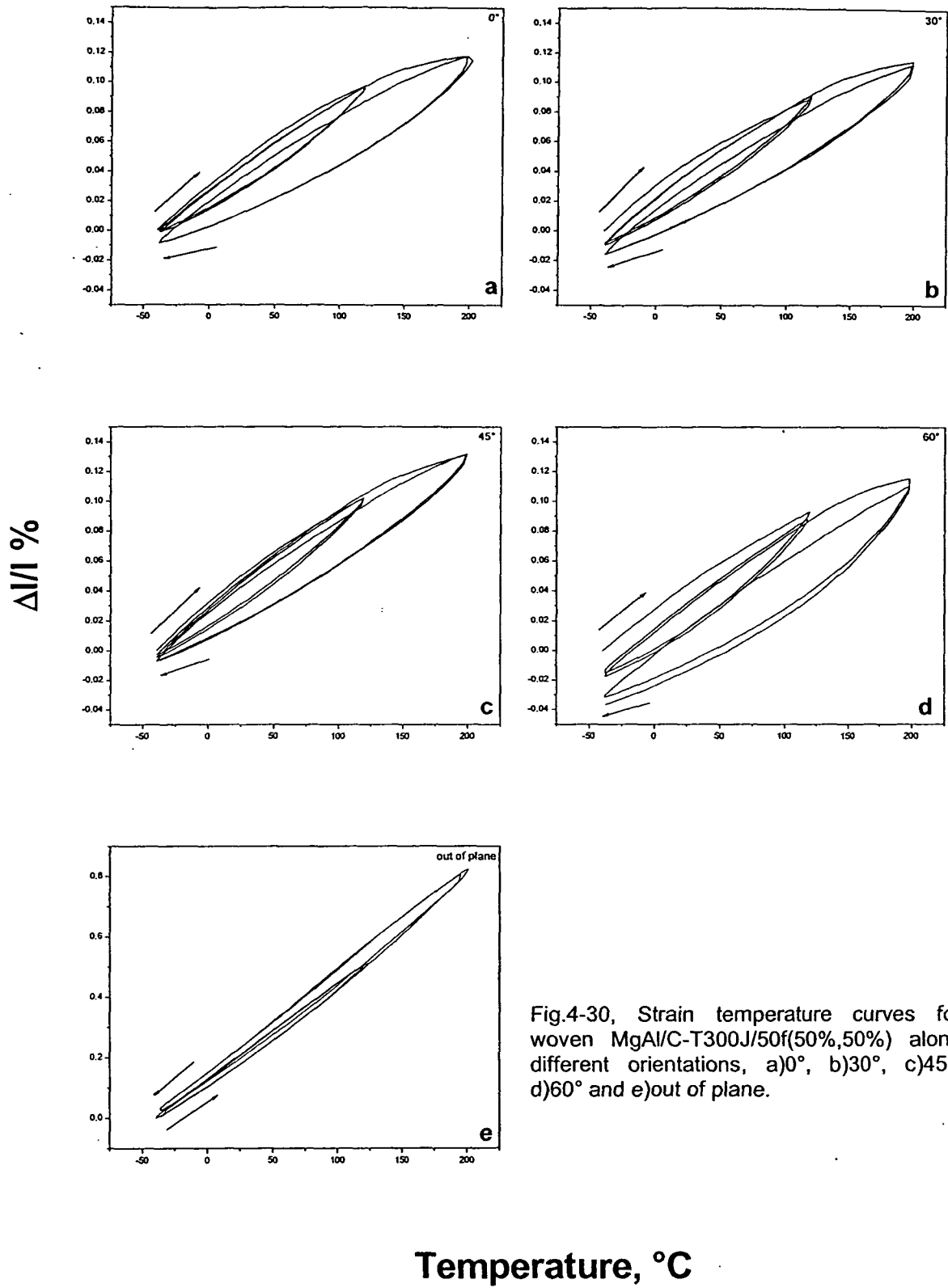


Fig.4-30, Strain temperature curves for woven MgAl/C-T300J/50f(50%,50%) along different orientations, a)0°, b)30°, c)45°, d)60° and e)out of plane.

Temperature, $^{\circ}\text{C}$

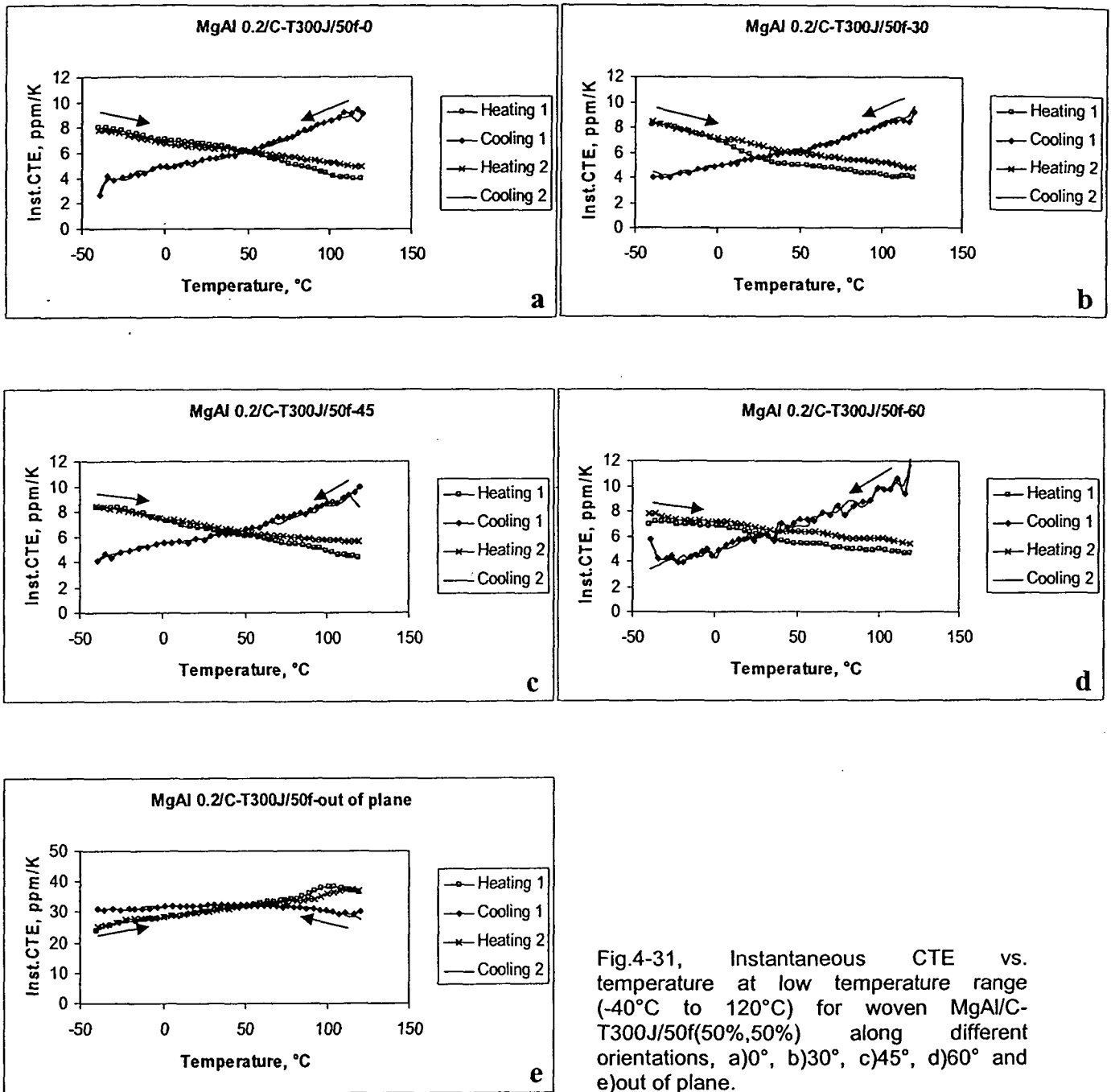


Fig.4-31, Instantaneous CTE vs. temperature at low temperature range (-40°C to 120°C) for woven MgAl/C-T300J/50f(50%,50%) along different orientations, a)0°, b)30°, c)45°, d)60° and e)out of plane.

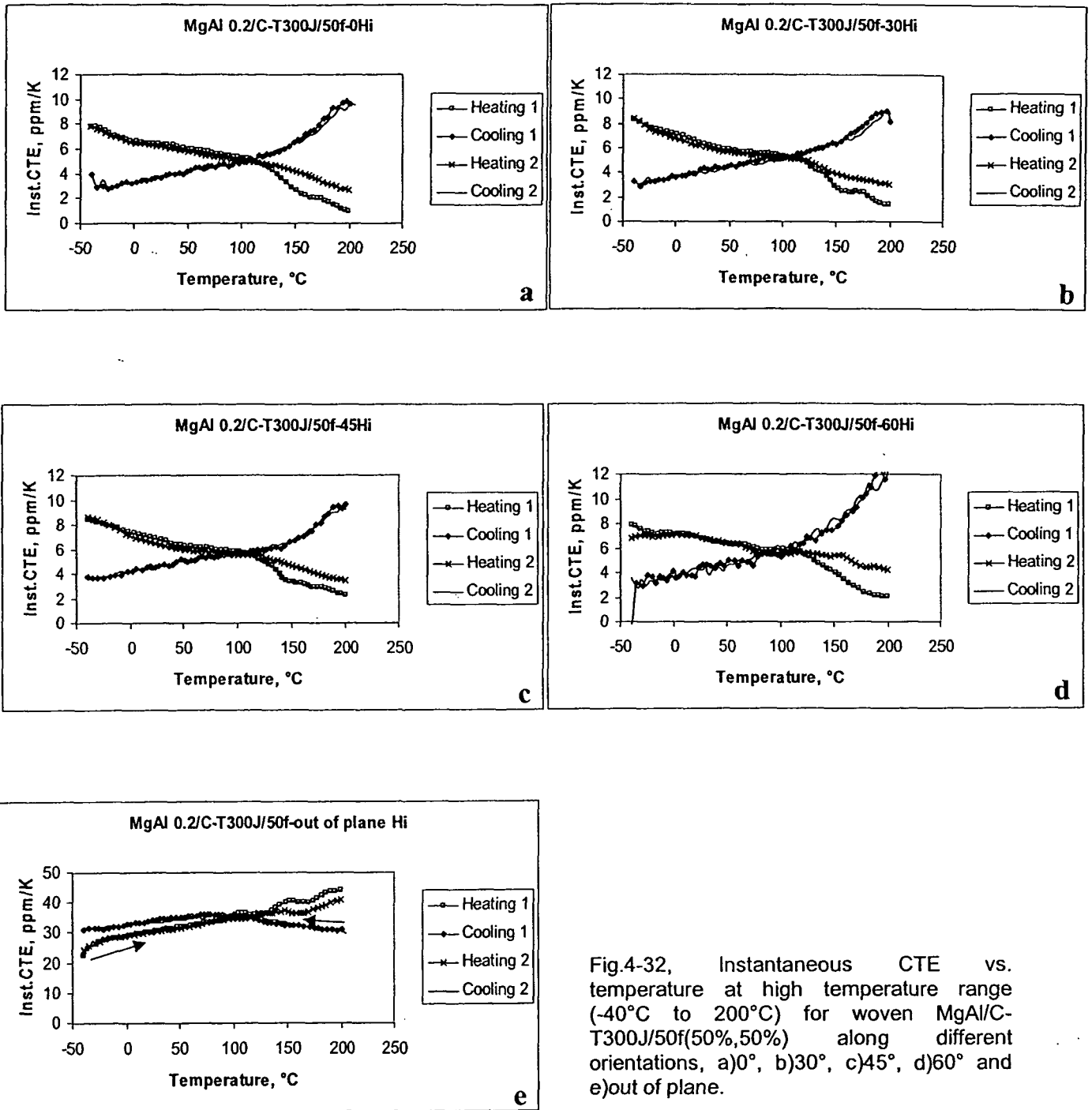


Fig.4-32, Instantaneous CTE vs. temperature at high temperature range (-40°C to 200°C) for woven MgAl/C-T300J/50f(50%,50%) along different orientations, a)0°, b)30°, c)45°, d)60° and e)out of plane.

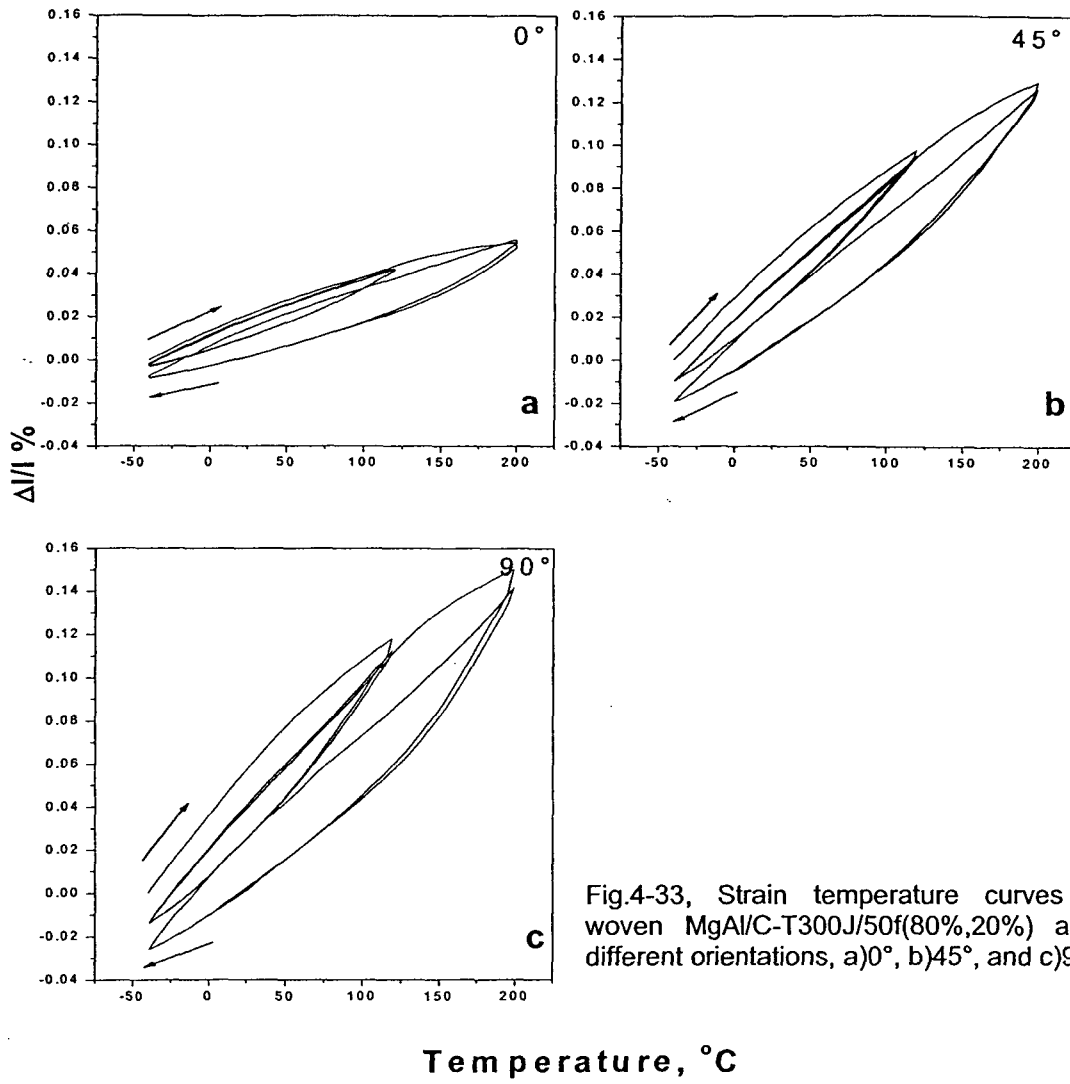


Fig.4-33, Strain temperature curves for woven MgAl/C-T300J/50f(80%,20%) along different orientations, a)0°, b)45°, and c)90°.

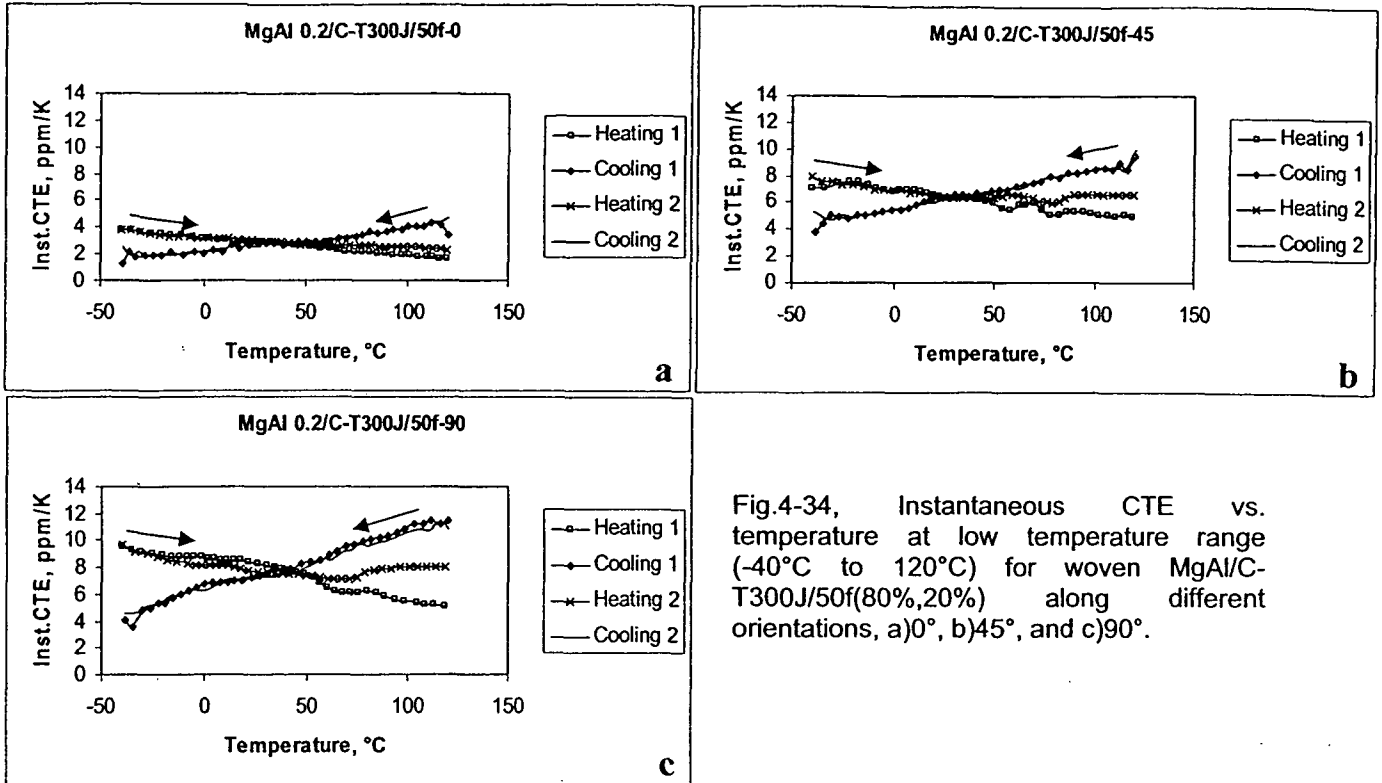


Fig.4-34, Instantaneous CTE vs. temperature at low temperature range (-40°C to 120°C) for woven MgAl/C-T300J/50f(80%,20%) along different orientations, a)0°, b)45°, and c)90°.

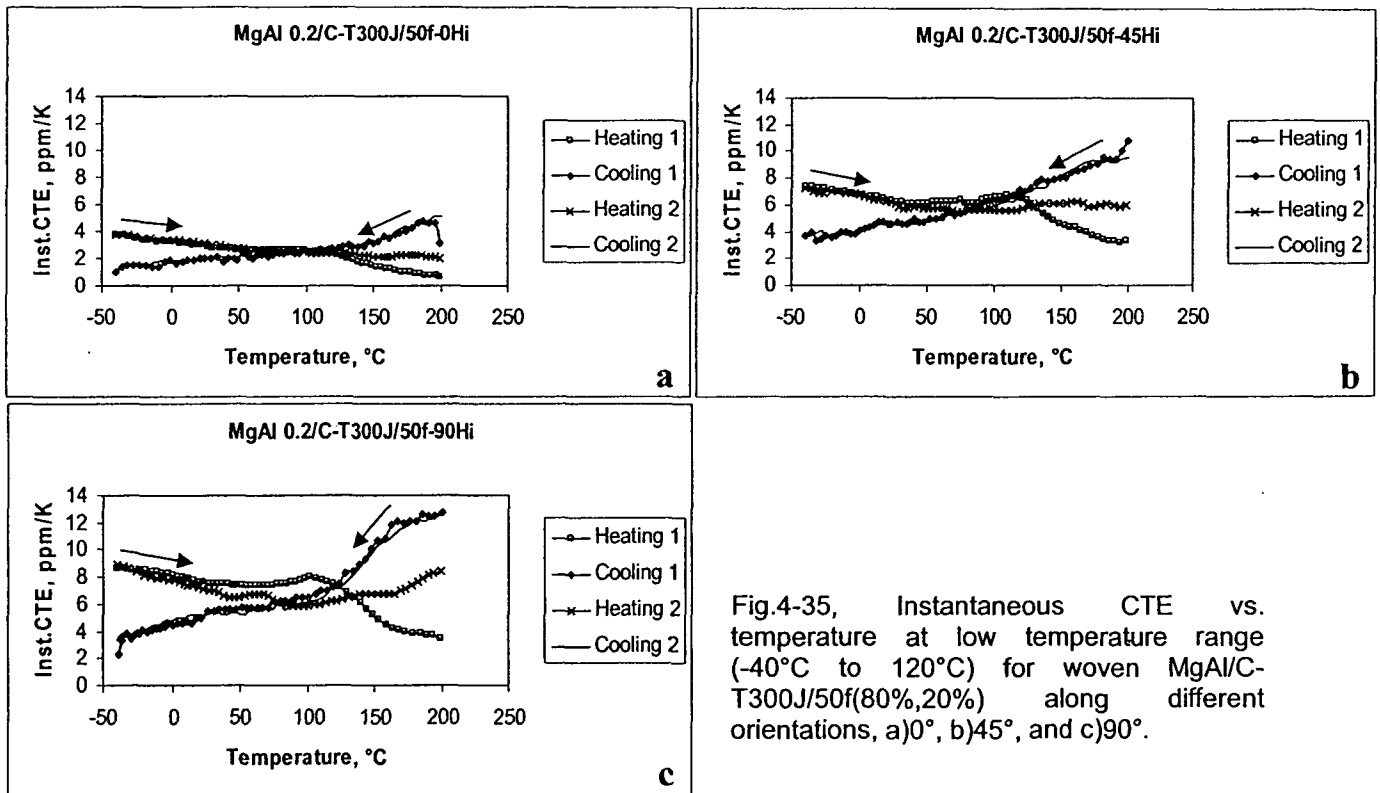


Fig.4-35, Instantaneous CTE vs. temperature at low temperature range (-40°C to 120°C) for woven MgAl/C-T300J/50f(80%,20%) along different orientations, a)0°, b)45°, and c)90°.

4.8. Damage

4.8.1. Damage due to thermal cycling

1000 thermal cycles by heating the Al/C-M40B specimen from room temperature up to 300°C have been done in order to evaluate the damage caused by thermal cycling in terms of density. The damage in density (according to void formation) D_p can be expressed as

$$D_p = 1 - (\rho_n / \rho_o)$$

where ρ_n is the density after n cycles and ρ_o is the initial density before cycling.

Fig.4-36 shows damage in density as well as decrease in density vs. thermal cycles. Also the effect of thermal cycling on CTE is shown in Fig. 4-37. The increase in CTE is more than 50% after 1000 cycles from the value of CTE in the first heating cycle which is attributed to local debonding. This damage is confirmed by evidence of cavities in the micrographs shown in Fig.4-38(a-d).

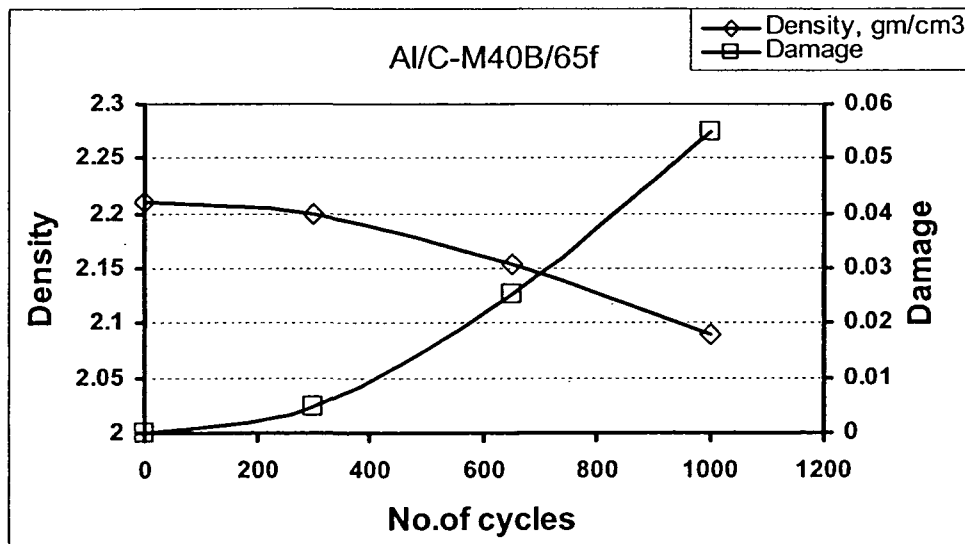


Fig.4-36, Density values and density damage vs. number of thermal cycles for Al/C-M40B/65f MMC.

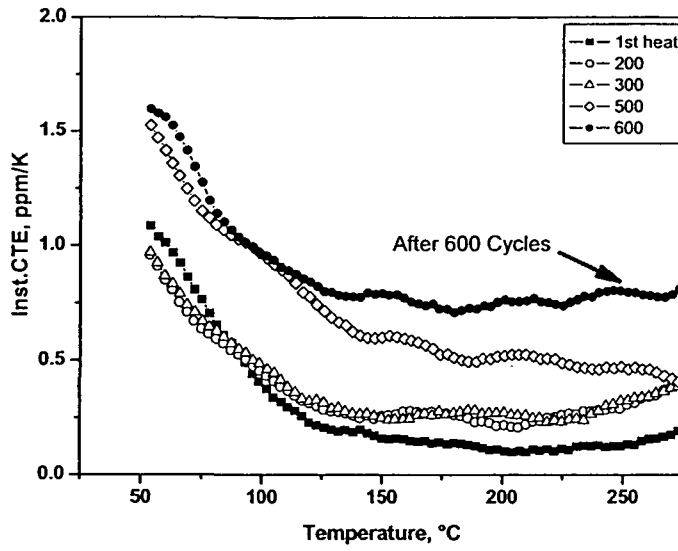


Fig. 4-37, CTE vs. temperature for Al/C-M40B MMC after different thermal cycles.

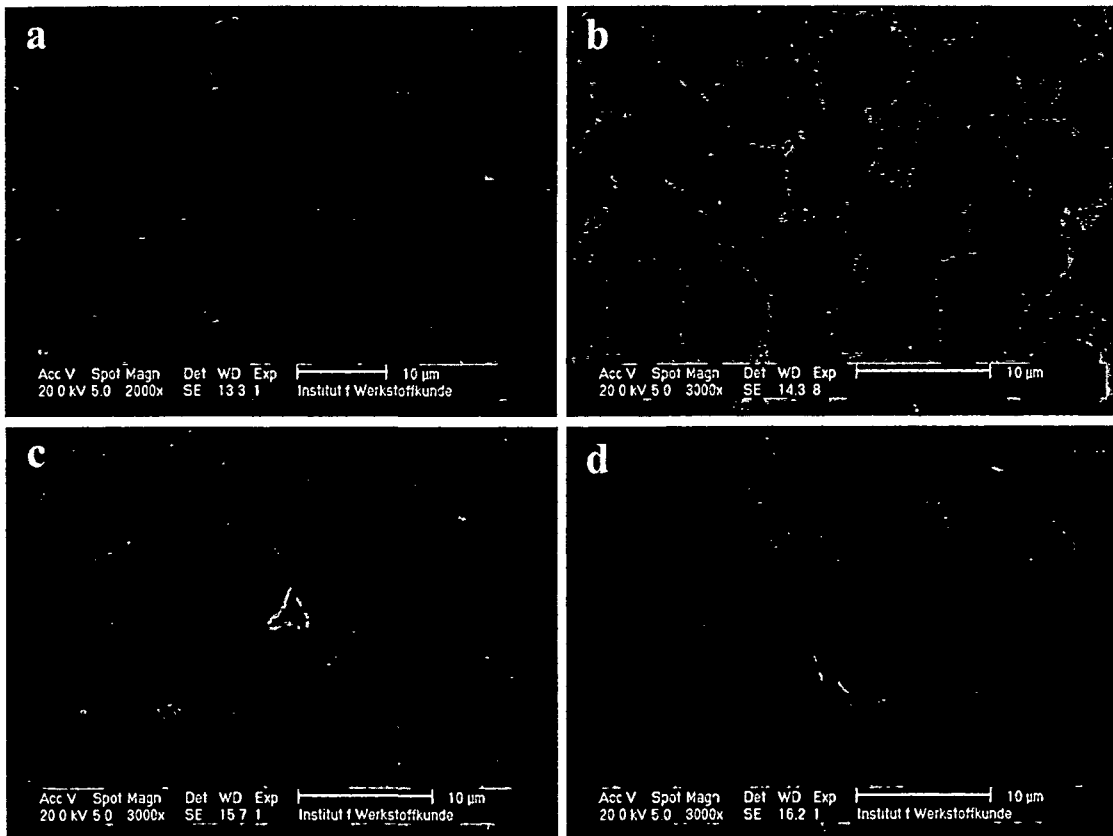


Fig.4-38, SEM micrographs for Al/C-M40B MMC after different thermal cycles, a) as received, b) 300 cycles, c) 650 cycles, and d) 1000 cycles.

4.8.2. Defects due to production conditions

In the infiltration process under the drive of the external pressure, the melt preferentially penetrates into the interconnected large interspaces at micro scale and then, penetrates the small ones when the local infiltration pressure increases up to the capillarity of the interspaces in question, causing; even if well distributed fibers from the beginning of preform preparation, the fibers to move as shown schematically in Fig. 4-39. This movement leads to different types of imperfections in fiber distribution.

According to the visualized melt flow behavior and the principles of hydrodynamics, statistic analysis of the effect of the dimension of the infiltrated interspaces, ranging from their maximum value $R_{eq,max}$ to the minimum $R_{eq,P}$, and their orientation D on melt flow in individual interspaces leads to the relationship between infiltration speed in terms of squeeze ram speed V_{ram} , and the local pressure gradient dP/dz in the infiltration direction z as follows

$$\frac{dP}{dZ} = \frac{A\mu V_{ram} R_{eq,max}^3}{D(1-V_f)(R_{eq,max}^5 - R_{eq,P}^5)}$$

where, μ is the dynamic viscosity of the matrix melt, A a constant determined by the infiltration system, and V_f preform fibre volume fraction. This equation shows that under a prescribed infiltration speed, the pressure gradient in the infiltrated preform is inversely proportional to $(R_{eq,max}^5 - R_{eq,P}^5)$, indicating the sensitive nature of infiltration pressure to the change of the dimension of the newly infiltrated interspaces [65].

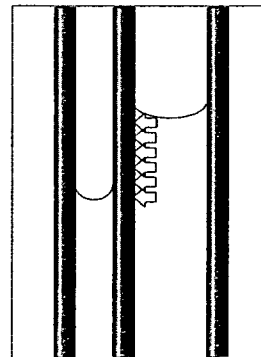


Fig.4-39, Fiber movement during infiltration process.

4.8.2.1. Unidirectional CFRM

Digital photography, radiography, followed by optical microscopy inspection for the received plates produced an overview about the defects accompanying the production of the gas pressure infiltrated plates for different fiber reinforced metal matrix composites. The defects ranging from movement of the fibers giving a nonuniform fiber distribution specially in the region between the fiber bundles. These defects illustrated in the Figs. 4-40 to 4-43. Fig.4-40 shows a fiber free region replaced by matrix in the center of the bundle as well as a bundle border filled with matrix material for Al/Al₂O₃-Nextel610/70f metal matrix composites. On the other hand, three veins in one plate detected by radiography and analyzed by the gray value for the radiograph and inspected by optical microscopy, as shown in Fig.4-41.

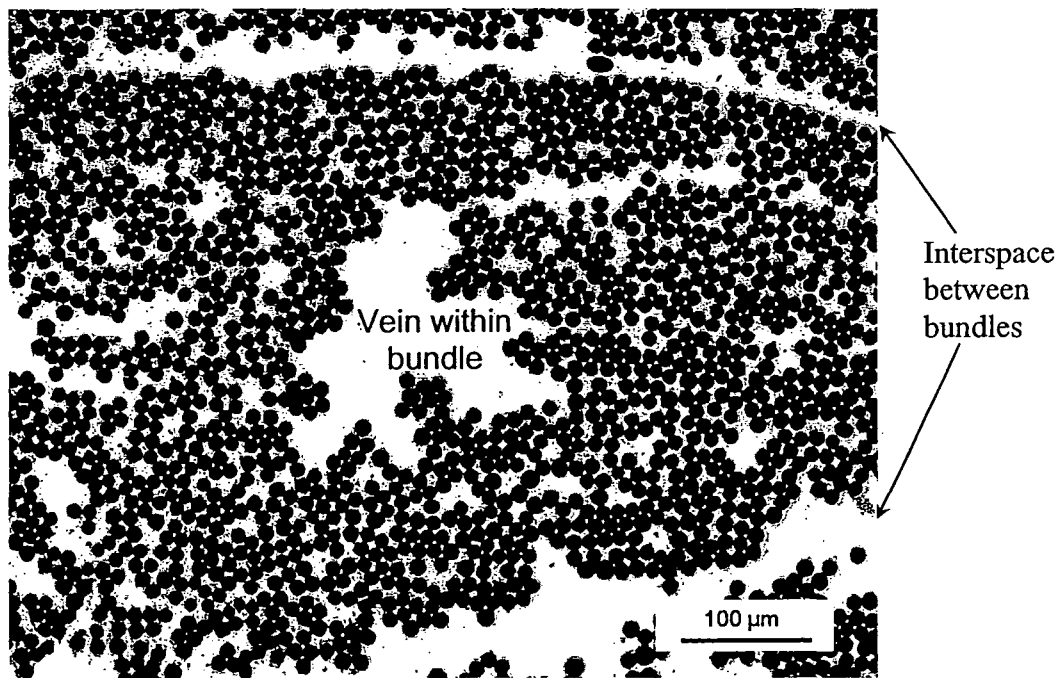


Fig.4-40, Nonuniform fiber distribution for AlMg/Al₂O₃-Nextel MMC.

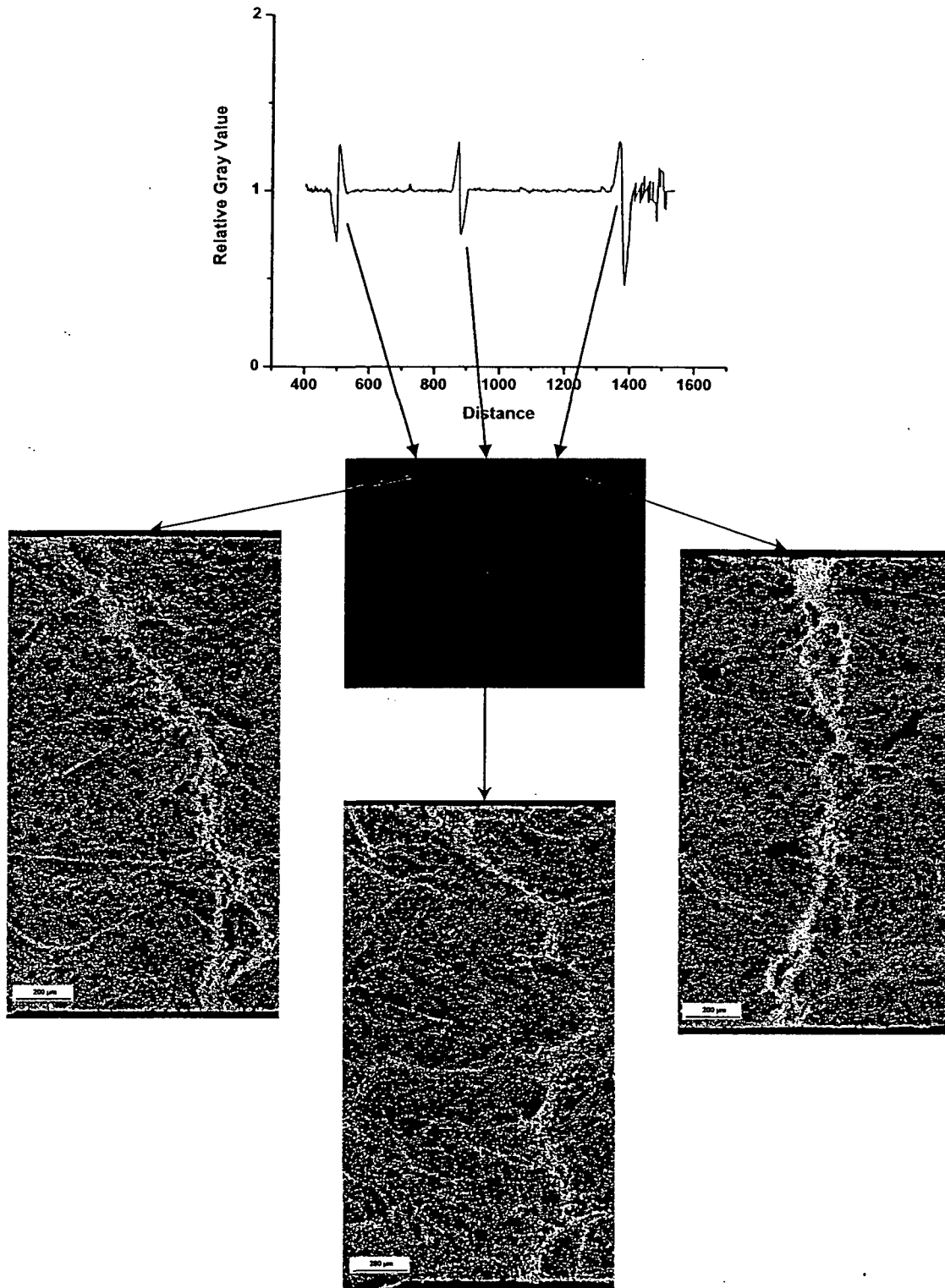


Fig.4-41, three metal channels appeared in the x-ray radiograph, cross sections and gray value difference curve in the V421 plate (Mg/M40), the black areas in the right hand picture is a preparation artifact.

Figs. 4-42 and 4-43 show black lines on the surface which indicate fibers coming out to the surface, also in Fig. 5, it is obvious that the fibers are not all parallel to the fiber axes.

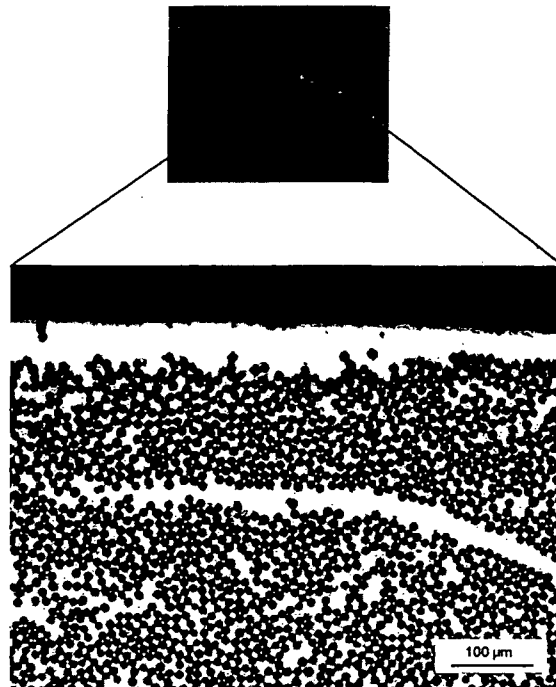


Fig.4-42, Part of digital photo for the surface of the plate showing black lines (upper) and cross section (lower).

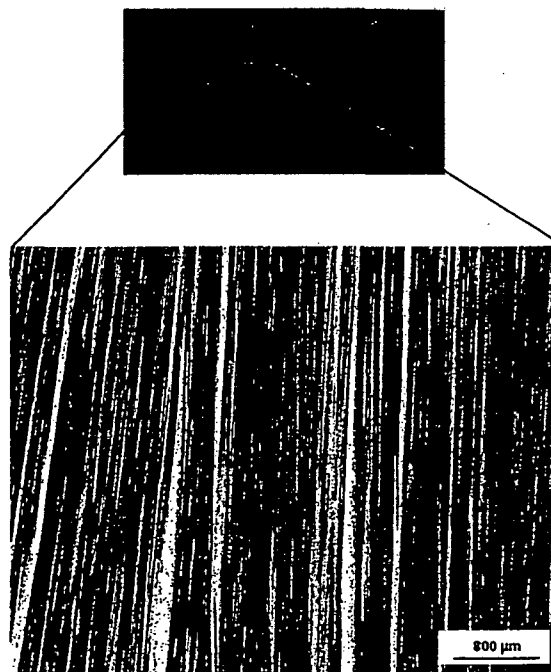


Fig.4-43, Part of digital photo for the surface of the plate showing curved black lines (upper) and a ground surface showing the curved fibers (lower).

4.8.2.2. Symmetric 6 layer specimens

The optical microscopy confirms perfect infiltration process for the fiber preform by the liquid aluminium. From the other hand some deviation was observed for the CTE measurements for the 15° inclination to the fiber direction.

Fig. 4-44 shows gray level images of reconstructed XCT recordings of planes parallel to the 6 fiber layers of an Al/C-M40B/64f (0,+60,-60, -60°, +60°, 0°) dilatometer sample cut 15° inclined to the 0° fibers in the surface layers, therefore the contrast follows the indicated angle. The orientation of the fibers can be clearly recognized by bright lines representing enrichments of matrix, which separate the fiber bundles. Layers 3, 4 and 6 look most densely packed, whereas layer 1 contains zones of reduced fiber volume fraction. Fig. 4-45 shows the XCT-image of a transverse plane of that sample and details of the layers in the metallographic pictures. The individual fibers are resolved by light optical microscopy but not by XCT, where the distribution of the fiber bundles is clearly visible. Enrichments of matrix can be recognized between the fiber layers, but as well in some veins across the layers, especially in layer 1. A black line can be observed in layer 6, which indicates a longitudinal crack, which cannot be resolved by microscopy of polished cross sections. The course of the veins and the crack can be traced by observing the planar XCT-images while travelling along the z-direction of the sample, which reveals that these inhomogeneities follow the fiber bundles.

The histograms of the gray levels of the described sample are shown in Fig. 4.46. Fig. 4.46a presents the peaks of the reference samples and those of the centers of layer 1 and 3. The peak of Gaussian shape of layer 3 is regarded as a benchmark distribution for densely packed infiltrated fiber bundles: the average gray level of such a perfect MMC corresponds to 67 vol% C_f , well within $68 \pm 2 \text{ vol\%}$ determined by quantitative metallography. The gray level peak of layer 1 is somewhat extended towards Al. Fig. 4.46b shows the gray level distributions of the whole sample, as well as of the upper and lower half separated by the dashed line in the inserted XCT image. The deviations can be quantified by subtracting a Gaussian curve: 25% of the histogram of the whole sample are

beyond the Gaussian shape concluding 75% of the sample consist of the respective perfect MMC with 67 vol% of fibers. The asymmetry of the sample can be quantified: the upper half contains 83% perfect fiber packing compared with only 67% in the lower, which corresponds to only 45 vol% C_f .

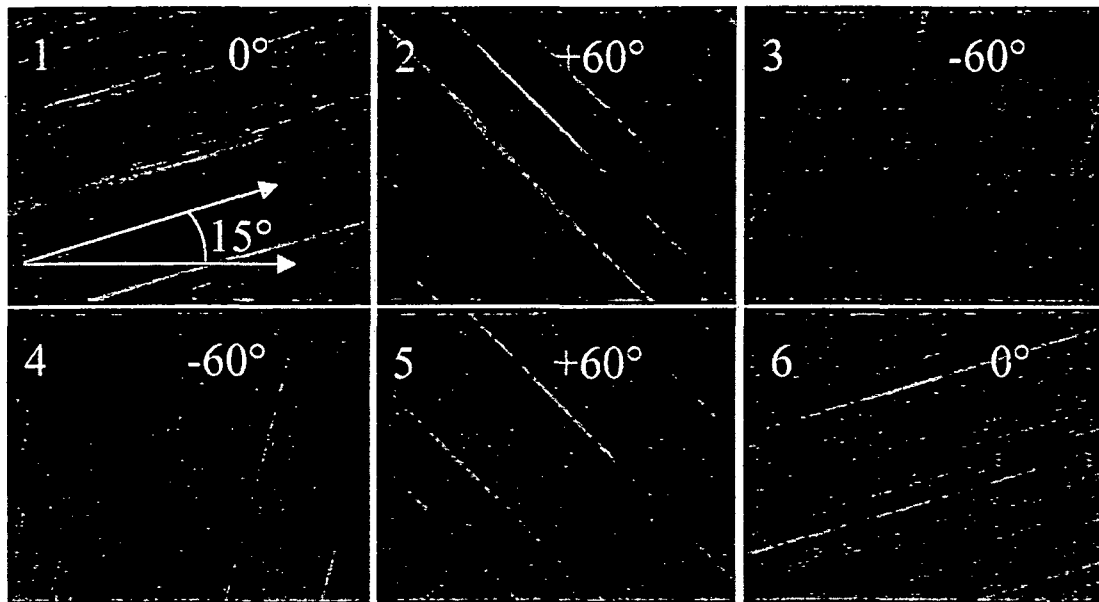


Fig.4-44: XCT image of a dilatometer sample of Al/C-M40B/64f (0,+60,2(-60),+60,0°) cut 15° inclined to the 0° surface fibers showing the central planes parallel to the 6 fiber layers.

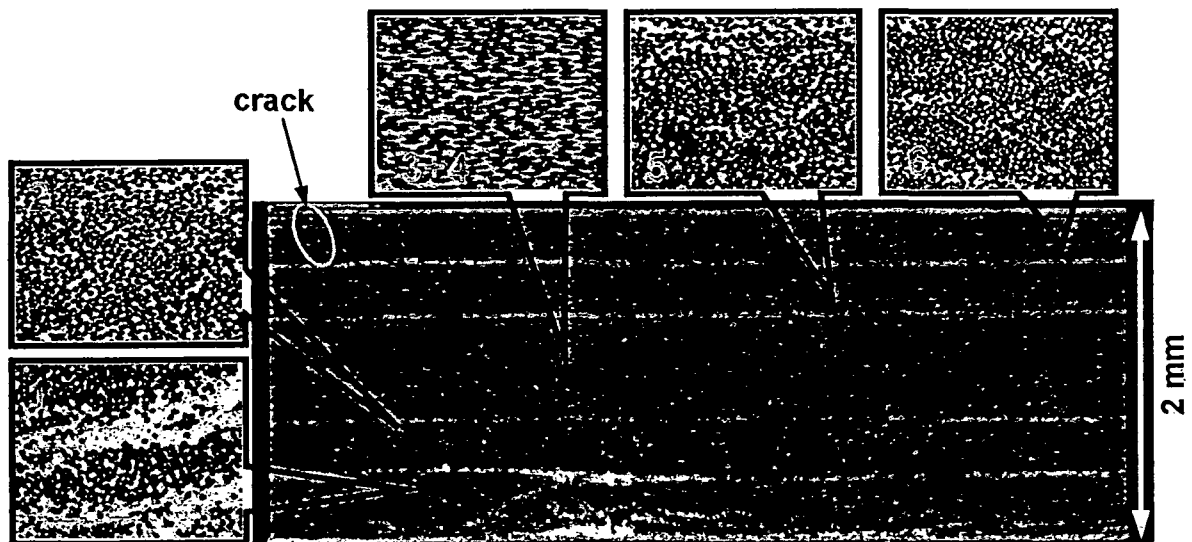


Fig.4-45: XCT image of a cross section of the same samples as in Fig. 3 showing the 6 fiber layers, Al interlayers, veins and a crack with details in inserts of light optical micrographs.

The gray levels integrated over planes parallel to the fibers (perpendicular to y) are plotted in Fig. 4-47, where the peaks reveal matrix agglomerations in between the fiber reinforced layers. The density maxima are used to measure the average thickness of each layer. The peak areas are compared with a theoretical step function distribution of pure Al (μ_{Al}) above the background of the MMC (μ_{MMC}), the resulting width of which is taken as the average thickness of the Al layer between the fiber rich layers. There is almost no Al interlayer between the parallel fibers of layers 3 and 4, but towards the adjacent layers rotated by 120° an average thickness of about $16 \mu\text{m}$ Al is measured. Altogether the Al interlayers occupy about 10% of the whole sample. The irregular fiber distribution in layer 1 yields a 30% higher thickness than that of layer 5 and 6. This is taken as an example for a quantitative quality criterion on fiber packing [66].

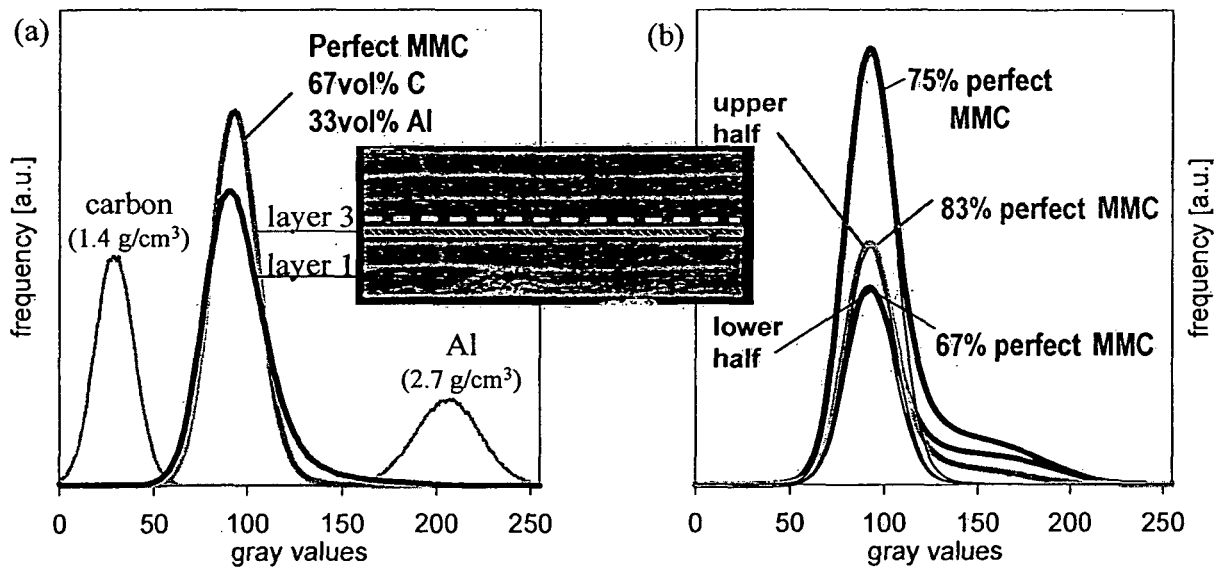


Fig.4-46: Histograms of XCT gray levels of sample Al/C-M40B/64f (0,+60,2(-60),+60,0°) according to the inserted XCT cross section: (a) within the depicted sections in layer 1 and 3 together with the reference masses of graphite and Al; layer 3 provides a Gaussian distribution representing a perfect fiber packing. (b) Histograms of the whole sample, the lower and the upper half (separated by the white dashed line in the insert) compared with the corresponding Gaussian distribution (narrow lines) yield the percentages of overlap as indicated.

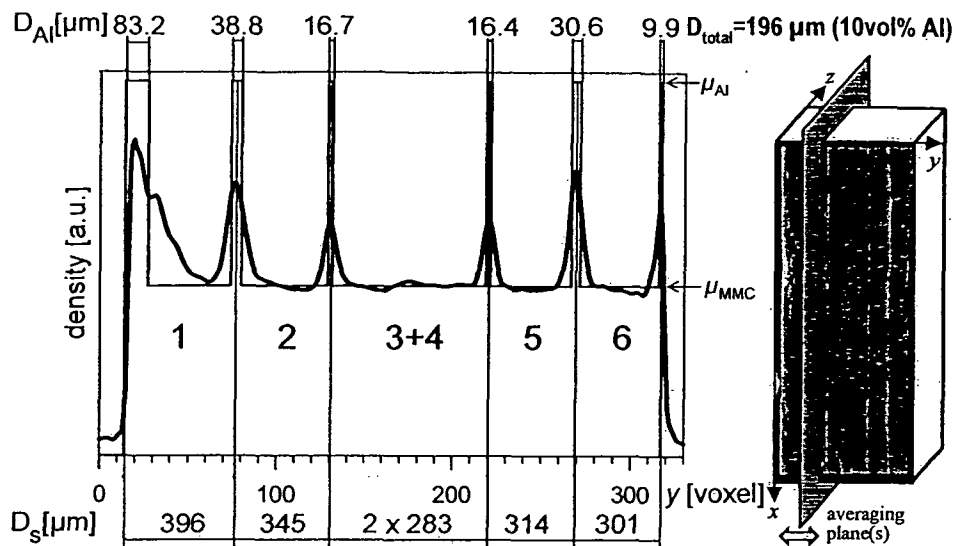


Fig.4-47, Average density profile of the x/z -planes of XCT as indicated in the insert of the sample (same as Fig. 4.44-46) producing peaks at the Al interlayers, the peak areas of which are equal to the rectangles $(\mu_{Al} - \mu_{MMC}) \cdot D_{Al}^{(0)}$, providing the indicated thickness values summed up to 196 μm . The distances between the peaks yield the thickness of the fiber layers $D_s^{(0)}$.

4.9. Matrix yield strength

Using gleeble machine, compression test on the pure aluminum, pure magnesium and magnesium with 0.6% aluminium matrices has been done for determining the true stress-strain curve as shown in Fig. 4-48 a-c. Materials tested at temperatures of 50°C, 100°C, 150°C, and 200°C, under low strain rate of 0.001 /s. In case of pure aluminium specimens, no big difference in yield strength between different temperatures was observed, so, only the highest and lowest temperatures were shown. Table 4.9, shows the measured Young's modulus values for different materials at different temperatures. The matrix hardening modulus is averaged in the range of 0.02 - 0.04 strain.

For determining the flow stress and temperature for pure aluminium and magnesium, the specimens constrained in length by the machine jaws. The temperature was increased from room temperature with a rate of 3 K/min to simulate the conditions of the CTE measurements. The flow curves are shown in Fig. 4-49 a,b. The stress increases steadily up to about 80°C for Al and about 75 for Mg. Then follows a short strengthening period due to plastic deformation

passing a maximum of 53 MPa at 130°C for Al and 37 MPa at 110°C for Mg. Increasing the temperature further the stress exerted by thermal expansion decreases. This effect is called softening and is originated from the decreasing yield stress with increasing temperature and relaxation of preceding strain hardening as exposure time proceeds.

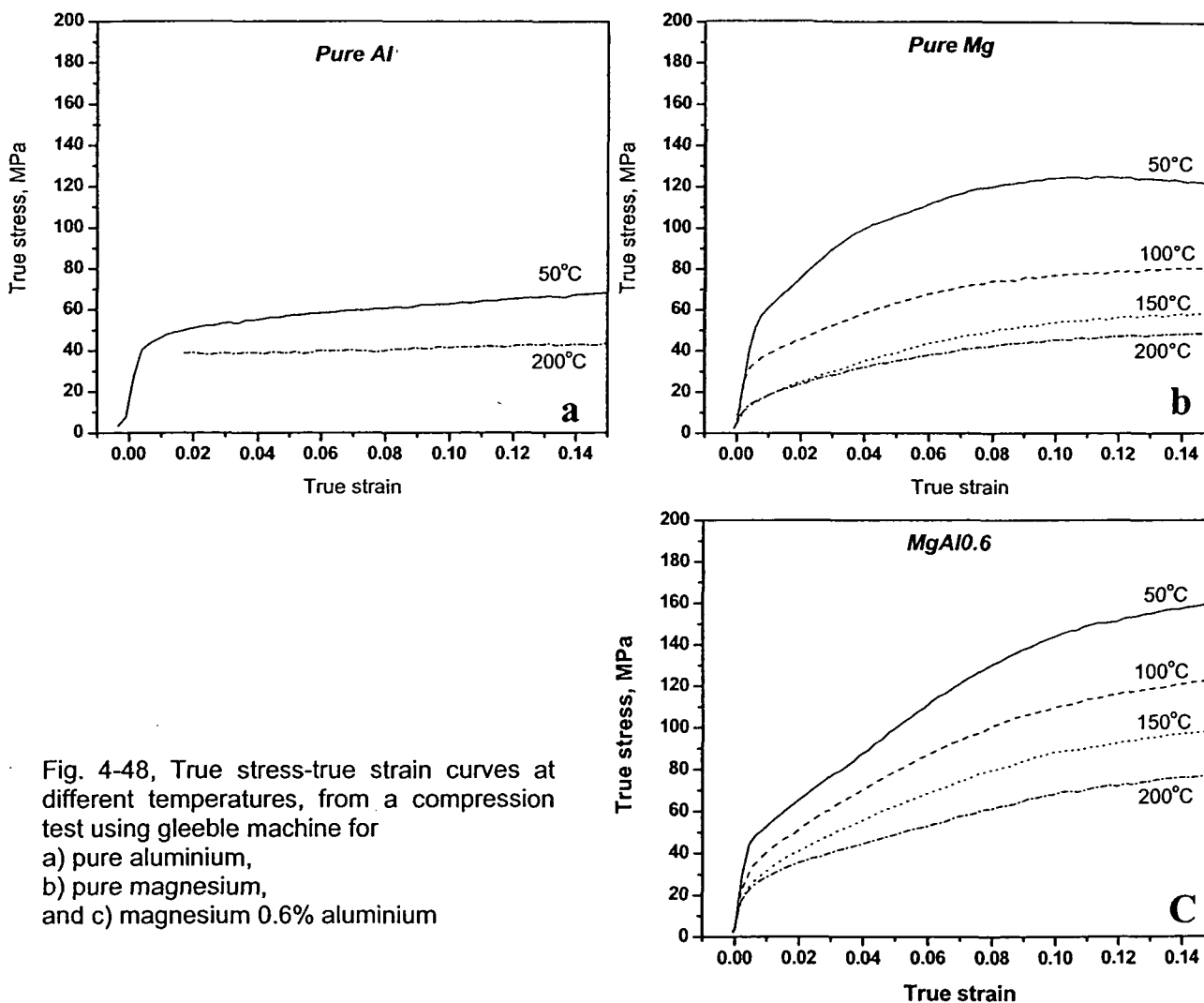


Fig. 4-48, True stress-true strain curves at different temperatures, from a compression test using gleeble machine for
 a) pure aluminium,
 b) pure magnesium,
 and c) magnesium 0.6% aluminium

Table 4.9, Calculated modulus values according to the Gleeble tests.

Temperature, °C		Elastic and hardening mod., GPa		
		MgAl0.6	Al	Mg
RT		45	69	45
50	Matrix hardening	1.2	0.07	1.4
100	Elastic	43	67	43
	Matrix hardening	0.9	0.07	0.7
150	Matrix hardening	0.7	0.04	0.5
200	Elastic	40	63	40
	Matrix hardening	0.4	0.3	0.4

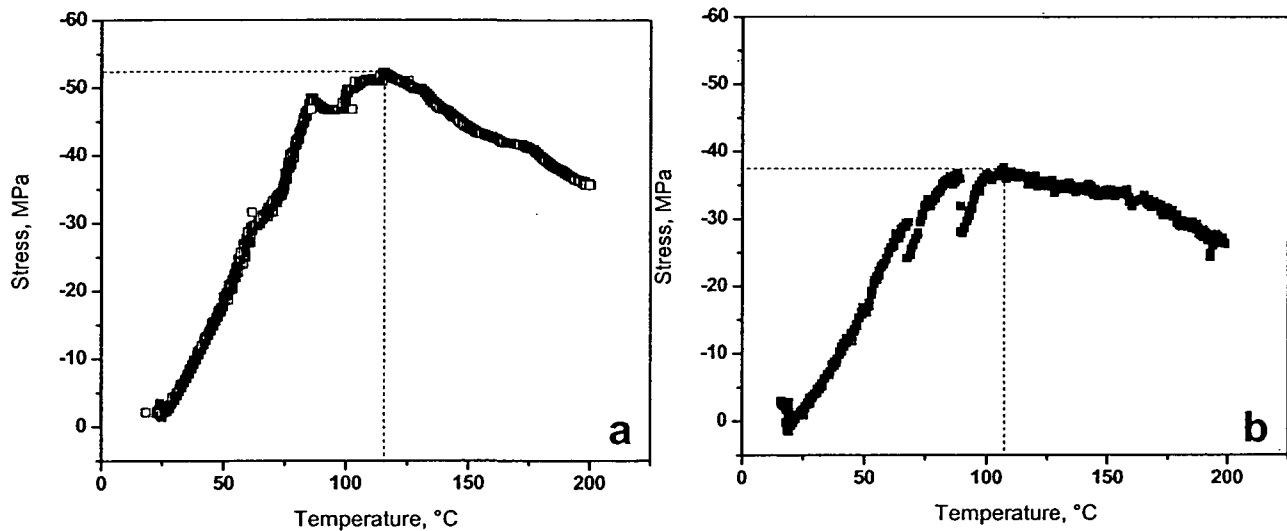


Fig. 4-49, Stress-temperature curve produced from Gleeble test for constrained (in length) specimens of a) commercially pure aluminium and b) commercially pure magnesium.

5. Discussion of results

5.1. Al based UD MMCs

5.1.1. Al/C-M40B/65f

The reaction between carbon fibers and aluminium which produces aluminium carbide (Al_4C_3) increases the bonding between fibers and matrix even after very short periods of contact between melt and fibers during processing. Considering the high modulus carbon fibers reinforced commercial pure aluminium system, the fibers have a longitudinal E-modulus of 392 GPa, and the transverse value is approximately 7 GPa, thus, the unidirectional aluminium carbon fiber composites are highly anisotropic in behavior. The estimated value of longitudinal E-modulus from the rule of mixtures is 280 MPa, and the transverse value results in 11 GPa. The E-modulus value measured by DMA is higher than the value estimated by the rule of mixtures, while the value measured by resonant beam technique is lower than the values obtained by the rule of mixtures. Using the values of longitudinal and transverse moduli produced from the DMA measurements and the shear modulus produced from the resonant beam technique, as inputs to the laminator software to predict the off-axis Young's moduli at different directions, the experimental off axis DMA values show a good agreement with the theoretical values produced from the calculations. The storage modulus produced from the DMA, like other DMA property data, indicate only relative rather than absolute values since the measurements are influenced by experimental conditions and instrumentation compliance. The polar diagram in Fig. 5-1 shows the experimental and theoretical values of E-modulus.

Using the stress strain curves for the Al matrix as a result from the Gleeble compression test as shown in Fig. 4-48, the yield strength of the aluminium is 43 MPa at 50°C, and 38 MPa at 200°C. In this consideration no initial residual stress is assumed. Initial tensile stresses in the matrix are certainly introduced when the sample is cooled to -40°C. Heating from -40°C reduces the tensile stress in the matrix converting into compression at a certain temperature. Thus elastic

deformation of the matrix may extend from the yield stress in tension to that of compression. Thus plastification of the matrix is expected at a certain temperature change.

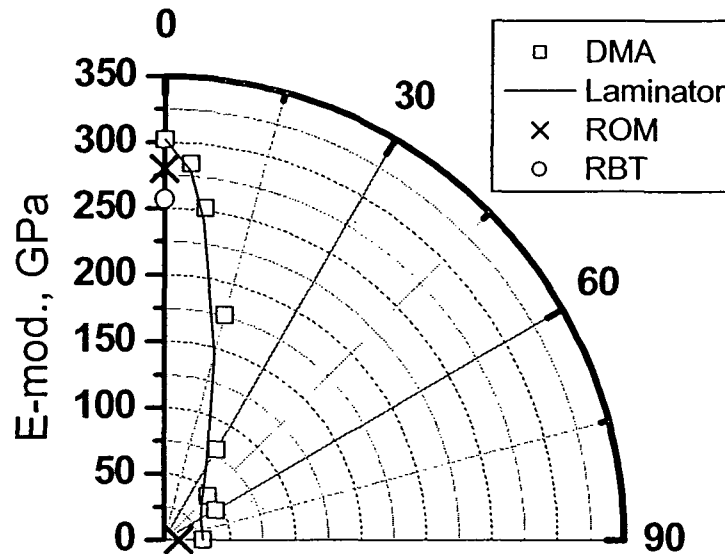


Fig. 5-1, Al/C-M40B/65f polar diagram for Young's modulus vs. orientation measured by dynamic mechanical analysis, resonant beam technique and estimated by rule of mixtures (data calculated by laminator based on the longitudinal and transverse moduli that measured by DMA).

From the dilatation curve for the temperature range from room temperature to 525°C shown in Fig. 5-2a, the whole range can be divided into four zones; the first zone is matrix elastic zone followed by the plastic deformation of the matrix subdivided into strain hardening, then softening of the matrix and at higher temperature the matrix protrusion zone is postulated, i.e. matrix flows beyond the fibers at the end-on-surfaces of the specimen ($< 3 \mu\text{m}$). According to Schapery's estimation of thermally induced matrix stress,

$$\sigma_m = E_m (\alpha_c - \alpha_m) \Delta T \quad (5.1.1)$$

where σ , E , α and T stand for stress, Young's modulus, coefficient of thermal expansion, and temperature, the subscripts m , c stand for matrix and composite, respectively.

With a stiffness value of C-M40B fibers of 392GPa in the fiber direction and 70 GPa of the matrix, with volume fraction of fibers of 0.65 and coefficient of thermal expansion of matrix and composite of 23 and 1.44 ppm/K, respectively, a ΔT of one degree produces a matrix stress of 1.48 MPa. As shown in the dilatation curve in Fig.5-2b, yielding of the matrix begins at approximately 5°C, which means 45 K from the beginning of the experiment at -40°C. Longitudinal stresses of 67 MPa are produced in this temperature range if the matrix deformed elastically. If we assume the matrix begins with tensile residual stress of 24 MPa at the temperature of -40°C, passing through zero going to compression during heating, it reaches the yield stress of 43 MPa at 5 °C. Plastic deformation under compression increases the yield stress of the matrix from 43 MPa to about 52 MPa by strain hardening, reaching a maximum at a ΔT of approximately 110 K (at 70°C). At this temperature the matrix begins to soften due to the decrease of the matrix yield strength and by recovery and creep relaxation causing a decrease in the tensile load on the fiber which in turn produces a relative contraction (reduction in the strain) of the fibers and hence the pertained matrix which follows the thermal behavior of the fibers until the end of the first heating cycle up to 120°C.

The aluminium matrix starts to soften from a strength of 52 MPa at the temperature of 115°C up to 200°C, as shown in the stress-temperature curve produced from the Gleeble test for the constrained specimens after a temperature increase of 85 K from room temperature. This gives an indication that the matrix may begin to soften in the temperature range between 45°C (-40+85) and 115°C. According to Fig. 5.2b matrix softening begins at 70°C until the end of the first cycle at temperature of 120°C. This interpretation is illustrated in Fig.5-4.

Upon cooling, the yield strength of the matrix is estimated from the Gleeble test to be approximately 40 MPa at 120°C, while the matrix compression and the fiber

tension are reduced upon cooling experimentally a higher shrinkage rate is observed which in turn appears as a higher CTE for cooling than heating in the instantaneous CTE against temperature curve shown in Fig. 5-3. Some effect may be associated to some matrix protrusion (range of μm) during heating which would be reversed as soon as the course of temperature is reversed, but the uncertainty in the stress and temperature dependence of the C-fiber properties may cause such differences as well. The stress of the matrix converts from compression into tension elastically with decreasing temperature and starts to yield in tension at approximately 65°C , when the temperature had changed by 55 K . The corresponding change in elongation between 120°C and 65°C amounts to about -10^{-4} strain, which equals to an elastic straining of the fibers by a change in stress of about -39 MPa , which is close to the residual stress change in the matrix estimated by $(1-v_f) \Delta\sigma_m = 0.35 \times (40+43) = 30\text{ MPa}$. The tensile stress in the matrix is increased and it starts to flow producing some strain hardening until the end of the first cycle producing some residual stress higher than that existing in the specimen before the dilatometer cycles. Calculating the coefficient of thermal expansion in the last segment in the cooling cycle using the simple relation $\Delta\varepsilon = \Delta\alpha \Delta T$ with the strain difference of -0.0036% (coming from -0.0056% to -0.0020%) and a temperature difference of 60 K , this gives a value of -6×10^{-7} for $\Delta\alpha$ which approximately equals the nominal coefficient of thermal expansion of the M40B carbon fibers with negligible change in compression by the matrix.

Regarding the specimen contraction in fiber direction after the first cycle, the following conclusions on the residual stresses can be drawn:

$$1^{\text{st}} \text{ cycle } -40^\circ\text{C to } 120^\circ\text{C}, \Delta L/L_0 = -2 \times 10^{-5},$$

$$\text{fiber compression } \Delta\sigma_f = -2 \times 10^{-5} \times 392 \times 10^3 \text{ MPa} = -8 \text{ MPa},$$

$$\text{matrix stress increase } \Delta\sigma_m' = -v_f \Delta\sigma_f / (1-v_f) = 15 \text{ MPa}.$$

For the second cycle at the same temperature range, the beginning of the cycle is shifted to a lower value of strain due to residual stresses accumulated during cooling, the behavior is the same like the first cycle but approximately without

introducing new stresses at the end of the cycle, which means that the second cycle is always reproducible.

For the high temperature range cycle, no difference is observed in the behavior of the dilatation curve up to 120°C, the same stress state for all stages, the only difference is with increasing temperature, the softening of the matrix during heating is continued due to the higher temperature and lower strength of the matrix. The residual stresses could be estimated in this temperature range from -40°C to 200°C as, fiber compression $\Delta\sigma_f = -2 \times 10^{-5} \times 392 \times 10^3 \text{ MPa} = -8 \text{ MPa}$,

matrix stress increase $\Delta\sigma_m'' = -v_f \Delta\sigma_f / (1-v_f) = 15 \text{ MPa}$.

With the assumption of an initial residual stress of 24 MPa, the first cycle to 120°C adds ca. 15 MPa and the third cycle to 200°C further 15 MPa, summing up to 54 MPa residual longitudinal stresses in the matrix. A schematic diagram shows the axial longitudinal stress component in Al/C-M40B MMC changing with temperature cycles as described in Fig.5-4.

With increasing angle of inclination to the fiber axis up to 30°, the behavior is completely different, the effect of the residual stress component in the direction of measurement is much lower than in fiber direction. As long as the tensile stress along the fibers is reduced during heating, the expansion at any angle deviating from the fiber orientation is accelerated until about -15°C, when compression builds up (Fig. 4-22b). During cooling the contraction is decelerated as soon as tensile stresses are plastifying the matrix ($T < 20^\circ\text{C}$). The width of the hysteresis decreases with increasing angle of inclination to the main fiber axis for both low and high temperature ranges. In the 60° and transverse specimens almost linear behavior for the dilatation curve reflects the smaller CTE mismatch between fibers in transverse and matrix (Fig4-21d,e). A contraction was observed in the transverse samples at the end of every first heating/cooling cycle, this is attributed to the effect of Poisson's ratio in the transverse direction due to the elastic tensile expansion of the matrix in the direction of fibers.

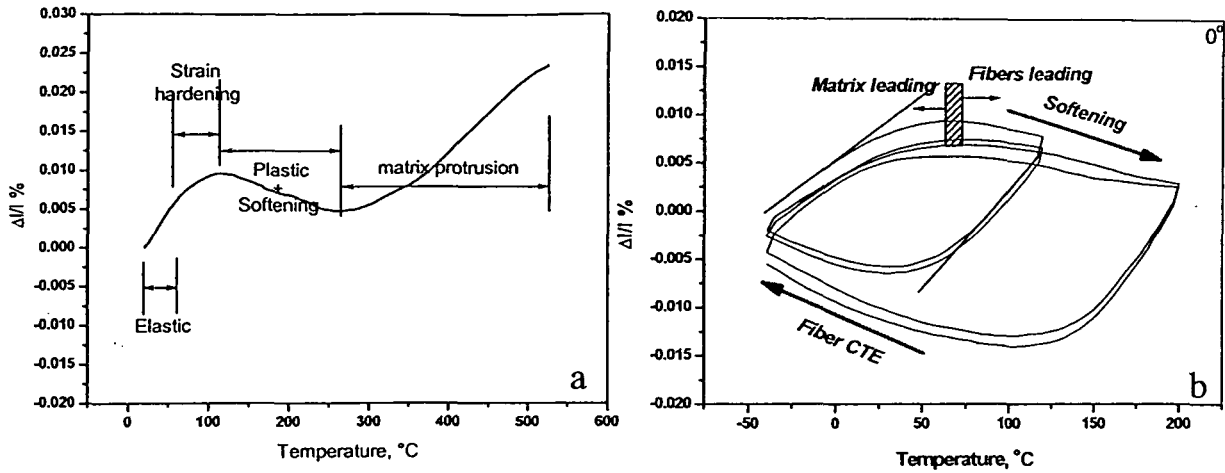


Fig. 5-2, Dilatation curve for Al/C-M40B/65f UD showing different regions during thermal cycling, a) heating from RT to 525°C b) four heating/cooling cycles from -40°C to 120 and 200°C.

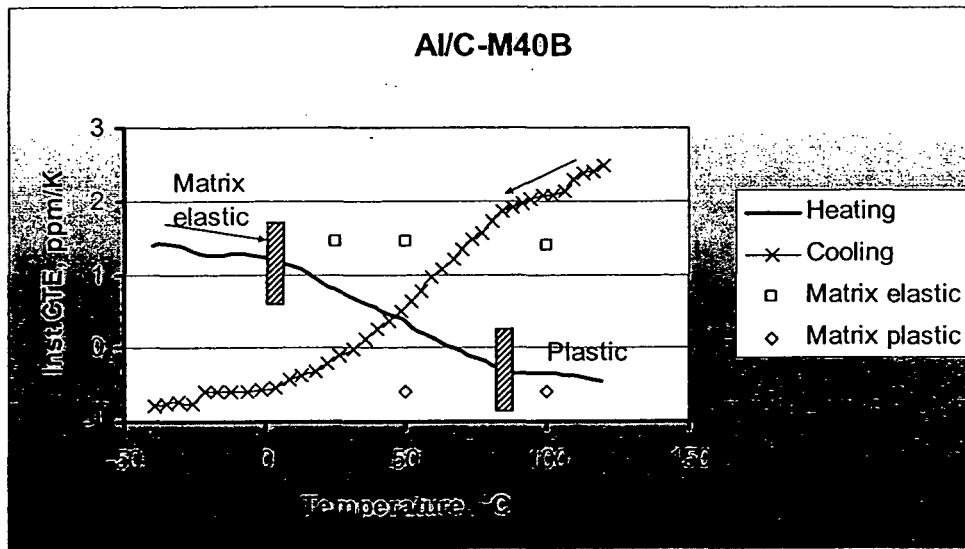


Fig. 5-3, Instantaneous CTE vs. temperature for Al/C-M40B/65f during heating and cooling, and values of CTE calculated by considering elastic matrix according to Schapery and matrix plastic according to Böhm.

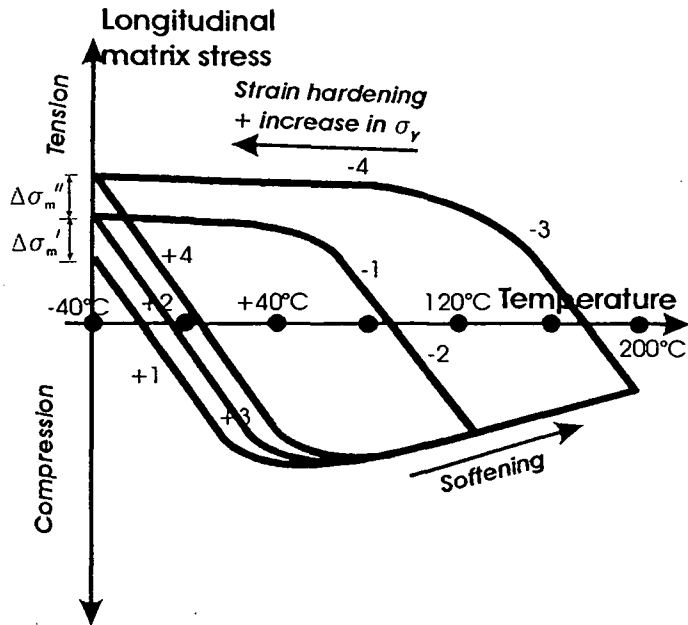


Fig. 5-4, Schematic estimation of longitudinal matrix stress during thermal cycling, two cycles in the temperature range from -40°C to 120°C (± 1 , ± 2) and two cycles from -40°C to 200°C (± 3 , ± 4)

The instantaneous coefficient of thermal expansion is decreasing with increasing temperature and different stress regions appear in the curve shown in Fig. 5-3. The theoretical values of CTE calculated from Schapery's model as well as the modified model by Böhm for the matrix hardening are shown in Fig. 5-3. The matrix moduli were calculated from the stress strain curves shown in table 4-9. The measured values of the CTE are in good agreement with the models considering a continuous transition between fully elastic and ideally plastic matrix deformation. Only the first period of cooling yields higher CTE than predicted by the elastic model, which is attributed to the change in the sign of the stresses and some contribution from reversion of protrusion. A temperature dependence of the fiber properties could be another reason.

A polar diagram for CTE values at different temperatures versus orientations is illustrated in Fig. 5-5, showing the anisotropy of this type of MMC, the lowest value is in the fiber direction, while the highest is in the transverse direction. For

comparison the technical expansion coefficient are given as well, which indicate as well a slight dependence on the corresponding temperature interval.

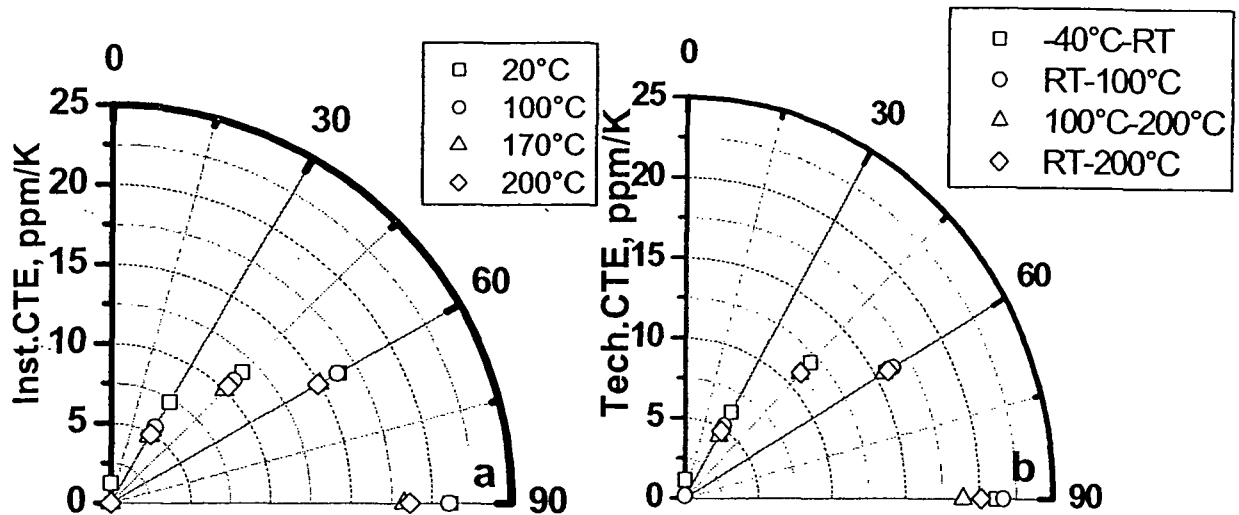


Fig. 5-5, Polar diagram at different temperatures vs. orientation for Al/C-M40B/65f for a) instantaneous CTE and b) technical CTE measured in different temperature ranges.

5.1.2. AlMg1/Al₂O₃-Nextel610/65f

The diffusional reaction between Mg in the aluminium matrix and alumina fibers produces a relatively good bonding between matrix and fibers. The isotropy of the fibers lead to small differences between the longitudinal and transverse properties, which can be easily observed from the polar diagrams in Fig. 5-6 a,b. The estimated value of longitudinal E-modulus from the rule of mixtures is 267 MPa, and the transverse value is 148 GPa, this reflects the less anisotropic behavior of this MMC system. Based on the longitudinal and transverse values measured by four point bending test and the shear modulus measured by resonant beam technique, the E-moduli values in off-axis directions calculated using the laminator software and the values show a good agreement with the model. Except the pulsed laser ultrasonic technique E-modulus values, the values obtained by different methods have a good agreement with each other.

The strength to failure is still highly anisotropic: almost 4-times as high in longitudinal direction compared with transverse direction. The efficiency of the global load distribution is much better than with C-fiber reinforcement, thus achieving higher strength levels in all directions.

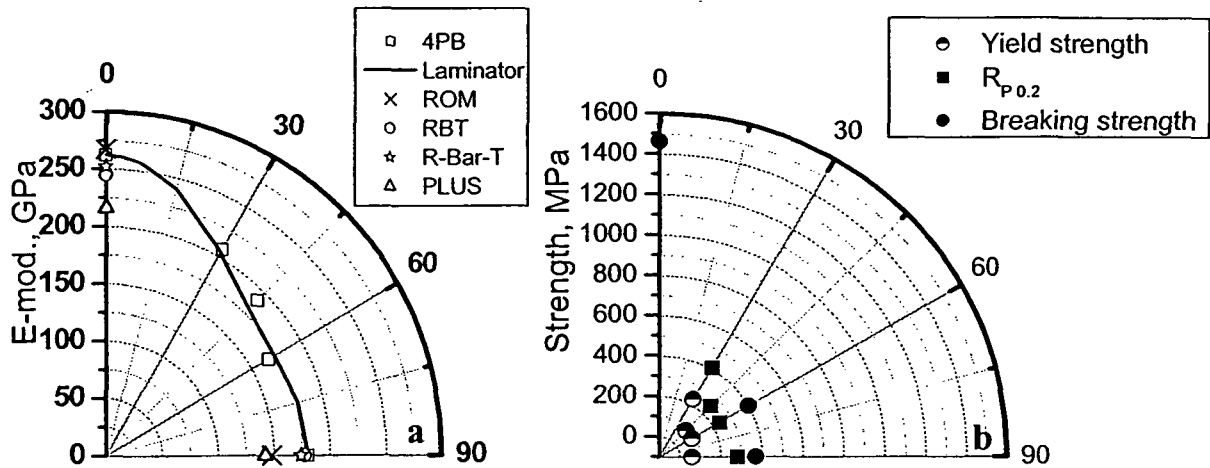


Fig. 5-6, Polar diagram for AlMg1/Nextel610/65f a) Young's modulus vs. orientation measured by four point bending, resonant beam technique, resonant bar technique, and pulsed laser ultrasonic and calculated by laminator and rule of mixtures, b) strength.

For the thermal behavior, it is well known that the yield strength for aluminium is increasing with increasing magnesium addition. From the curve shown in Fig.5-7, the addition of about 1% Mg to

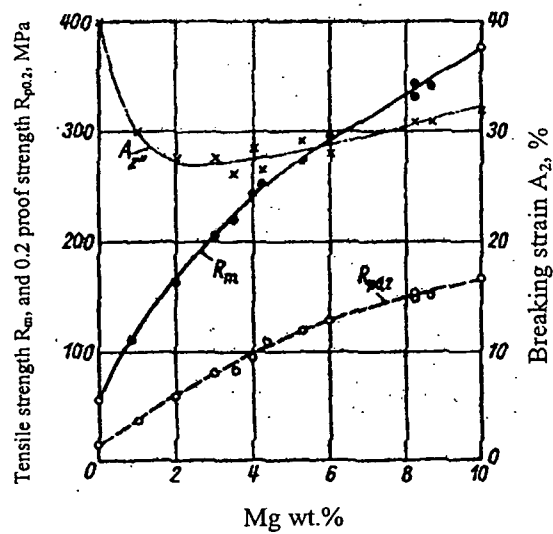


Fig. 5-7, Effect of magnesium addition to aluminium on tensile strength, proof stress, and breaking strain [67].

aluminium doubles the yield strength of pure aluminium [67]. Considering the strength of aluminium at room temperature to be like the previous case which is 43 MPa, then the yield strength for the aluminium matrix with 1% magnesium is assumed to reach about 86 MPa. The relatively small mismatch between fiber and matrix lowers the mismatch stresses with respect to the previous MMC system. From the dilatation curve shown in Fig. 5-8, the behavior of the curve is linear up to a temperature of 150°C, with a ΔT of 190K, this gives a stress of 180 MPa based on a matrix stress of 0.95 MPa for every $\Delta T=1K$ calculated from the equation (5.1.1), using coefficient of thermal expansion of the composite as 9.2 ppm/K. With increasing temperature, the slope of the curve changes at about 50°C, which indicates a change in the stress of the matrix from tension to compression, and the change in slope may be due to the non linear elastic behavior of the alumina fibers [68]. Given by B. Moser et al [68] that the “third order” elasticity for the tensile modulus of an isotropic material can be described using the following equation,

$$\sigma_f(\varepsilon) = E_f \varepsilon + (K/2) \varepsilon^2$$

where K equals 2540 for Nextel alumina fibers.

The low mismatch between matrix and fibers and the high yield strength of the AlMg alloy displace plastification of the matrix to higher temperature (above 150°C). The protrusion can be seen above temperatures of approximately 340°C (ΔT of 320 K) in the dilatation curve up to 525°C shown in Fig. 5-8b.

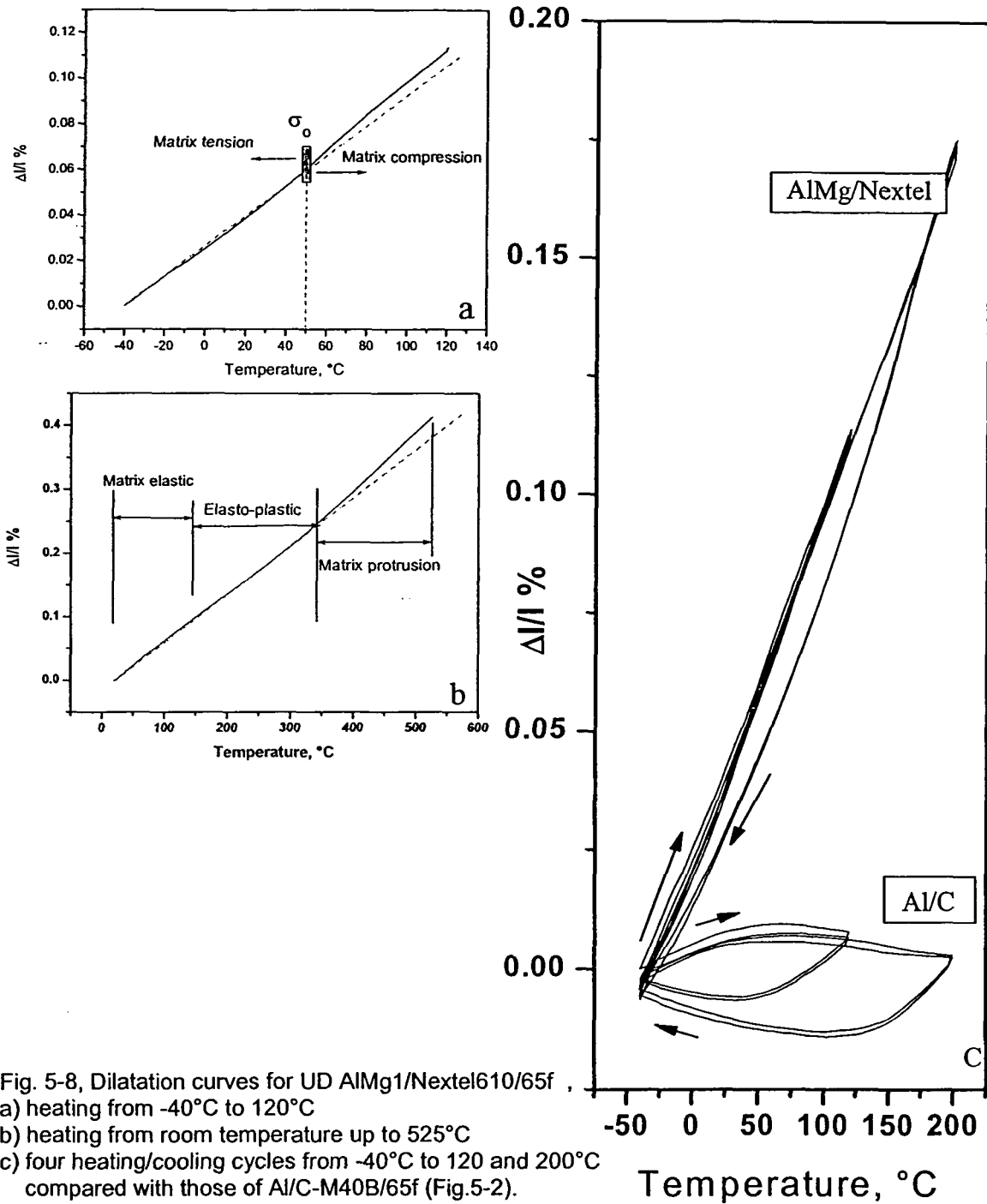


Fig. 5-8, Dilatation curves for UD AlMg1/Nextel610/65f ,
 a) heating from -40°C to 120°C
 b) heating from room temperature up to 525°C
 c) four heating/cooling cycles from -40°C to 120 and 200°C
 compared with those of Al/C-M40B/65f (Fig.5-2).

The thermal cycles between -40°C and 120°C seem to produce purely elastic strains.

For the thermal cycling at higher temperature range from -40°C to 200°C (ΔT of 240 K), the cooling cycles indicate some plastification. A schematic diagram shows the longitudinal matrix stress in case of AlMg/Nextel610 MMC qualitatively with temperature in the longitudinal direction in Fig.5-9.

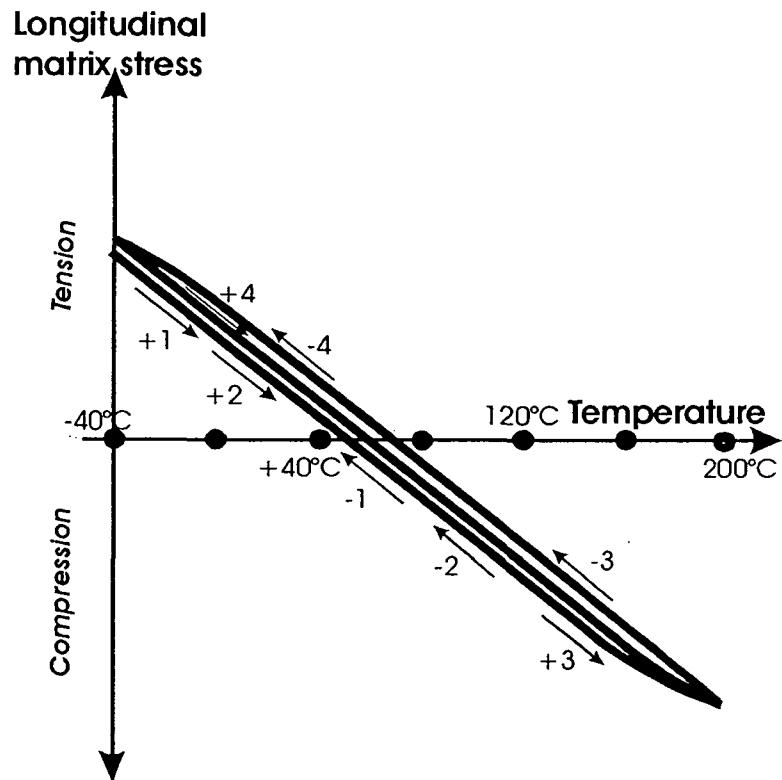


Fig. 5-9, Schematic estimation of longitudinal matrix stresses during thermal cycling of AlMg1/Nextel, two cycles in the temperature range from -40°C to 120°C (± 1 , ± 2), and two cycles from -40°C to 200°C (± 3 , ± 4)

Deviation from the fiber direction is less sensitive than the previous MMC system. The transverse properties of CFRM with ceramic fibers are similar to those of particle reinforced systems because of the good bonding between fibers and matrix. The increase in the total strain in the 30° , 45° , 60° , and 90° directions with respect to previous direction step is 29%, 18%, 15%, and 16% (Fig. 4-18a-e), respectively.

Applying the Schapery model on the Al/Nextel MMC shows that the measured values are lower than that estimated by the model as shown in Fig. 5-10.

A polar diagram for CTE values at different temperatures versus orientations are illustrated in Fig. 5-11, showing the lower anisotropy of this type of CFRM compared to the carbon fibers reinforced MMCs. There is almost no difference between the instantaneous and technical CTE values as shown in the polar diagrams in Fig. 5-11.

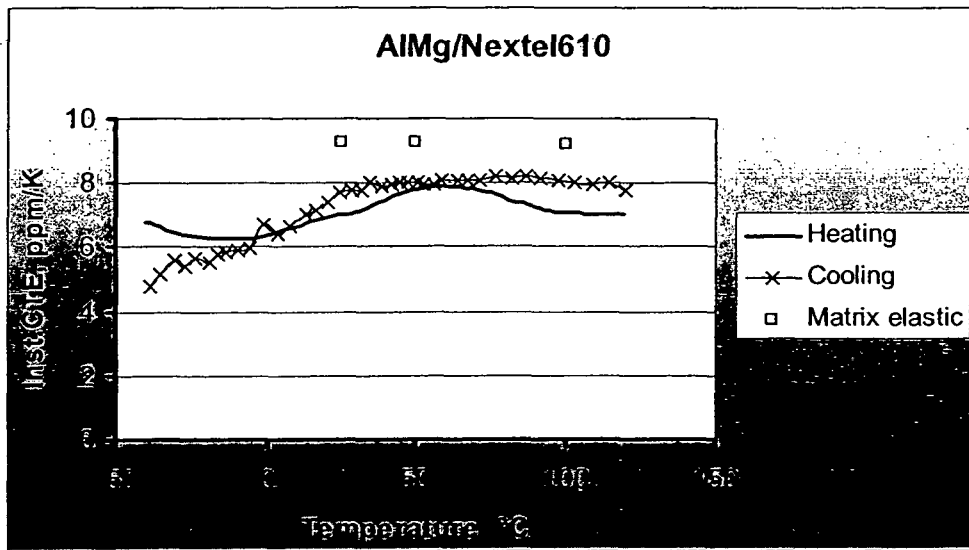


Fig. 5-10, Instantaneous CTE vs. temperature during heating and cooling, and values of CTE calculated by considering elastic matrix according to Schapery.

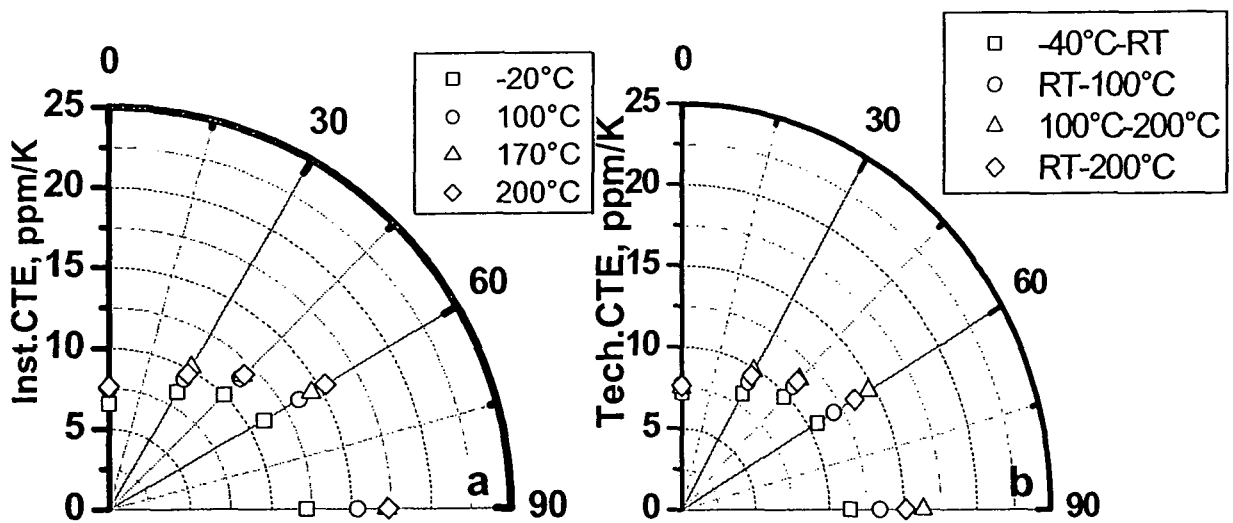


Fig. 5-11, Polar diagram at different temperatures vs. orientation for Al/Nextel610/65f MMC, a) instantaneous CTE and b) technical CTE measured in temperature range from -40°C to 200°C.

5.2. Mg based UD MMCs

5.2.1. MgAl0.6/C-M40B/65f

The strong anisotropy displayed by carbon fiber reinforced magnesium matrix composites MgAl/C-M40B/65f is shown in polar diagrams for E-modulus and strength illustrated in Fig. 5-12 a,b. The rule of mixture calculations of E-modulus based on the values of 45 GPa for the matrix and a high modulus value of 392 GPa for the longitudinal fiber direction and a weak ~ 7 GPa for the transverse direction. Assuming that the initial state of the matrix is already close to the yield stress, further straining in tension deforms the matrix plastically. Accordingly, the hardening modulus of the matrix should be inserted into ROM, which would yield 255 GPa. The theoretical values of the E-modulus calculated from the transformation matrix using the laminator software are based on the longitudinal and transverse values measured by the four point bending test. The deviation of the measured values of E-modulus from the theoretical one at different angles is attributed to the shear stress which was not included in the calculations from the bending test. The longitudinal and transverse values of E-modulus measured by resonant beam, resonant bar and pulsed laser ultrasonic techniques are close to each other because all of them are based on the velocity of sound in the material.

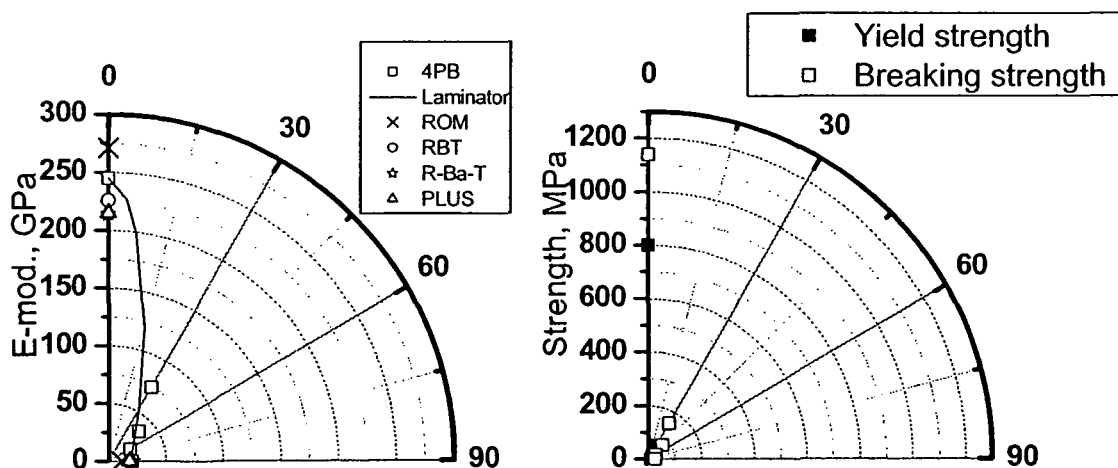


Fig. 5-12, Polar diagrams for MgAl0.6/C-M40B/65f a) Young's modulus measured by different techniques (data calculated by laminator based on the longitudinal and transverse moduli that measured by four point bending test), b) strength vs. orientation.

For the thermal cycling behavior of the carbon fibers reinforced magnesium MMCs, beginning from -40°C , the maximum elastic stress for matrix is estimated to be 50 MPa in tension. Considering Young's modulus of the matrix is 45 GPa, modulus of fibers is 392 GPa with volume fraction of fibers of 0.65 and coefficient of thermal expansion of matrix and composite of 26 and 0.95 ppm/K, respectively, a ΔT of one degree produces a matrix stress of 1.1 MPa using the previously mentioned equation (5.1.1). From the dilatation curve shown in Fig. 5-13, compressive yielding starts at 45°C , with ΔT of 85 K. This gives a stress amplitude in the matrix of 95 MPa. The compressive yield stress of the matrix was measured by using the Gleeble compression test to be approximately 45 MPa. It is well known that magnesium and magnesium alloys have higher yield stress in tension than in compression [68]. The matrix starts with tensile stress of approximately 50 MPa at -40°C , passing through stress free state little above 0°C , followed by compression up to 45MPa, and then yielding starts until the end of the first cycle up to 120°C . During cooling, an elastic range of approximately 95 MPa is assumed again yielding in tension from about 35°C downwards, when strain hardening increases the residual stresses. A negative residual strain of -0.005% is observed at the end of the cooling cycle. Regarding the specimen contraction in fiber direction after the first cycle to a certain temperature range, the following conclusions on the residual stresses can be drawn:

1st cycle -40°C to 120°C , $\Delta L/L_0 = -5 \times 10^{-5}$,

fiber compression $\Delta\sigma_f = -5 \times 10^{-5} \times 392 \times 10^3 \text{ MPa} = -20 \text{ MPa}$,

matrix stress increase $\Delta\sigma_m' = -v_f \Delta\sigma_f / (1-v_f) = 37 \text{ MPa}$.

For the second heating cycle at the same temperature range, the matrix begins in the strain hardened state remaining elastically during the whole temperature range up to 120°C , with very little negative residual strain after cooling compared with the length after the first cycle. We can estimate the stress difference between -40°C and 120°C of the second cycle by multiplying the strain times the fiber modulus to get the stress in fibers of about 63 MPa. Considering the volume

fraction of the matrix 0.35, then the stress change of the matrix is approximately 76 MPa for the whole range (tension and compression of the matrix).

In the high temperature range cycle up to 200°C, the strain hardened matrix behaves elastically from tension to compression until yielding under compression at a temperature of 150°C followed by softening of the matrix at approximately 185°C. Upon cooling, an additional contraction of -8×10^{-5} strain is observed for the CFRM with respect to the length before this cycle indicating an increase in residual stresses. In the following cycle no softening is observed.

The residual stresses could be estimated in this temperature range from -40°C to 200°C as, fiber compression $\Delta\sigma_f = -8 \times 10^{-5} \times 392 \times 10^3 \text{ MPa} = -31 \text{ MPa}$,

matrix stress increase $\Delta\sigma_m'' = -v_f \Delta\sigma_f / (1-v_f) = 57 \text{ MPa}$.

With assumption of an initial residual stress of 50 MPa, the first cycle to 120°C adds ca. 37 MPa and the third cycle to 200°C further 57 MPa, summing up to 144 MPa residual longitudinal stresses in the matrix. This stress value seems to be very high for the MgAl0.6 alloy which may produce strain hardening between 100 and 200 MPa [69].

Concluding from dilatation measurements with holding time at RT, the elastic straining of the constituent is relaxing. Therefore the starting point of the dilatation cycle becomes the same according to a relaxed residual stress situation for all specimens.

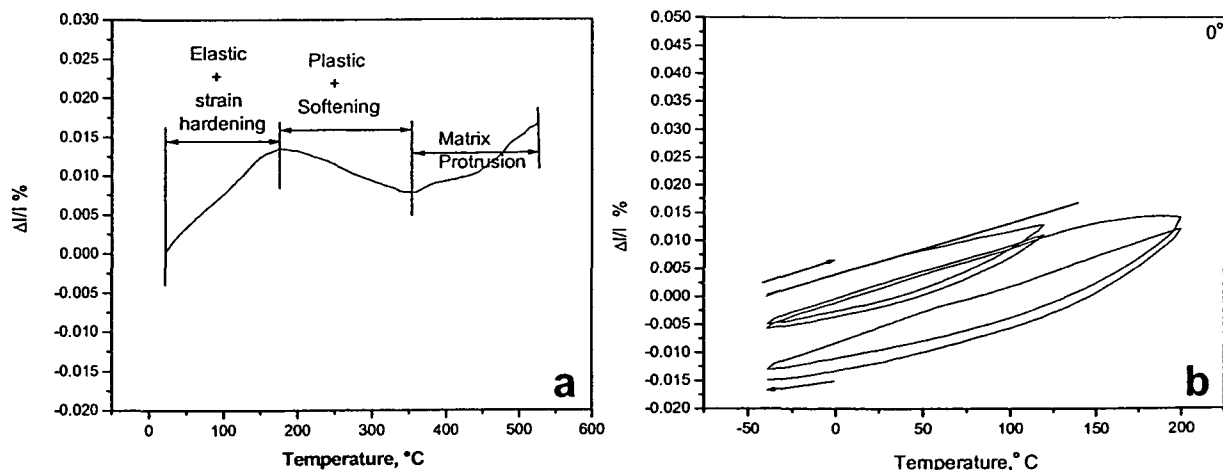


Fig. 5-13, Dilatation curve for MgAl0.6/C-M40B/65f UD, a) from room temperature up to 525°C, and b) thermal cycling from -40°C to 200°C.

The behavior for the second cycle in the same temperature range is again elastic up to about 150°C followed by plastification and relaxation as before. It cools down with the same behavior like the first cycle with negligible additional residual strain. A schematic diagram shows the MgAl_{0.6} longitudinal matrix stress in case of MgAl_{0.6}/C-M40B MMCs with temperature in Fig.5-14.

With deviation from the fiber axis, at 30° inclination, the effect of fibers on matrix is decreasing and the behavior of the whole composite is approximately linear, specially for the low temperature range cycles (Fig. 4-15b-e). A hysteresis is only observed for the cycles at the high temperature range due to the tensile straining of the matrix in the cooling down part. Increasing the inclination more than 30°, the behavior tends to exhibit decreasing CTE in the tensile strain range of the matrix with decreasing temperature.

From the stress strain curves produced by compression test for the matrix, the stress strain relation of the matrix is approximated by two different hardening moduli at each temperature. The moduli used for the calculations of the CTE according to modified model produced by Böhm, for the range of plastic matrix deformation and in the elastic state $E(T)$ according to Schapery's model. Fig.5-15 shows the instantaneous CTE with thermal cycling and the agreement of the calculated CTE value and the model of Schapery using $E(T)$ for the elastic range, E_h for the strain hardening range of the matrix which is approximated to zero, i.e. ideally plastic extreme case (for data see Table 4.9).

A polar diagram showing the instantaneous and technical CTE for carbon fibers reinforced MgAl_{0.6} at different temperatures against fiber orientation is illustrated in Fig.5-16a,b. They are very close to each other except the scatter of the technical CTE at 30° inclination.

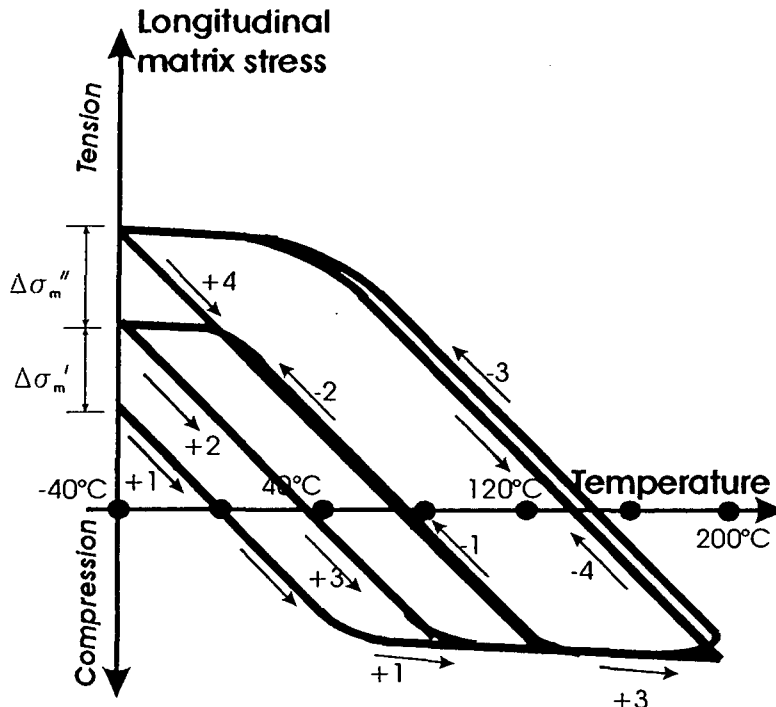


Fig. 5-14, Schematic estimation of longitudinal matrix stresses during thermal cycling, two cycles in the temperature range from -40°C to 120°C (± 1 , ± 2), and two cycles from -40°C to 200°C (± 3 , ± 4) for MgAl0.6/C-M40B/65f UD.

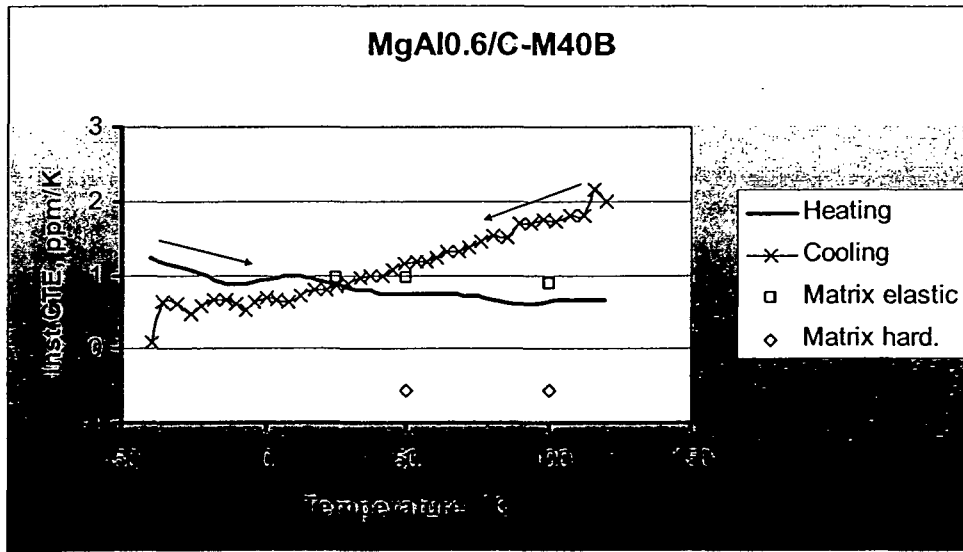


Fig. 5-15, Instantaneous CTE vs. temperature for MgAl0.6/C-M40B/65f during heating and cooling, and values of CTE calculated by considering elastic matrix according to Schapery and plastic matrix according to Böhm.

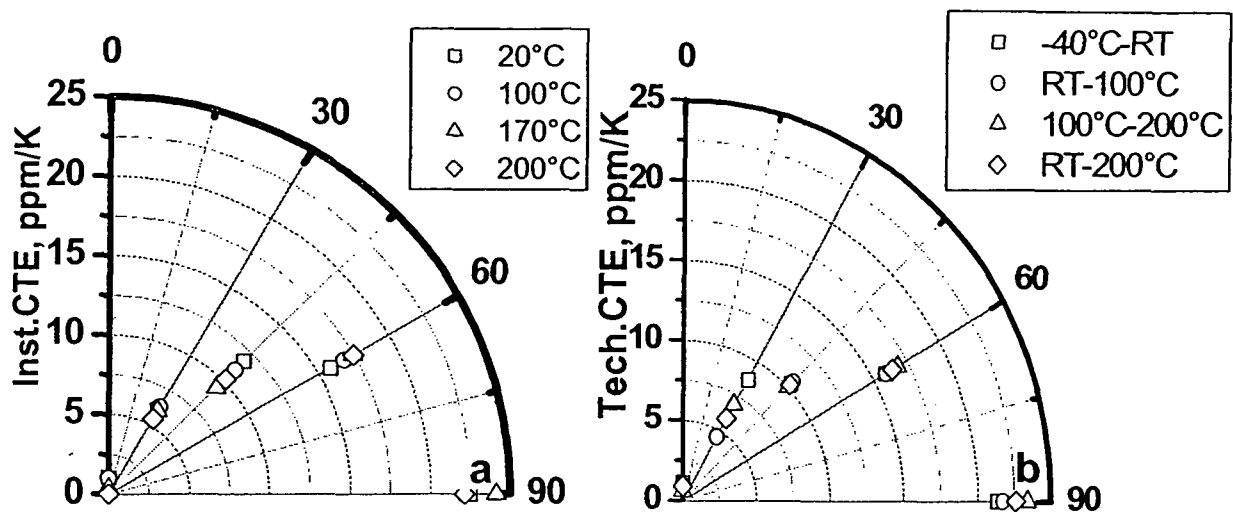


Fig. 5-16, Polar diagram at different temperatures vs. orientation for MgAl_{0.6}/C- M40/65f, a) instantaneous CTE and b) technical CTE measured in temperature range from -40°C to 200°C.

5.2.2. Mg/C-Tenax HTA 5331/55f

The tenax fiber is one of the high strength low modulus carbon fiber types which has highly anisotropic properties. The polar diagrams in Fig.5-17 a,b show the relation between fiber orientation and both E-modulus and fracture strength, respectively. The experimental four point bending test value would correspond to a computational efficiency of 0.8 for the fiber modulus applied to the linear ROM. This may be due to the lack of straightness of the fibers or due to the matrix veins in between fibers, this also explains the high scatter of ± 20 GPa between tested specimens as shown in table 4-3. Assuming the matrix being strained to yield stress already before bending, the matrix deforms plastically along the tension side. Inserting the hardening modulus of the matrix into ROM yields $E = 130$ GPa. The same analysis like in MgAl_{0.6}/C-M40B for the thermal dilatation curves could be done on the commercially pure magnesium reinforced by Tenax carbon fibers. A small difference in values comparing the high modulus carbon fibers can be observed due to the type of carbon fibers used and

the smaller volume fraction which is 55% in this case, as well as the pure Mg matrix. This is the reason for the drop of temperature of the elastic strain limit from 45°C to 10°C which is illustrated in Fig.5-18 comparing with MgAl_{0.6}/C-M40B/65f. Assuming the yield stress of the matrix at low temperature being ca. 40 MPa in tension and ca. 30 MPa in compression [68], using equation (5.1.1) and considering the coefficient of thermal expansion of composite is 3.6 ppm/K, the matrix stress is calculated to be 1 MPa for one degree temperature difference. The matrix stress range of 70 MPa corresponds to a temperature change of 70 K with a sign change at about 40 K, i.e. at 0°C. Compressive yielding would start around +30°C followed by strain hardening overlapping with reduction of yield stress owing to the increasing temperature up to 120°C. Reducing the temperature, the elastic range may be about 70 MPa again, which requires a temperature change of about 70 K. Tensile yielding would start in tension at about 50°C.

During further cooling to -40°C strain hardening takes place reaching a somewhat higher internal stress state than in the beginning of the first cycle, which causes some contraction of the CFRM sample. The subsequent dilatation in heating follows the same pattern as in the previous cycle up to 120°C. After some strain hardening, softening starts at 150°C due to relaxation and reduction of yield stress.

At 200°C we assume a residual stress of about 25 MPa (see Fig. 4-48b) which will be relieved during cooling and converted into a tensile stress up to about 35 MPa. This change in stress of about 60 MPa corresponds to a reduction in temperature of about 60 K. From 140°C downwards the matrix is again plastically deformed providing significant strain hardening which increases the mismatch stresses (> 30 MPa) producing a significant contraction of the CFRM.

The residual stresses after cooling in the third temperature cycle from -40°C to 200°C could be estimated as,

fiber compression $\Delta\sigma_f = -1.5 \times 10^{-4} \times 237 \times 10^3 \text{ MPa} = -35 \text{ MPa}$,

matrix stress increase $\Delta\sigma_m'' = -\Delta\sigma_f / (1 - v_f) = 43 \text{ MPa}$.

With assumption of an initial residual stress of 40 MPa, the total longitudinal matrix stress at the end of the third cycle is 83 MPa. The following dilatometric cycle to 200°C repeats this elastoplastic deformation scheme without further changes.

A schematic diagram shows the longitudinal matrix stress in case of Mg/C-Tenax MMC behavior with temperature in the longitudinal direction constructed in Fig.5-19. The CTE level changes from the elastic level during heating to the matrix plastifying whereas it starts at the elastic level during cooling becoming plastic during heating (see Fig.5-20).

The value of CTE obtained from the experimental result is in a good agreement with the Schapery's model as shown in Fig. 5-20. Different E-moduli of table 4-9 were used for application of Böhm's modified model. The dependence of CTE on temperature and orientation is illustrated in polar diagram in Fig. 5-21. There is little difference between the instantaneous and technical CTE values.

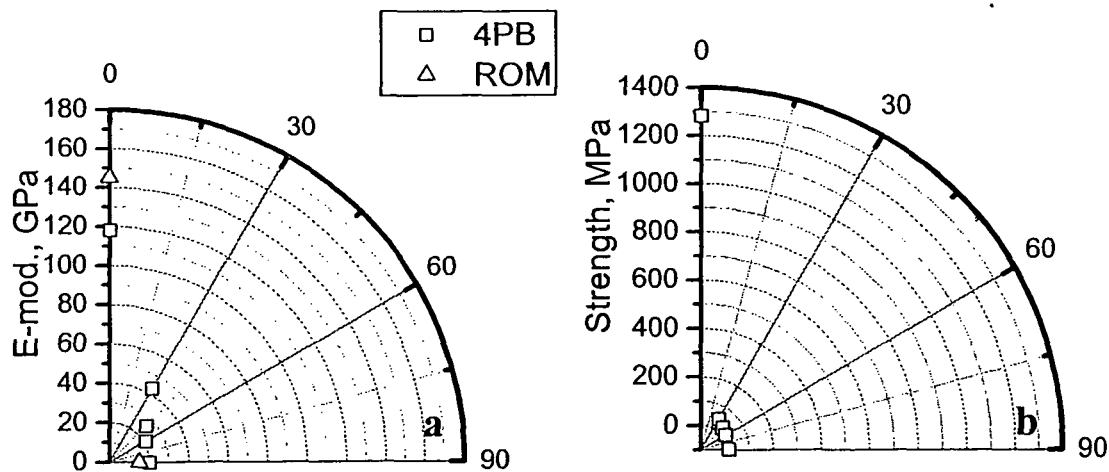


Fig. 5-17, Polar diagrams for a) Young's modulus measured by four point bending and estimated by ROM, b) breaking strength vs. orientation for Mg/C-Tenax/55f MMC.

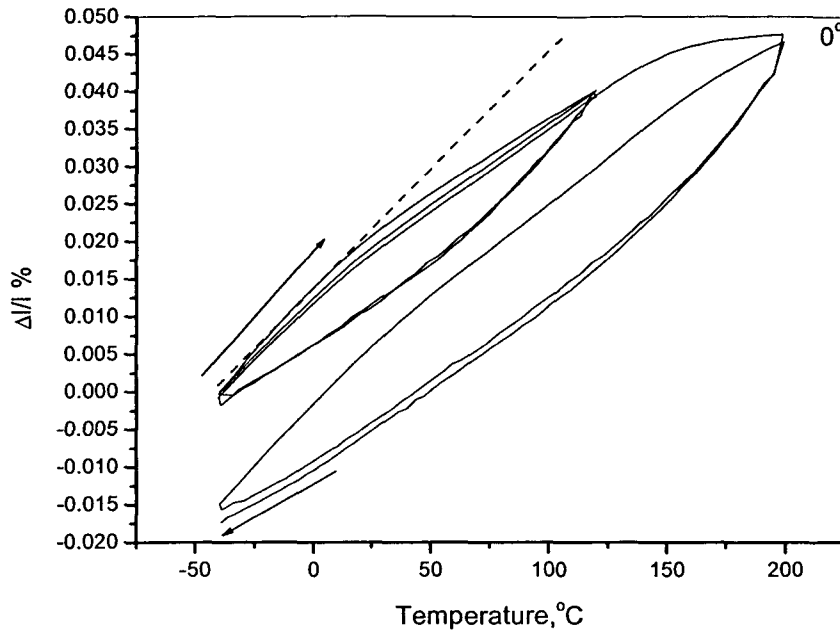


Fig. 5-18, Dilatation curve for Mg/C-Tenax/55f UD MMC in the longitudinal direction.

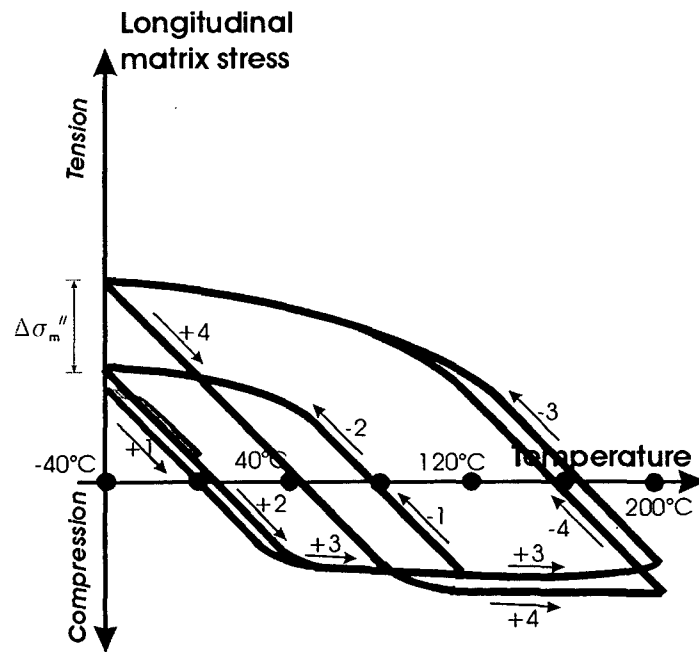


Fig. 5-19, Schematic estimation of longitudinal matrix stresses during thermal cycling, two cycles in the temperature range from -40°C to 120°C (± 1 , ± 2), and two cycles from -40°C to 200°C (± 3 , ± 4) for Mg/C-Tenax/55f.

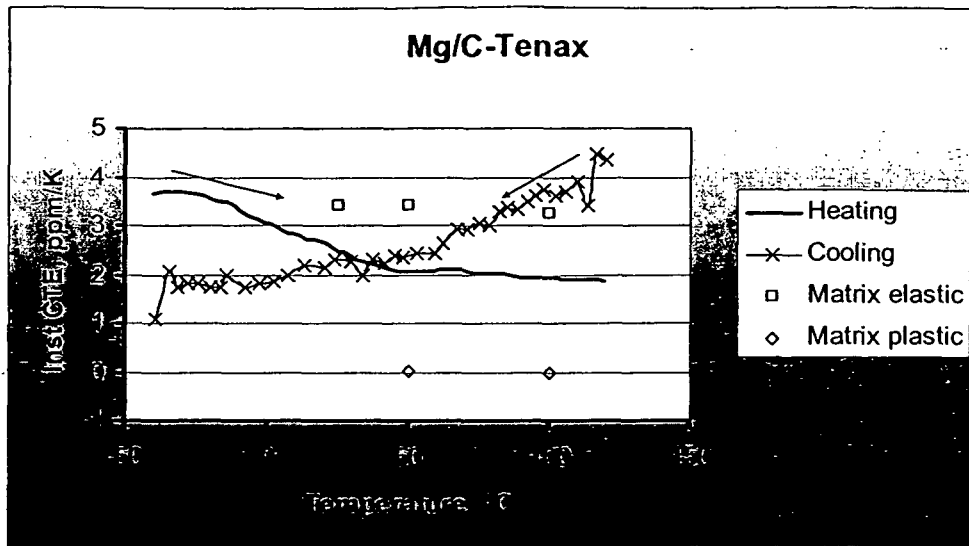


Fig. 5-20, Instantaneous CTE vs. temperature for Mg/C-Tenax/55f during heating and cooling, and values of CTE calculated by considering elastic matrix according to Schapery and matrix plastic according to Böhm.

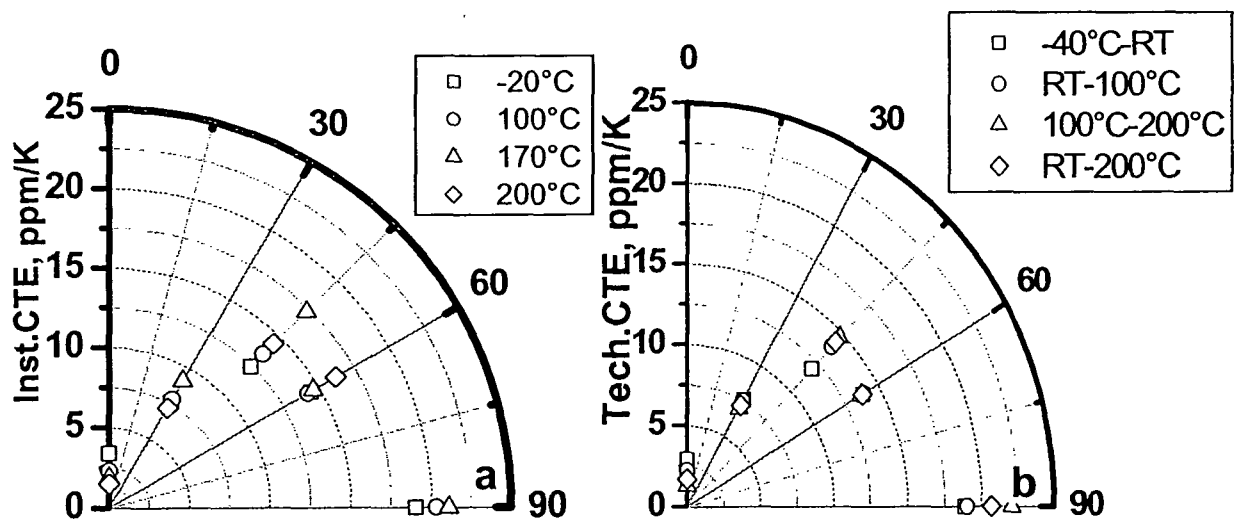


Fig.5-21, Polar diagram at different temperatures vs. orientation for Mg/C-Tenax/55f, a) instantaneous CTE and b) technical CTE measured in temperature range from -40°C to 200°C.

5.3. 6 Layered UD and woven fiber reinforcement

The layered UD material consists of 6 unidirectional layers of Al/C-M40B, with orientations of $0,+60,-60,-60,+60,0^\circ$. One of the main advantages of this symmetric angle ply material is that bending-stretching coupling will not be present in such laminates. But, on the other hand, the main disadvantage is the production difficulty which appeared in the microstructural cross-section shown in Fig.4-3a. The thin aluminium layers between plies weaken the material. An important assumption in the lamination theory is that the layers have a perfect bonding, so that no slip occurs at ply interfaces. For this reason, there is some deviation between the experimental and theoretical values for flexural modulus in the longitudinal direction. These calculations based on the data of the UD MMC material discussed in section 5.1.1 using the laminator software. Both, flexural modulus and strength values depend on the outer layer, this can be seen obviously in polar diagram in Fig. 5-22 a,b.

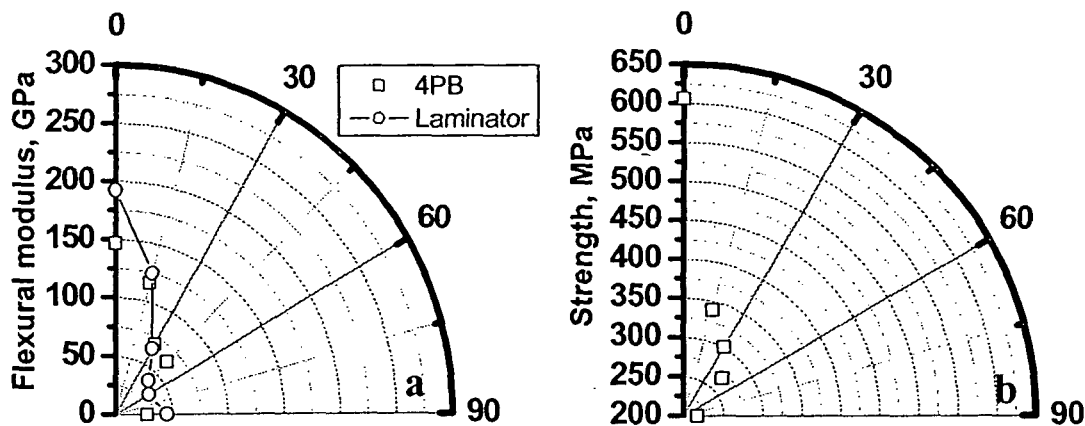


Fig. 5-22, Polar diagrams for a) flexural modulus measured by four point bending and estimated by laminator software, b) breaking strength vs. orientation for 6 layers symmetric MMC.

These materials are designed to provide isotropy, the thermal behavior of such material should be equivalent in all directions. A lower CTE value is measured in the direction where the stacking includes two layers in fiber direction and a higher CTE value in the direction where two layers in the transverse direction were included as shown in the polar diagram in Fig. 5-23. The dilatation curves as well as the stress behavior are comparable to the Al/C-UD system.

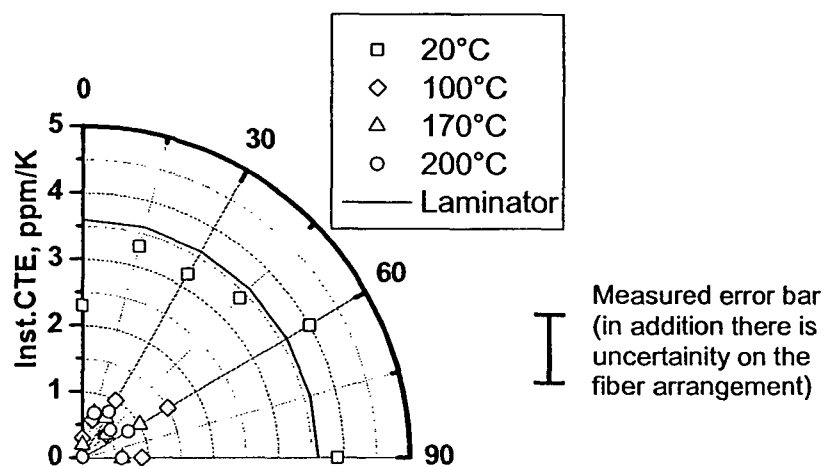


Fig.5-23, Polar diagram for instantaneous CTE at different temperatures vs. orientation for the 6 layers symmetric MMC.

For the woven carbon fiber reinforced magnesium, if the volume fraction of fibers in the warp and fill directions were equal, the CTE values are approximately the same for all directions with a higher CTE value in the 45° direction as shown in polar diagram in Fig. 5-24a. If the volume fraction of fibers in the warp direction is 80% and in the fill direction is only 20%, the lower CTE value is in the direction of more fibers and the lowest in the perpendicular direction as shown in Fig. 5-24b. For theoretical estimation of CTE, the fiber volume fractions for different woven systems were calculated with respect to the total matrix volume fraction, then the transverse CTE was calculated using the transverse Schapery's model equation (2.5.4) and considered as a matrix for the desired direction. The results for CTE values are illustrated in Fig. 5-24 a-c for different woven systems.

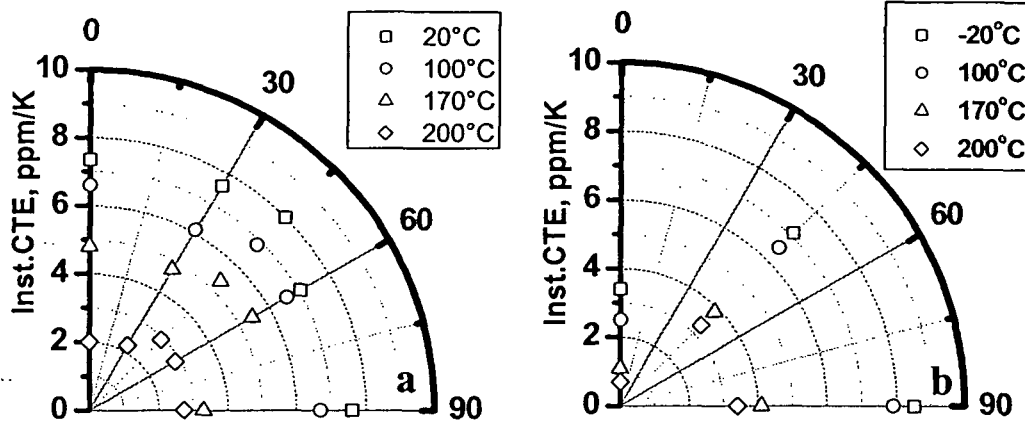


Fig.5-24, Polar diagram for instantaneous CTE at different temperatures vs. orientation for a) woven 50/50 and b) woven 80/20 MMC.

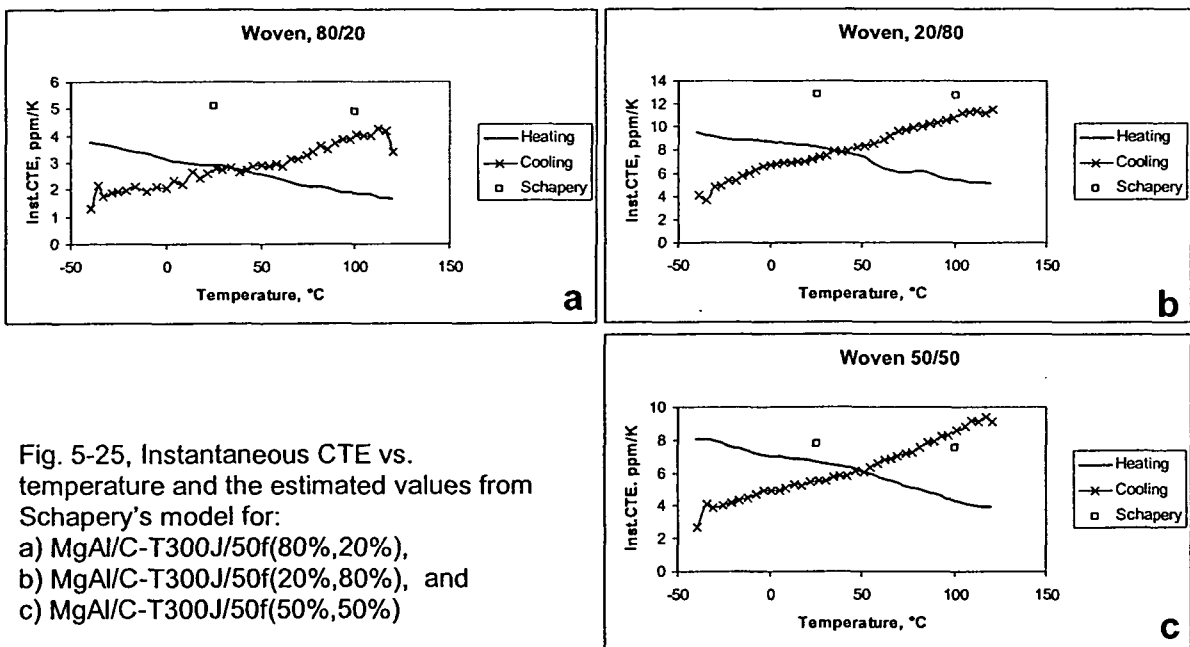


Fig. 5-25, Instantaneous CTE vs. temperature and the estimated values from Schapery's model for:
 a) MgAl/C-T300J/50f(80%,20%),
 b) MgAl/C-T300J/50f(20%,80%), and
 c) MgAl/C-T300J/50f(50%,50%)

5.4. Volumetric change calculations

The volume changes under thermal cycling were calculated using the linear thermal dilatation curves of UD-CFRM in both longitudinal and transverse directions for thermal cycles. Assuming independent deformation of the constituents, the volumetric change for both fibers and matrix is summed disregarding any coupling. The temperature dependence of a volume is given by

$$V(T) = V_0 + \Delta V(T) = V_0 (1 + \alpha_l \Delta T) (1 + \alpha_t \Delta T)^2$$

$$\Delta V / V_0 = (\alpha_l + 2 \alpha_t) \Delta T \quad \text{when } \alpha_l \neq \alpha_t, \text{ and}$$

$$\Delta V / V_0 = 3 \alpha \Delta T \quad \text{when } \alpha_l = \alpha_t = \alpha$$

$$\Delta V / V_{\text{CFRM}}^* = v_f (2 \alpha_{f,t} \Delta T + \alpha_{f,l} \Delta T) + (1 - v_f) (3 \alpha_m \Delta T) \quad (5.4.1)$$

where V , v , α and ΔT stand for volume, volume fraction, CTE and temperature change, respectively, and the subscripts l , t , f and m stand for longitudinal, transverse, fibers and matrix, respectively. Equation (5.4.1) gives an upper estimation of the thermal expansion of a CFRM volume:

$$\Delta V / V_{\text{CFRM}} (\text{real}) \leq \Delta V / V_{\text{CFRM}}^*$$

The experimentally determined longitudinal $\Delta l / l_0 (\Delta T)_l$ and transverse $\Delta l / l_0 (\Delta T)_t$ linear expansions are used to calculate the volume expansion of the CFRM by

$$\Delta V / V_{\text{CFRM}} (\text{experimental}) = \Delta l / l_0 (\Delta T)_l + 2 \Delta l / l_0 (\Delta T)_t \quad (5.4.2)$$

In the following the thermal expansion during the first cycle of the higher temperature range (-40 to 200°C) is taken, because it shows the biggest strain difference with respect to the following reproducible cycles.

Considering the constituents to expand freely, in the transverse direction, but to be subjected to an isostrain condition in the longitudinal direction represented

by the experimental result, which is assumed to be achievable by purely elastic straining ($\varepsilon^{\text{elast}}$), the elastic strain in the constituents can be calculated separately by

$$\varepsilon_m^{\text{elast}} = \Delta l/l_0 (\Delta T)_l - \alpha_m \Delta T \quad (5.4.3a)$$

$$\varepsilon_f^{\text{elast}} = \Delta l/l_0 (\Delta T)_l - \alpha_{f,l} \Delta T \quad (5.4.3b)$$

Elastic straining causes a change in volume owing to the Poisson's ratio (ν) being different from 0.5. The resulting volume change of the constituents is the bigger the smaller the ν value and is given by

$$\Delta V/V_m^{\text{elast}} = (1-2\nu_m) \varepsilon_m^{\text{elast}} \quad (5.4.4a)$$

$$\Delta V/V_f^{\text{elast}} = (1-2\nu_f) \varepsilon_{f,l}^{\text{elast}} \quad (5.4.4b)$$

The volume change for the CFRM is given by

$$\Delta V/V_{\text{CFRM},l}^{\text{elast}} = v_f \cdot \Delta V/V_f^{\text{elast}} + (1-v_f) \cdot \Delta V/V_m^{\text{elast}} \quad (5.4.4c)$$

Inserting the values for AlMg1/Nextel 610/65f, the volume change of the free constituents is calculated using equation (5.4.1), considering the volume fraction of the fibers is 65%, CTE of the matrix and fibers are 23 and 7.9 ppm/K, respectively, and temperature change of 150 K, this gives a volumetric change of 0.6%.

The elastic volume change for the matrix is calculated from

$$\Delta V/V_m^{\text{elast}} = (1-2\nu_m) [\Delta l/l_0 (\Delta T)_l - \alpha_m \Delta T]$$

Considering for matrix the following, $\nu = 0.3$, $\alpha_m = 23$ ppm/K, $\Delta l/l_0$ between 50°C and 200°C ($\Delta T = 150$ K) = 12.5×10^{-4} (see Fig.5-8c), yielding $\Delta V/V_m^{\text{elast}} = -0.88 \times 10^{-3}$ due to compression.

Considering Nextel610 fibers, $\nu = 0.2$, $\alpha_f = 7.9$ ppm/K, $\Delta l/l_0$ the same as for the matrix, then from equation (5.4.3b), $\Delta V/V^{\text{elast.}_f} = 0.03 \times 10^{-3}$ due to tension.

Then $\Delta V/V^{\text{elast.}_{CFRM,I}} = 0.65 (0.03 \times 10^{-3}) + 0.35 (-0.88 \times 10^{-3}) = -0.3 \times 10^{-3}$

Fig. 5-26 shows five different calculated lines for easier comparison between different cases illustrating the pure aluminium matrix behavior (i.e. 35 vol. %), the isostrain condition, free constituent of the composite calculated from eq. (5.4.1), isostrain of the composite from eq. (5.4.4c), free fiber behavior, and the isostrain of the fiber (65%) behavior. The lines are intersected at 50°C just for better illustration. The experimental volume change as well as the free independent constituents and the isostrain lines for AlMg1/Nextel610/65f are shown in Fig. 5-27, the elastic limits as well as the zero residual stress temperatures are shown with vertical lines at temperatures based on the schematic axial stress-temperature diagram (Fig. 5-9). The elastic volume change of the matrix is dominating.

The calculated estimations of the temperature dependence of $\Delta V/V$ are presented in the corresponding figures by a straight lines for the free expansion of the constituents as well as the isostrain of composite passing through the temperature where the residual stresses are zero during heating. The relative increase in the experimental volume change in the temperature lower than 50°C may be explained by pore opening or formation during cooling within the same temperature range of plastic matrix deformation. The difference to the isostrain line amounts to about 0.5×10^{-3} in volume at -40°C which would represent the pore volume portion created during cooling.

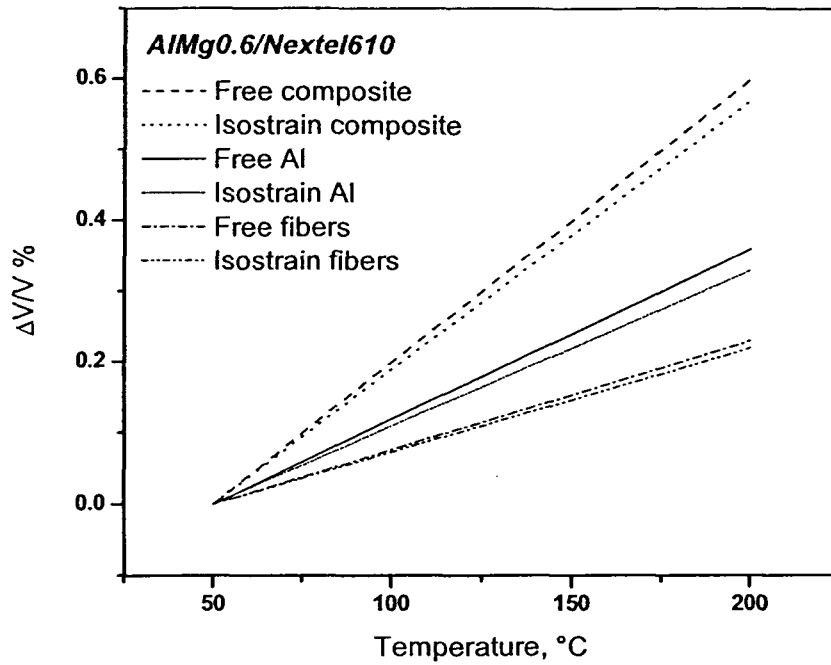


Fig.5-26, Volume change vs. temperature calculated for 35 vol % pure Al, Al/Nextel610/65f CFRM and 65% Nextel fibers with free expansion and isostrain conditions for the constituents as calculated.

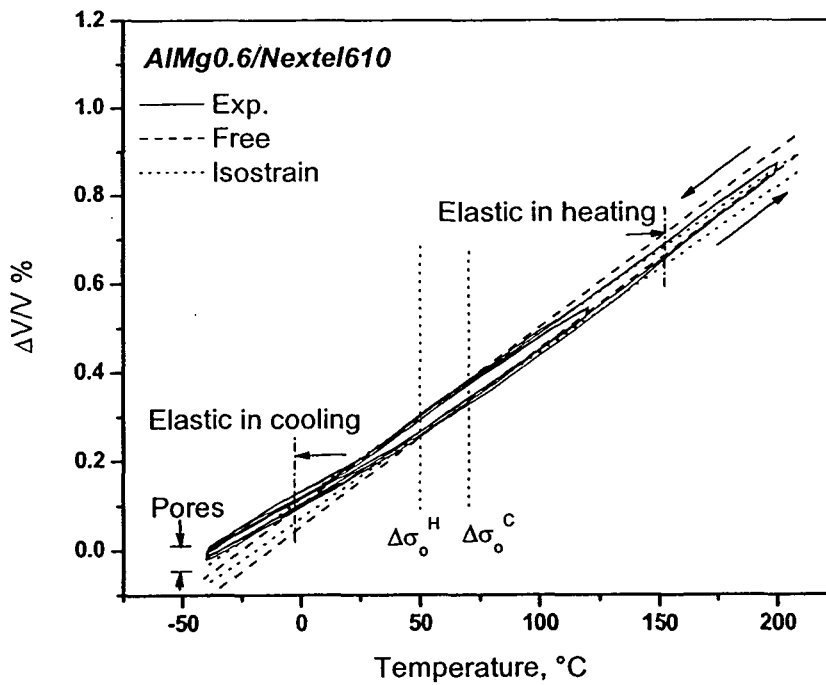


Fig.5-27, Volume change vs. temperature calculated from dilatation curves for Al/Nextel610/65f with free expansion and isostrain condition for the constituents as calculated, $\Delta\sigma_o^H$ and $\Delta\sigma_o^C$ represent the zero matrix stress upon heating and cooling, respectively, taking from Fig. 5-9.

For the Al/C-M40B MMC, the volume fraction of the fibers is 65%, CTE of the matrix and fibers in the longitudinal and transverse directions are 23, -0.6, and 17 ppm/K, respectively, a temperature change of 150 K, from equation (5.4.1) causes a volume change of 0.7%.

Considering for matrix the following, $\nu = 0.3$, $\alpha_m = 23$ ppm/K, $\Delta l/l_0$ between 50°C and 200°C ($\Delta T = 150$ K) = 0.4×10^{-4} (see Fig. 5-2b), yielding $\Delta V/V^{\text{elast.}}_m = -0.5 \times 10^{-3}$. Considering M40 carbon fibers, assuming $\nu = 0.2$, $\alpha_{f,l} = -0.6$ ppm/K, $\alpha_{f,t} = 17$ ppm/K, and $\Delta l/l_0$ the same as for the matrix, then from equation (5.4.4b), $\Delta V/V^{\text{elast.}}_f = 0.7 \times 10^{-4}$, which is one magnitude lower than the value of the volume change of the matrix and can be neglected. Testing the sensitivity of these estimations, it turns out that neither scatters in volume fraction nor in the longitudinal CTE of the fibers are of great influence, but the uncertainty in the transverse CTE of the C-fibers contributes considerably.

The experimental volume change for the 3rd temperature cycle as well as the estimation for free independent constituents and the isostrain lines for Al/C-M40B/65f are shown in Fig. 5-28. The calculated lines pass through the point where the residual stress of matrix is zero during heating and cooling according to schematic diagram shown in Fig. 5-4. The volumetric CTE for the same CFRM during heating and cooling was calculated using the experimentally measured linear CTE values in longitudinal and transverse directions by summing the longitudinal value of CTE and double of the transverse value. The free and isostrain lines were calculated using the same CTE values as the volume calculations. Experimental and calculated lines as well as the elastic limits during heating and cooling according to the schematic diagram for the longitudinal matrix stress (Fig. 5-4) are shown in Fig. 5-29. The relative increase in the experimental volume change in the temperature lower than approximately 30°C and higher than approximately 100°C may be explained by pore opening and closing up to 10^{-3} in volume from the free constituents' line at -40°C which would represent the pore volume portion created during cooling.

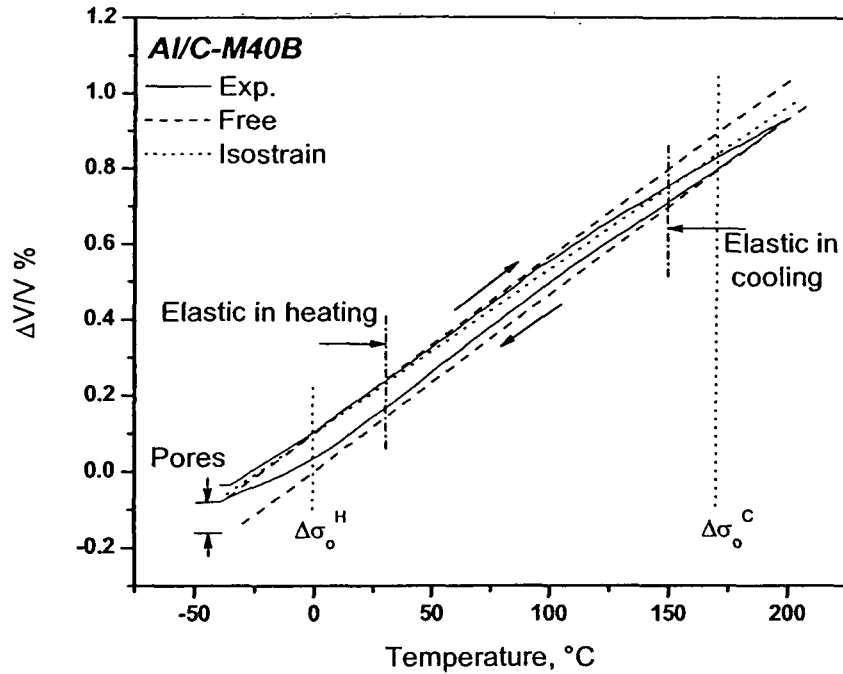


Fig.5-28, Volume change vs. temperature calculated from the 3rd thermal cycle for Al/C-M40B/65f with free expansion and isostrain condition for the constituents as calculated, $\Delta\sigma_o^H$ and $\Delta\sigma_o^C$ represent the zero matrix stress upon heating and cooling, respectively, taking from Fig. 5-4.

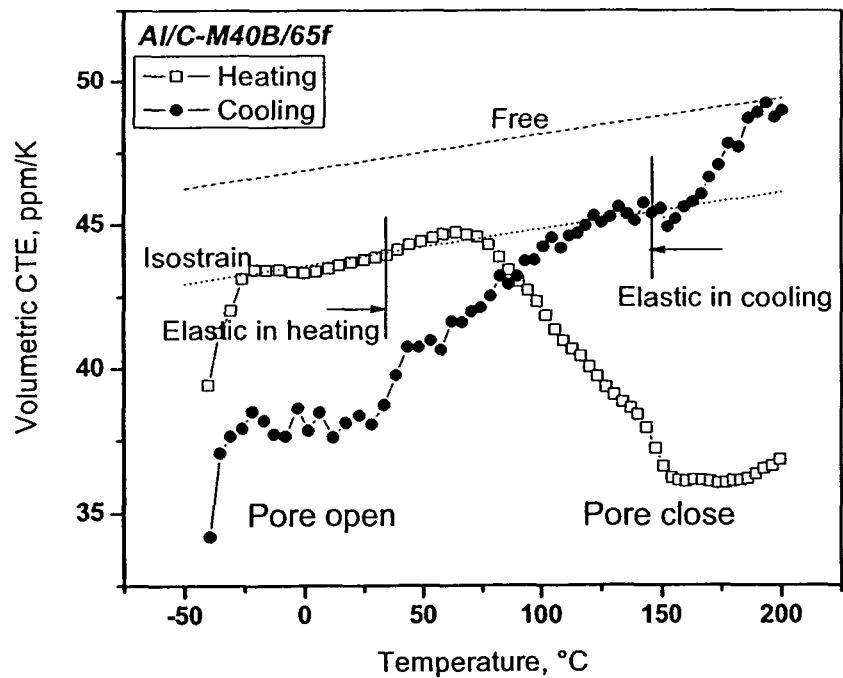


Fig.5-29, Volumetric CTE vs. temperature calculated from longitudinal and transverse CTE curves for Al/C-M40B/65f with free expansion and isostrain condition for the constituents as calculated, the elastic limits in heating and cooling are taken from the 3rd thermal cycle in the schematic diagram in Fig. 5-4.

For the MgAl0.6/C-M40B MMC, the volume fraction of the fibers is 65%, CTE of the matrix and fibers in the longitudinal and transverse directions are 26, -0.6, and 17 ppm/K, respectively, and temperature change of 150 K, from equation (5.4.1) the volume change is 0.75%.

For the matrix, $\nu = 0.3$, $\alpha_m = 26$ ppm/K, $\Delta l/l_0$ between 50°C and 200°C ($\Delta T = 150$ K) = 1.0×10^{-4} (see Fig. 5-13b), yields $\Delta V/V^{\text{elast.}}_m = -0.53 \times 10^{-3}$. The experimental volume change for the 3rd thermal cycle as well as the free independent constituents and the isostrain lines for MgAl0.6/C-M40B/65f are shown in Fig. 5-30. The calculated lines pass through the point where the residual stress of the matrix is zero during heating and cooling according to schematic diagram shown in Fig. 5-14. The relative increase in the experimental volume change in the temperature lower than approximately 80°C may be explained by pore opening or formation during cooling within the temperature range of plastic matrix deformation, which may reach more than 10^{-3} volume portion at -40°C.

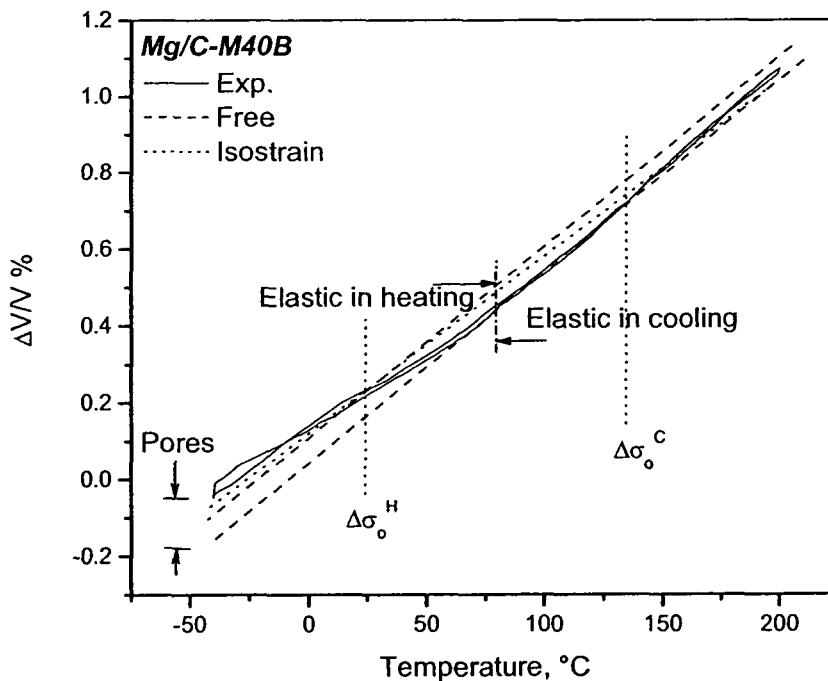


Fig.5-30, Volume change vs. temperature calculated from the 3rd thermal cycle for MgAl/C-M40B/65f with free expansion and isostrain condition for the constituents as calculated, $\Delta\sigma_0^H$ and $\Delta\sigma_0^C$ represent the zero matrix stress upon heating and cooling, respectively, taking from Fig. 5-14.

For the Mg/C-Tenax MMC, the volume fraction of the fibers is 55%, CTE of the matrix and fibers in the longitudinal and transverse directions are 26, -0.1, and 10 ppm/K, respectively, and temperature change of 150 K, from equation (5.4.1) the volume change is 0.7%.

For the matrix, $\nu = 0.3$, $\alpha_m = 26$ ppm/K, $\Delta l/l_0$ between 50°C and 200°C ($\Delta T = 150$ K) $= 2.0 \times 10^{-4}$ (see Fig.5-18), yields $\Delta V/V^{\text{elast.}_m} = -0.67 \times 10^{-3}$. The experimental volume change as well as the free independent constituents and the isostrain lines for Mg/C-Tenax/55f are shown in Fig. 5-31. The calculated lines pass through the point where the residual stress is zero either during heating or cooling according to schematic diagram shown in Fig. 5-19. Fig. 5-32 shows the experimental volumetric CTE as well as the free and isostrain lines intersected in the point where the yielding of the matrix begins during heating. The volumetric CTE for heating and cooling follow the isostrain line in the range from 0°C to 125°C. Below 0°C, the relative decrease in the volumetric CTE in Fig. 5-32 may be explained by pore opening or formation during cooling which is not evident in Fig. 5-31. The increasing volume and volumetric CTE higher than 125°C may be explained by reduction of stresses according to transverse creep (relaxation).

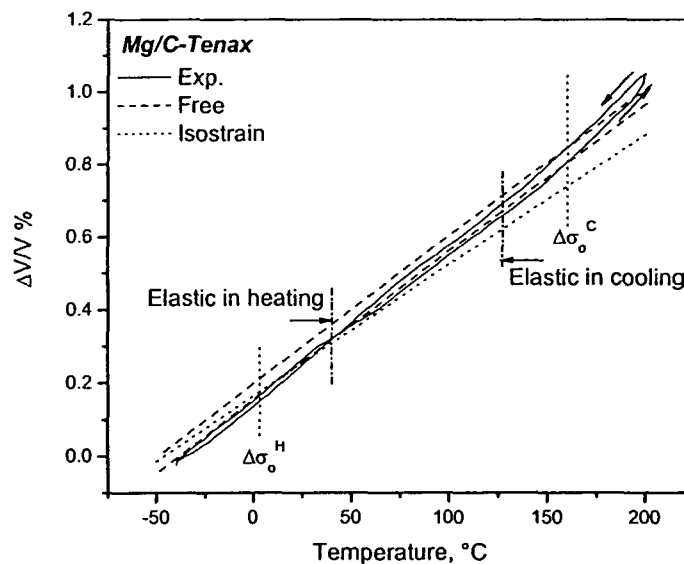


Fig.5-31, Volume change vs. temperature calculated from the 3rd thermal cycle for Mg/C-Tenax/55f with free expansion and isostrain condition for the constituents as calculated, $\Delta\sigma_0^H$ and $\Delta\sigma_0^C$ represent the zero matrix stress upon heating and cooling, respectively, taking from Fig. 5-19.

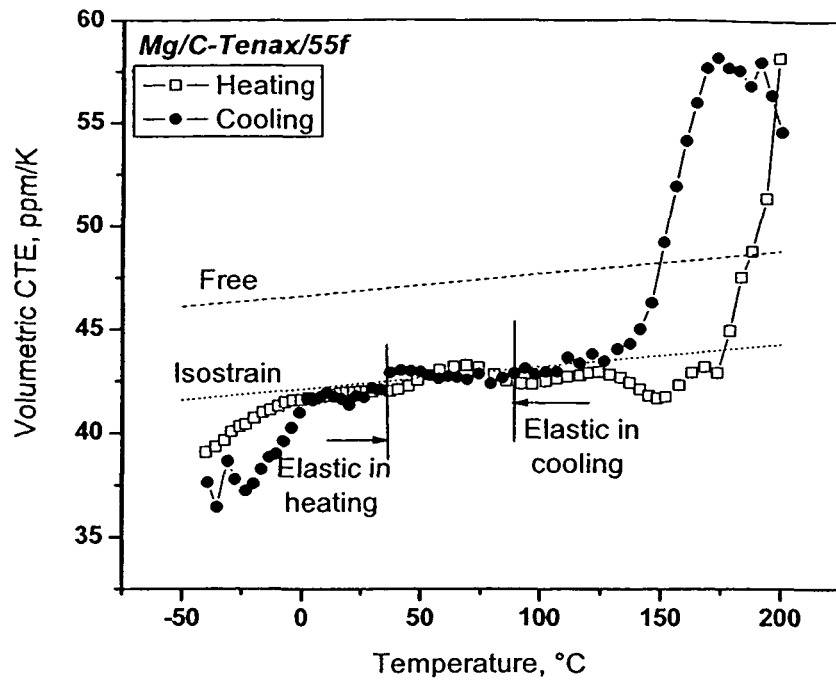


Fig.5-32, Volumetric CTE vs. temperature calculated from longitudinal and transverse CTE curves for Mg/C-Tenax/55f with free expansion and isostrain condition for the constituents as calculated, the elastic limits in heating and cooling are taken from the 3rd thermal cycle in Fig 5-19.

5.5. Comparison

Aluminium has a FCC crystal structure, while magnesium has HCP crystal structure, for this reason aluminium is more ductile than magnesium. According to literature [68], formability of Mg starts only above 120°C. This can be seen obviously during heating for both materials in the temperature range from room temperature up to 525°C, plastification in pure aluminium when reinforced by carbon fibers starts at approximately 60°C ($\Delta T = 40$ K from room temperature) corresponding to +5°C ($\Delta T = 45$ K) in the thermal cycling with lower bound of -40°C, while for magnesium reinforced with the same fiber type starts at 120°C ($\Delta T = 100$ K) corresponding to -45°C ($\Delta T = 85$ K) in thermal cycling from -40°C.

Comparing the zero strain gleeble test (Fig.4-49) on aluminium indicates yielding at 75°C which corresponds to a $\Delta T = 50$ K (starting temperature in Gleeble is 25°C).

Addition of magnesium to aluminium increases the yield strength of the matrix by solid solution strengthening, this can be seen in the AlMg1/Nextel MMC and MgAl0.6/C-M40B.

The behavior of magnesium and magnesium alloys is non-symmetric in tensile and compressive strength, they have a higher tensile than compressive strength, which is the reason for the different plastification level of Mg in heating (compression) and cooling (tension).

Due to the negative CTE of carbon fibers in the axial direction a very low longitudinal coefficient of thermal expansion is obtained for CFRM. A CTE value of approximately zero in the temperature range from room temperature up to 200°C was found for the carbon fiber reinforced aluminium, while a value of 1 ppm/K was obtained in case of magnesium matrix because of an extended elastic behavior. Perpendicular to the fiber direction, CTE values for UD CFRM are close to the values of CTE of the matrix, in the case of planar textile reinforcement the out of plane CTE of the CFRM is much bigger than that of the matrix compensating the planar constraints by the fiber arrangement.

When the composite is subjected to a change in temperature, the differences in coefficient of thermal expansion of the constituents will produce an internal strain mismatch causing the thermally induced stresses. If the strain mismatch is small, it is generally accommodated elastically, this can be seen in the Al/Nextel MMC. On the other hand, for the larger CTE mismatch, the entire deformable volume of the matrix of a MMC may become plastically deformed, as in the Al/C CFRM. The yield strength of the matrix under the constrained conditions between the fibers determines the beginning of plastic deformation during thermal cycling. The yielding of AlMg/Nextel and of MgAl/C-M40B starts at larger thermal mismatch values than pure Al. Taking the temperature of elastic straining, the following mismatch strains can be correlated with the yield strength levels of the matrix as

AlMg/Nextel	$\Delta T \cdot \Delta \alpha = 150 \times 15 \times 10^{-6} = 2.25 \times 10^{-3}$
Al/C-M40B	$= 45 \times 23 \times 10^{-6} = 1.04 \times 10^{-3}$
MgAl/C-M40B	$= 85 \times 26 \times 10^{-6} = 2.2 \times 10^{-3}$
Mg/C-Tenax	$= 50 \times 26 \times 10^{-6} = 1.3 \times 10^{-3}$

The volume change of the AlMg/Nextel610 system below 30°C ($\Delta T = 170$ K in cooling) indicates pore opening/formation but in a reversible way during slow thermal cycles. In the Al/C-M40 system pore opening/formation starts below 80°C when cooled from 200°C, which corresponds to a ΔT of 120 K for initiation of volume changes by pore opening (or closing during heating). It is concluded that Al-C systems are more sensitive to interface damage than the other investigated CFRM systems, but similar to MgAl/C-M40.

It is reported that, the damage due to thermal cycling in the alumina reinforced MMCs is not observable below approximately 1000 cycles [41]. In case of carbon fiber reinforced MMCs, damage is expected to be higher because of the higher mismatch between fibers and matrix. The density loss as an indication to the void formation shows that the damage is observable by density measurements after approximately 300 cycles. Debonding was not observed in the temperature range -40°C to 200°C neither with Al/C nor Mg/C.

The governing parameters for materials design in case of strong light weight structure needed are the specific modulus E/ρ and specific strength σ/ρ . For design against bending, the governing parameters are $E^{1/2}/\rho$ and $\sigma^{2/3}/\rho$. Composite materials are the only to increase both of these design parameters. The studied CFRM systems compared with some of the pure metals and some alloys showed the benefits of using composite materials as shown in Figs.5-33 to 5-36.

If we consider loads in the direction of fibers, all the studied MMC systems produce outstanding results, specially, the carbon fibers reinforced light alloys. The transverse properties are lower than that of the matrix because of poor stiffness and strength of the carbon fibers in the transverse direction from one hand and the strength is limited by the weak bond between matrices and fibers due to non reactivity in case of magnesium or from extensive interfacial reaction in case of Al. Textile or layered reinforcement designs have to be used to improve in plane properties over any angular range compared with transverse properties of UD samples. This has the draw back of necessary reduction of the fiber portion in the main load direction. But in case of alumina fibers, on the

expense of the relatively high CTE compared to carbon fibers, the results obtained from this MMC is less anisotropic in properties, but better than the matrix for both CTE (for longitudinal 27% and transverse 46%) and E modulus (for longitudinal 370% and transverse 250%). These properties can be fully exploited only if the structural components are designed properly according to the anisotropic- temperature dependent properties of CFRM.

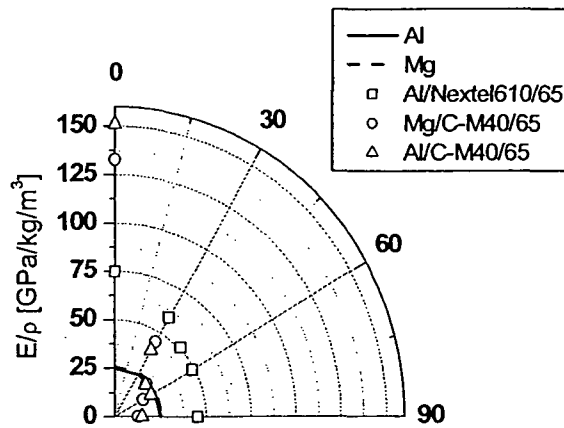


Fig.5-33, Polar diagram for specific modulus vs. fiber orientation for different materials.

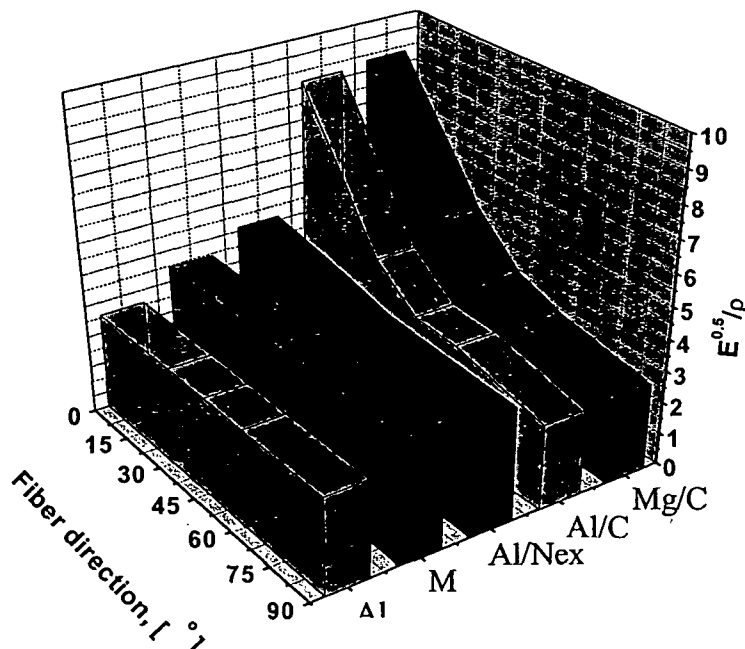


Fig.5-34, Relation between the ratio $E^{0.5}/\rho$ for different materials with fiber orientations.

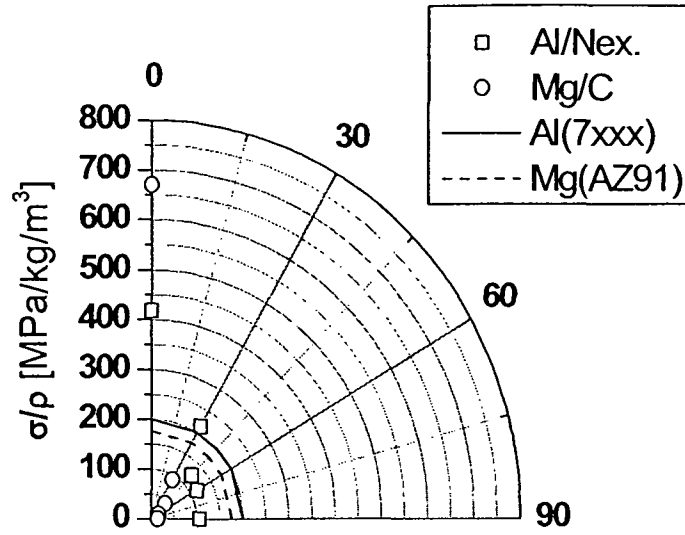


Fig.5-35, Polar diagram for specific strength vs. fiber orientation for different materials.

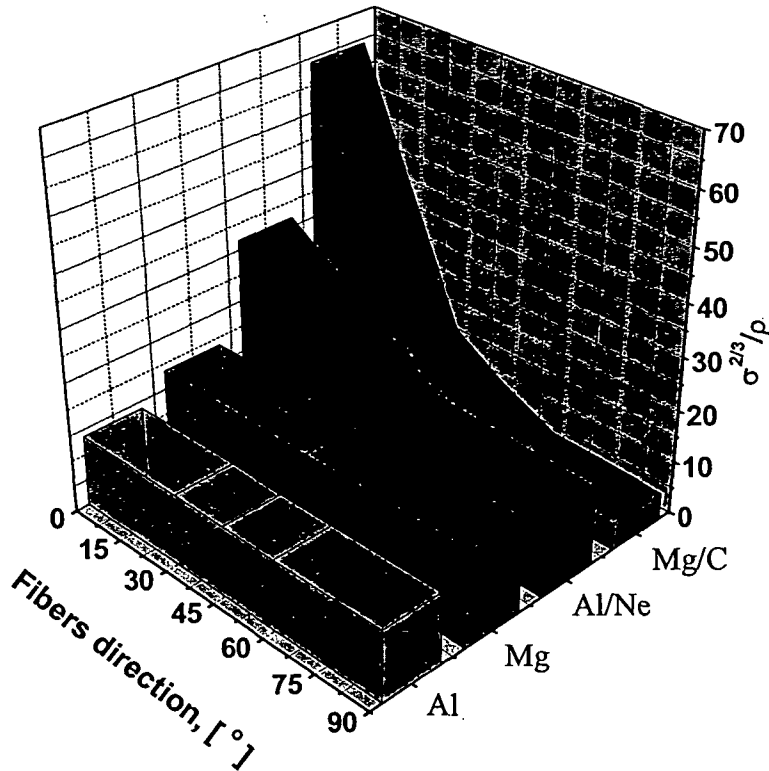


Fig.5-36, Relation between the ratio $\sigma^{2/3}/\rho$ for different materials with fiber orientations.

5.6. Anomalous CTE upon cooling

In our experimental determination of CTE, higher CTE values than the Schapery's model predictions were observed in cooling during conversion in both temperature ranges from -40°C to 120°C , and high from -40°C to 200°C in all the CFRM examined. The argument may be either the stress on the fibers is very low and the fibers shrinks faster as long as the matrix is in compression or the fibers behave anelastically, which means that the fiber modulus is different if in compression than in tension. The extreme behavior of the C-fibers may be assigned even to a change in their thermal expansion coefficient. Extended thermal amplitudes were applied to the Mg/Tenax system showing the higher CTE always for about 50 K during cooling from the maximum temperature, where an elastic regime is assumed.

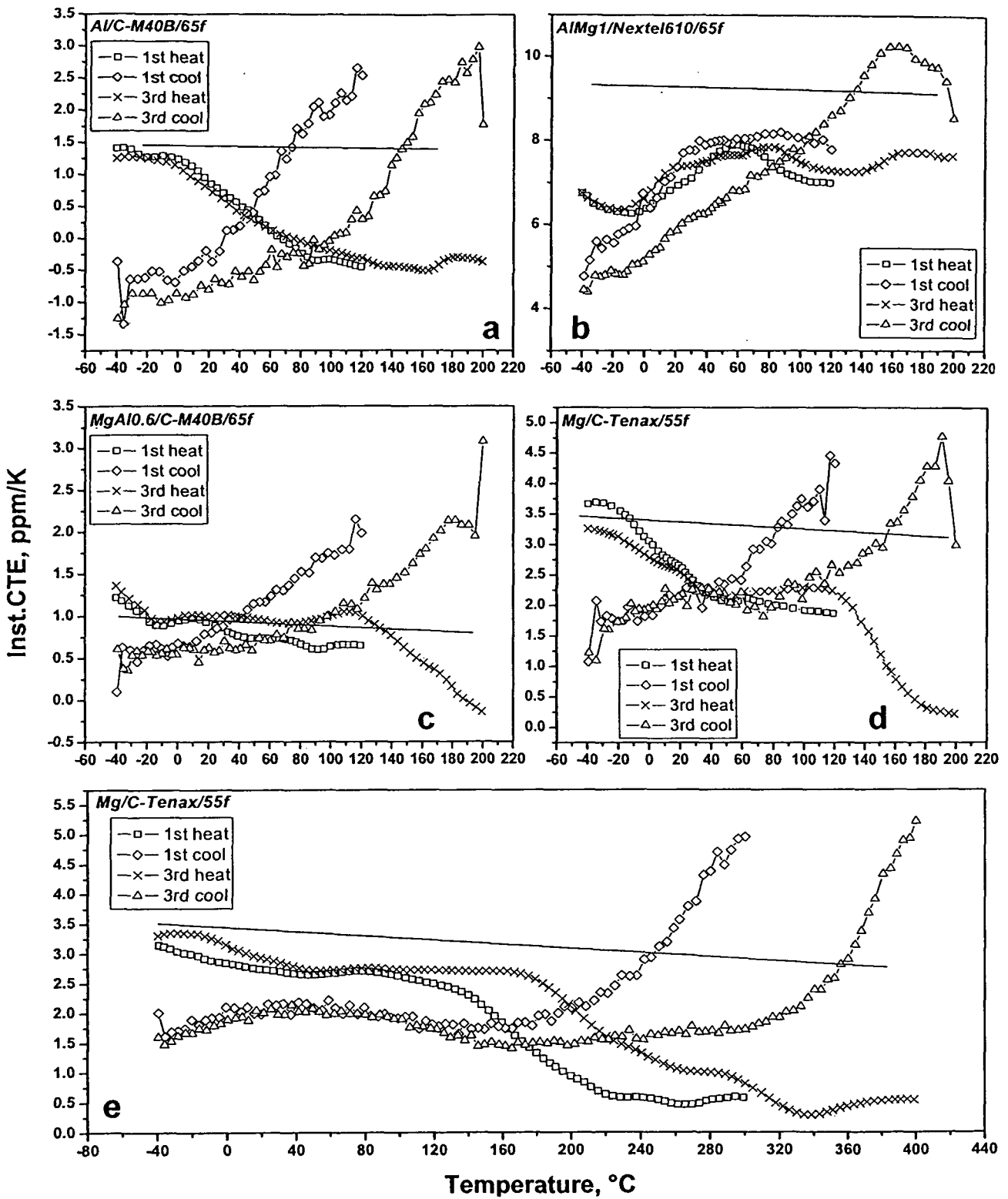


Fig. 5-37, Instantaneous CTE vs. temperature showing the higher CTE values in cooling compared with values in heating during thermal cycling, a) Al/C-M40B/65f, b) AlMg1/Nextel610/65f, c) MgAl0.6/C-M40B/65f, d) Mg/C-Tenax/55f from -40°C to 120°C and from -40°C to 200°C, e) Mg/C-Tenax/55f from -40°C to 300°C and from -40°C to 400°C, the solid line represents the Schapery's model for the CTE.

6. Conclusions

Dilatometry is a sensitive method to investigate the interaction between fibers and matrix and the residual stress situation during heating and cooling. Especially the consideration of volume expansion is helpful in understanding thermal expansion of anisotropic materials. Generally for the CFRM, the matrix is in tension from cooling from production temperature, it deforms elastically as well as plastically during thermal cycling changing from tension to compression and vice versa. The portion of elastic and plastic deformation is determined by the thermal mismatch of the system, the yield stress of the matrix and the temperature amplitude. The experimental CTE values in the longitudinal direction revealed a good agreement with that calculated by Schapery's model and the modified model considering plastification of the matrix.

A very low CTE value can be obtained in the longitudinal direction of UD carbon reinforced CFRM, due to the low longitudinal CTE value of the fibers. But due to the high thermal mismatch between the constituents, high stresses are induced in such materials.

The longitudinal expansion stops above a critical temperature during heating demonstrating the increasing dominance of the fibers exhibiting negative CTE. Surprisingly the elastic range governing thermal expansion is bigger for Mg-matrix than pure Al. Magnesium solid solution matrices are recommended for C-fiber reinforcement, because they offer the highest specific properties over a wide temperature range, but only in fiber direction. The main draw backs of carbon fiber reinforcement are the poor transverse stiffness and strength and the high transverse thermal expansion.

The low thermal mismatch stress between the alumina fibers and aluminium-magnesium alloy matrix leads to an approximately elastic behavior in the whole examined temperature range from -40°C to 200°C . Furthermore, the mechanical properties are increased in the transverse direction as well. Solid solution

aluminium matrix reinforced with alumina fibers offers reliable mechanical and thermal properties for design of components loaded multidirectionally.

Although the symmetric laminated material is designed to produce isotropic properties, it suffers from difficulties during production to achieve regular fiber distribution. If subjected to a bending loads, the isotropy is low.

The micro-computer tomography is an efficient nondestructive technique for detecting defects in materials: distortion in fiber arrangement, small cracks, and matrix veins.

It is important to note that the thermal history of CFRM produces residual stresses. Changing the temperature excursions may cause macroscopic distortions. The volume change of the AlMg/Nextel610 system below 30°C indicates pore opening/formation but in a reversible way during slow thermal cycles. In the Al/C-M40B system pore opening/formation starts below 80°C when cooled from 200°C, where closing starts as well during heating, which corresponds to a ΔT of 120 K for initiation of volume changes by pore opening or closing. It is concluded that Al/C-M40B and MgAl/C-M40B systems are more sensitive to interface damage than other investigated CFRM. Thermal cycling produces porosity if the temperature amplitude exceeds a certain range. Although it is closed reversible, it is the origin of damage.

References

1. A.Evans, C.S.Marchi, A.Mortensen, Metal matrix composites in industry; an introduction and a survey, Kluwer academic publishers, Norwell, Massachusetts, USA, 2003, p.1-8.
2. S.Rawal, Metal-Matrix Composites for Space Applications, Journal of metals, 53,4,2001, p. 14-17.
3. R.E.Smallman, R.J.Bishop, Modern physical metallurgy& materials engineering, Reed educational and professional publishing Ltd., 1999, p.361-375.
4. T.W. Clyne, P.J. Withers, An Introduction to Metal Matrix Composites, Cambridge University Press, Cambridge, 1993, p. 330 – 331.
5. Dong Sheng Li and Michael R.Winsom, Finite element micromechanical modelling of unidirectional fibre-reinforced metal-matrix composites, Composite science and technology, vol 51, Issue 4, 1994, p. 545-563.
6. R.F.Gibson, Principles of composite material mechanics, McGraw-Hill inc., New York, 1994, p.1-33.
7. K.G.Kreider, Metallic matrix composites, Academic press inc., London, 1974, p.1-35.
8. F.L.Matthews, R.D.Rawlings, Composite materials: Engineering and science, Alden press, Oxford, 1996, p.1-23.
9. F. Delannay in Comprehensive Composite Materials Vol. 3 “Metal Matrix Composites” (Ed.: A. Kelly, C. Zweben; Vol.Ed.: T.W. Clyne), Elsevier Science Ltd., Oxford, 2000, p. 341 – 343.
10. M.L. Greene , R.W. Schwartz , J.W. Treleaven, Short residence time graphitization of mesophase pitch-based carbon fibers, Carbon, 40, 2002, 1217–1226.
11. T. D. Burchell, Carbon materials for advanced technology, Elsevier Science Ltd., 1999.
12. D. D. Edie, The effect of processing on the structure and properties of carbon fibers, Carbon, Vol.36, No.4, 1998, p. 345-362.
13. C.G.Papakonstantinou, P.balaguru, R.E.Lyon, Comparative study of high temperature composites, Composite:B, B32, 2001, p. 637-649.

14. V.Michaud, A.Mortensen, Infiltration processing of fiber reinforced composites: governing phenomena, *Composites A*, A32, 2001, p. 981-996.
15. V.D.Scott, A.S.Chen, Collected studies on interfaces and interphases as related to the behaviour of fiber reinforced aluminium alloy composites, *Journal of microscopy*, Vol.196, 1999, p. 86-102.
16. E.Pippel, J.Woltersdorf, M.Doktor, J.Blucher, H.P.Degischer, Interlayer structure of carbon fiber reinforced aluminium wires, *Journal of material science*, 35, 2000, p.2279-2289.
17. H.Capel, S.J.Harris, P.Schulz, H.Kaufmann, Correlation between manufacturing conditions and properties of carbon fibre reinforced Mg, *Mat.Sci.Tech.*, July-August 2000, Vol 16, p. 765-768.
18. F.Wu, J.Zhu, Morphology of second phase precipitates in carbon fiber and graphite fiber reinforced magnesium based metal matrix composites, *Composite science and technology*, 57, 1997, p. 661-667.
19. R.J.Arsenault, *Metal matrix composites: Mechanics and properties*, ed. R.K.Everett, R.J.Arsenault, Academic press, Inc., UK, 1991, p.133-167.
20. C.CAYRON, Ph.D. Thesis, École polytechnique federale de Lausanne, 2000.
21. A.Vassel, Continuous fiber reinforced titanium and aluminium composites: a comparison, *Materials science and engineering*, A263, 1999, p.305-313.
22. D.Durcet, R.El Guerjouma, P.Guy, M.R'Mili, J.C.Baboux, P.Merele, Characterization of anisotropic elastic constants of continuous alumina fiber reinforced aluminium matrix composite processed by medium pressure infiltration, *Composite A*, A31, 2000, p. 45-55.
23. K.Schreiber, W.Hufenbach, A.Langkamp, L.Wagner, A.Kottar, P.Schulz, Erweiterte Strukturanalyse und angepasste Fertigungsmethoden fuer textilvertaerkte Magnesium-Verbundstrukturen in Huellbauweise, in *Verbundwerkstoffe und werkstoffverbunde*, (Ed. B.Wielage, G.Leonhardt), Wiley-VCH, Weinheim, Germany, 2001, p.127-133.
24. H.P.Degischer, P.Schulz, W.Lacom, Erreichte Kennwerte endlosfaserverstaerkter Al-und Mg-Matrixverbundwerkstoffe hergestellt mittels Gasdruckinfiltration, in *Verbundwerkstoffe und werkstoffverbunde*, Hrg. G. Ziegler, DGM-Oberursel, 1996, p. 517-520.

25. R.M.Jones, *Mechanics of composite materials*, Tayler and Francis Inc., Philadelphia, USA, 1999.
26. M.R.Piggott, *Load bearing fiber composites*, Pergamon press Ltd, Headington hill hall, Oxford, England, 1980.
27. C,Decolon, *Analyasis of composite structures*, Hermes Penton Ltd., London, England, 2002.
28. D. Ducret, R. El Guerjouma, P. Guy, M. R'Mili, J.C. Baboux, P. Merle, Characterisation of anisotropic elastic constants of continuous alumina fibre reinforced aluminium matrix composite processed by medium pressure infiltration, *composites A*, Part A31, 2000, p.45-55.
29. G.Korb, J.Korab and G.Groboth, Thermal expansion behaviour of unidirectional carbon fiber reinforced copper matrix composites, *Composites part A*, 29A, 1998, p.1563-1567.
30. R.U.Vaidya, K.K.Chawla, Thermal expansion of metal matrix composites, *Composite science and technology*, 50, 1994, p.13-22.
31. W.Lacom, J.Qu, H.P.Degischer, Th.Schmitt, H.Leitner, Thermal expansion of aluminium matrix composites, *Proceedings of the international conference on light metals, Advanced aluminium and magnesium alloys* (ed. T.Khan, G.Effenberg), Amsterdam, 1990, p. 711-718.
32. R.A.Schapery, Thermal expansion coefficient of composite mateials based on energy principles, *Journal of composite materials*, Vol.2, No.3, 1968, p.380-404.
33. S.Kumar, S.Ingole, H.Dieringa, K.U.Kainer, Analysis of thermal cycling curves of short fiber reinforced Mg-MMCs, *Composites Science and Technology*, 63, 2003,p.1805–1814.
34. H.J.Boehm, H.P.Degischer, W.Lacom, J.Qu, Experimental and theoretical study of the thermal expansion behavior of aluminium reinforced by continuous ceramic fibers, *Composite engineering*, Vol.5, No.1, 1995, p.37-49.
35. S.Rawal, *Metal-Matrix Composites for Space Applications*, JOM 53, 4, 2001, p. 14-17.
36. I.Dutta, Role of interfacial and matrix creep during thermal cycling of continuous fiber reinforced metal matrix composites, *Acta mater.*, 48, 2000, p. 1055-1074.

37. R.Holthe, K.Asboll, Carbon fiber reinforced aluminium-Manufacture and properties, Proc.ESA Symp.: Space applications of advanced structural materials, ESTEC, Noordwijk, 1990, p.307-312.
38. D.Masutti, J.P.Lentz, F.Delannay, Measurement of internal stresses and of the temperature dependence of the matrix yield stress in metal matrix composites from thermal expansion curves, Journal of material science letters, vol9, 1990, p.340-342.
39. Q.Sun, O.T.Inal, Fabrication and characterization of diamond/copper composites for thermal management substrate applications, Materials science and engineering, B41, 1996, p.261-266.
40. S.Q.Wu, Z.S.Weil, S.C.Tjong, The mechanical and thermal expansion behavior of an Al-Si alloy composite reinforced with potassium titanate whisker, Composite science and technology, 60, 2000, p.2873-2880.
41. Z.R.Xu, K.K.Chawla, A.Wolfenden, A.Neuman, G.M.Liggett, N.Chawla, Stiffness loss and density decrease due to thermal cycling in an alumina fiber/magnesium alloy composite, Materials science and engineering, A203, 1995, p.75-80.
42. H.J.Chun, I.M.Daniel, Residual stresses in a filamentary SiC/Al composite, Composites engineering, Vol.5, No.4, 1995, p.425-436.
43. H.Li, J.B.Li, Z.G.Wang, C.R.Chen, and D.Z.Wang, Dependence of thermal residual stress on temperature in a SiC particle reinforced 6061Al alloy, Metallurgical and materials transactions A, 29A, 1998, p.2001-2009.
44. Torayca technical reference manual, Toray industries, Inc.
45. Tenax data sheet.
46. 3M data sheet, metal matrix composites program, May 1998.
47. Zwick machine manual, May 2000.
48. P.L.Sullivan, D. Dykeman, Guidelines for performing storage modulus measurements using the TA Instruments DMA 2980 three-point bend mode: I. Amplitude effects, Polymer Testing, 19, 2000, p.155-164.
49. M.C.Dolizal, PhD thesis, Institute of material science and testing, Technical university, Vienna, 2003.

50. M.C.Dolizal, H.P.Degischer, *Aluminium*, 79, 2003, p.304-310.
51. S. Puchegger, D. Loidl, K. Kromp, H. Peterlik in: *Proceedings 14. Symposium-Verbundwerkstoffe und Werkstoffverbunde 2003* (Ed.: H.P. Degischer), Wiley-VCH, Weinheim, 2003, 280 - 285.
52. G. Kaindl, W. Lins, H. Peterlik, K. Kromp, R. Reetz, T. Reetz, *Interceram* 2000, 49 (2), 92 – 101.
53. W. Lins, G. Kaindl, H. Peterlik, K. Kromp, *Rev. Sci. Instr.* 1999, 70 (7), 3052 – 3058.
54. B.Audoin, *Non-destructive avaluation of composite materials with ultrasonic waves generated and detected by lasers*, *Ultrasonics*, 40, 2002, p.735-740.
55. E.Fraizier, M.H.Nadal, R.Oltra, *Laser-ultrasonics: a non-contact method to link the acoustic attenuation to metal damping properties up to the melting point*, *Materials science and engineering*, A370, 2004, p.396-400.
56. T.T.Wu, Y.H.Liu, *On the measurement of anisotropic elastic constants of fiber reinforced composite plate using ultrasonic bulk wave and laser generated Lamb wave*, *Ultrasonics*, 37, 1999, p.405-412.
57. P. Burgholzer, C. Hofer, B. Reitingner, A. Mohammed, H.P. Degischer, D. Loidl, P. Schulz, *Non-contact determination of elastic moduli of continous fiber reinforced metals*, *Composites Science and Technology*, in press.
58. R.L. Hassel, *American Labortory*, Vol. 1, 1991.
59. TMA 2940™, *Operator's Manual*, TA Instruments, New Castle, DE, 1999.
60. ASTM Standard E-831, "Linear thermal expansion of solid materials by thermodilatometry", *Annual Book of ASTM Standards*, Vol. 8.03., Philadelphia, PA, 1982.
61. J.D.James, J.A.Spittle, S.G.R.Brown, R.W.Evans, *A review of measurement techniques for the thermal expansion coefficient of metals and alloys at elevated temperatures*, *Measurement science and technology*, 12, 2001, p.R1-R15.
62. DIL 805™, *Operator's Manual*, Bähr Thermoanalyse, Hüllhorst, 1997.
63. J. Baruchel, J.-Y. Buffiere, E. Maire, P. Merle, G. Peix, *X-ray Tomography in Material Science*, Hermes Science, Paris, 2000.

64. E. Cornelis, A. Kottar, A. Mohammed, H. P. Degischer, X-Ray computed tomography characterising carbon fiber reinforced composites, Proceeding of ICCM14, San Diego, California, USA, No. 1365, July 14-18, 2003, CD-ROM.
65. S. Long, O. Beffort, L. Rohr, H. M. Flower, Effect of squeeze infiltration speed on infiltration quality and tensile properties of cast saffil/AlCu4MgAg composite, Proc. of 11th International Conference on Composites Materials, Vol. III: Metal Matrix Composites and Physical Properties, ed. by Murray L. Scott, Australia Composite Structures Society, Queensland, Australia, 1997, p.14-18.
66. A. Mohammed, H. Knoblich, A. Kottar, H.P. Degischer, P. Schulz, A. Langkamp, Continuous carbon fiber alignment in aluminium and magnesium matrices. Sonderbd. Prakt. Met. 2003; 34.
67. W. Hufnagel, Aluminium Taschenbuch, Aluminium-Verlag, Düsseldorf, Germany, 1988.
68. B. Moser, A. Rossoll, L. Weber, O. Beffort, A. Mortensen, Nextel610 alumina fiber reinforced aluminium: influence of matrix and process on flow stress, composites, Part A, A 32, 2001, p. 1067-1075.
69. C. Kammer, Magnesium Taschenbuch, Aluminium-Verlag, Düsseldorf, Germany, 2000.